Study of Two Jet Photoproduction at HERA

by

C. Coldewey

Study of Two Jet Photoproduction at HERA

Dissertation
zur Erlangung des Doktorgrades
des Fachbereichs Physik
der Universität Hamburg

vorgelegt von

Carsten Coldewey ∪
aus Hamburg

Hamburg
1995

For my parents
and
Elke

Abstract

At the HERA storage ring two jet photoproduction is measured for jets with a minimum transverse energy $E_t > 6\,\text{GeV}$ and for pseudorapidities in the ep–laboratory range $-1 < \eta_{jet} < 2$, for photon-proton center-of-mass energies $132\,\text{GeV} < \sqrt{s_{\gamma p}} < 265\,\text{GeV}$. The outgoing electron is not detected, limiting the maximum virtuality of the exchanged photon to $Q^2_{max} = 4\,\text{GeV}^2$, with a median value of approximately $10^{-3}\,\text{GeV}^2$. Dijet events are extracted from the data taken by the ZEUS experiment in 1993 using an integrated luminosity of $545\,\text{nb}^{-1}$.

The measured differential cross section is compared with the LO-QCD parton cross section as generated with the PYTHIA 5.6 program without use of fragmentation, a LO-QCD hadron jet cross section including jet fragmentation, and hadron jet cross sections using fragmentation, intrinsic k_t smearing and parton shower evolution for cutoff values of $p_{t,min} = 5.0\,\text{GeV}$ and $p_{t,min} = 2.5\,\text{GeV}$. Resolved and direct processes are included using the MRSD- proton parametrization and the GRV-LO and LAC1 parton density functions for resolved photoproduction.

In the backward direction ($\eta < 0$) the data are described within the systematic uncertainties by each of the hadron jet cross sections using the GRV-LO and LAC1 photon parametrization, while the LO-QCD parton cross section is above the data. The best description of the forward direction ($\eta > 0$) is obtained using intrinsic k_t smearing, fragmentation, and parton shower evolution with the low cut-off $p_{t,min} = 2.5\,\text{GeV}$. In this model, the data agree with the expectation of the LAC1 parametrization in the forward direction, while GRV-LO is below the data.

A measurement of the energy flow shows a satisfactory agreement between the data and the PYTHIA 5.6 Monte Carlo simulation, except in the forward (proton) direction close to the beam pipe. The energy deposition in the region $5^\circ < \theta < 15^\circ$ is approximately 30 % larger as compared to the Monte Carlo simulation. This energy excess in the forward direction is traced back to the resolved photoproduction process. It can be explained by the simple multiple interactions model implemented in PYTHIA 5.7.

Kurzfassung

Am HERA Speicherring werden Zweijet-Ereignisse in der Photoproduktion untersucht, wobei Jets mit einer transversalen Energie $E_t > 6\,\text{GeV}$ und einer Pseudorapidität $-1 < \eta_{jet} < 2$ (im ep-Laborsystem) für Schwerpunktsenergien des Photon-Proton-Systems im Bereich $132\,\text{GeV} < \sqrt{s_{\gamma p}} < 265\,\text{GeV}$ akzeptiert werden. Das nicht detektierte auslaufende Elektron begrenzt die maximale Virtualität des ausgetauschten Photons auf $Q^2_{max} = 4\,\text{GeV}^2$ bei einem mittleren Wert von $10^{-3}\,\text{GeV}^2$. Die Zweijet-Ereignisse wurden den 1993 mit dem ZEUS Experiment aufgezeichneten Daten entnommen, wobei eine integrierte Lumiosität von $545\,\text{nb}^{-1}$ erzielt wurde.

Der gemessene differentielle Wirkungsquerschnitt wird mit folgenden PYTHIA 5.6 Monte Carlo Wirkungsquerschnitten verglichen: Dem LO-QCD Parton Wirkungsquerschnitt ohne Fragmentierung, dem LO-QCD Wirkungsquerschnitt für Hadronen-Jets (mit Fragmentierung) und Wirkungsquerschnitten von Hadronen-Jets bei Verwendung von Fragmentierung, intrinsischer k_t-Verschmierung und Parton-Schauer-Entwicklung für Werte oberhalb von $p_{t,min} = 5.0\,\text{GeV}$ und $p_{t,min} = 2.5\,\text{GeV}$. Sowohl aufgelöste als auch direkte Photoprozesse werden berücksichtigt, wobei die MRSD-Parametrisierung für das Proton und die GRV-LO und LAC1 Partondichtefunktionen für die aufgelöste Photoproduktion verwendet werden.

Im Rückwärtsbereich ($\eta < 0$) werden die Daten innerhalb der systematischen Fehler durch jeden der Hadronen-Jet-Wirkungsquerschnitte sowohl für die GRV-LO als auch für die LAC1 Photon-Parametrisierung beschrieben. Die beste Beschreibung des Vorwärtsbereiches ($\eta > 0$) wird bei Verwendung von Fragmentierung, intrinsischer k_t-Verschmierung, Parton-Schauer-Entwicklung und einem Wert von $p_{t,min} = 2.5\,\text{GeV}$ erreicht. In diesem Modell stimmen die Daten mit den Erwartungen der LAC1 Photon-Parametrisierung im Vorwärtsbereich überein, während GRV-LO unterhalb der Daten liegt.

Eine Messung des Energieflusses zeigt eine zufriedenstellende Übereinstimmung zwischen Daten und der Simulation mit dem Programm PYTHIA 5.6, außer in der Vorwärtsrichtung (Proton-Richtung) nahe des Strahlrohrs. Die Energiedeposition im Bereich $5^\circ < \theta < 15^\circ$ ist etwa 30 % oberhalb des Wertes der Monte Carlo Simulation. Dieser Energieüberschuß in Vorwärtsrichtung kann auf die aufgelösten Photoprozesse zurückgeführt werden und wird durch das sogenannte *einfache Modell* der Vielfachwechselwirkungen, welches in PYTHIA 5.7 implementiert ist, weitgehend erklärt.

Acknowledgements

Contents

Chapter 1

Introduction

The history of experiments on deep inelastic scattering shows the strong relationship between experimental and theoretical progress. In the first deep inelastic scattering experiment in 1967 at the Stanford Linear Accelerator Center (SLAC) 20 GeV electrons were directed on a stationary target to probe the structure of the nucleon. Under the influence of these measurements and motivated by the assumption of Gell-Mann (1964) and, independently, Zweig that hadrons are combinations of more fundamental objects, the so-called quarks, the simple quark-parton model was proposed by Feynman (1969) as an intuitive picture to explain the observed Bjorken Scaling. In the parton model the nucleons are composed of point-like constituents, so-called partons, whose properties were identical with those of the quarks, which were originally introduced to account for hadron systematics. Thus, the parton model suggested the interpretation of the quarks as constituents of hadronic matter.

Data from SLAC indicated that roughly 50 % of the nucleon momentum is carried by neutral partons. Even before the discovery of scaling violation Quantum Chromodynamics as the local gauge theory of the strong interaction predicted eight electrically neutral spin-1 gauge field bosons, the gluons, as transmitter of the strong interaction, which could explain the fraction of the nucleon momentum carried by neutral partons. With the discovery of asymptotic freedom in 1972 Quantum Chromodynamics became a widely accepted theory of the strong interaction, which has been tested extensively during the last two decades. In particular particle interactions with high transverse momenta provide a rich source of information to compare data with perturbatively calculated QCD predictions.

One process especially suited for testing perturbative QCD is the transition of a photon into a hadronic system as observed in two-photon scattering. Disregarding the strong interactions, first calculations of the electromagnetic splitting process $\gamma \to q\bar{q}$ were carried out in lowest order QED for the scattering process $e^+e^- \to e^+e^- + \gamma^*\gamma \to e^+e^- + X$ where an almost real photon γ is probed by a highly virtual photon γ^* producing a hadronic final state X with large transverse momentum. In 1976, Witten calculated the renormalization of this scattering process and evaluated the structure functions of the photon in leading order perturbative QCD. He found

out, that in contrast to the hadrons the shape and the absolute normalization of the photon structure functions is calculable for high virtualities of the probing photon γ^*. Since this work much effort was concentrated in measuring the parton structure of the photon in high energy interactions of real photons.

First measurements of the photon structure functions were carried out in two-photon interactions at the e^+e^- colliders PEP, PETRA and TRISTAN. In analogy to deep inelastic electron-nucleon scattering, the scattering of a highly virtual photon on an almost real photon can be thought of as deep inelastic electron photon scattering. A shortcome of this kind of measurement is its insensitivity to the gluon content of the photon. In order to study the gluon distribution, scattering of almost real photons on nucleons can be used to determine the gluon distribution of the photon via parton-parton scattering processes.

The electron-proton collider HERA provides now the possibility to investigate the partonic photon structure including a determination of the gluonic photon content. At HERA, the first lepton-proton collider, collisions between 26.7 GeV electrons and 820 GeV protons offer the possibility to study a variety of processes in a new kinematic range with an electron-proton center of mass energy of $\sqrt{s} = 296\,\text{GeV}$. Electron-proton interactions are dominated by almost real photon exchange, which is very close to photoproduction with real photons. Photoproduction of high transverse momentum jets can be used to investigate the parton distributions of the photon by measuring the pseudorapidity distributions of the produced jets. In a leading-order QCD picture, the signature of hard photon-proton interaction due to quasi-real photon exchange is the production of two jets, which originate from the outgoing partons of the $2 \rightarrow 2$ parton scattering process.

This thesis is devoted to the measurement of the differential dijet cross section $(d\sigma/d\eta)_{\eta_1,\eta_2}$ of the two final state jets and it is structured as follows. In the second chapter an introduction to deep inelastic scattering, structure functions, the simple and the QCD improved quark-parton model and the Altarelli-Parisi evolution equations is given followed by a discussion of the physical photon and its interactions in high-energy collisions. Chapter 3 describes the ZEUS experiment at the HERA collider emphasizing the detector components used for the present analysis. Then, chapter 4 is used to give some informations about Monte Carlo techniques and the Monte Carlo generators taken for the event simulation. A description of the data selection including a discussion of trigger effects, off-line filters and a description of the cone algorithm for jet finding is presented in chapter 5. Chapter 6 is reserved for a comprehensive study of the selected dijet sample. General event characteristics, jet variables and the final state topology of hard photoproduction processes are shown. The observed energy excess in proton direction close to the beam pipe not described by the Monte Carlo program PYTHIA 5.6 is studied in detail. Finally detector effects and its influence on the jet reconstruction are estimated. Chapter 7 covers the measurement of the differential dijet cross section $(d\sigma/d\eta)_{\eta_1,\eta_2}$ and shows the result in a comparison with different Monte Carlo simula-

tions, including predictions using the GRV-LO and LAC1 photon parameterizations. Finally an analysis of the forward energy excess and its simulation by the simple multiple interactions model provided in PYTHIA 5.7 is presented in chapter 8.

Chapter 2

Photoproduction

In this chapter an overview of photon induced interactions of almost real photons is given. The structure of the physical photon and different theoretical models for the description of photon-photon and photon-proton scattering are introduced where the perturbative description of the photon in terms of parton density distributions is emphasized. The discussion starts with deep inelastic scattering, which is also used to explain the kinematic variables. Then structure functions are introduced as parametrizations of the hadronic tensor in a derivation of the differential double cross section $d\sigma^2/dxdy$. The meaning of the structure functions F_2 and F_1 is discussed in the simple quark-parton model, which is then modified to the QCD improved parton model. After a short discussion of asymptotic freedom, parton distributions and the Altarelli-Parisi equations, the photon structure as observed in two-photon physics is introduced. Then, the different states of the photon are used to explain direct and resolved photoproduction in photon-proton scattering.

In high transverse momentum collision, the processes photoproduction gives rise to the introduction of a photon structure function, similar to ordinary hadrons. Different approaches for photon parametrizations are discussed. Then, it is shown, how distributions of the jet rapidity can be used to decipher the quark-gluon structure of the resolved photon. Different reconstruction methods for the kinematics and next-to-leading order effects and their meaning for the definition of resolved and direct processes are discussed. Finally, the phenomenon of *multiple interactions*, which occurs in hadron-hadron collisions, is introduced. This class of interactions is under discussion as a possible explanation of the observations in this paper.

2.1   Deep Inelastic ep–Scattering

The basic process of deep inelastic electron-proton scattering is shown schematically in Fig. 2.1. The incoming electron exchanges a neutral (*neutral current*) or charged (*charged current*) electroweak gauge boson with the interacting struck quark. Due to the large momentum transfer, the proton breaks up and the struck quark frag-
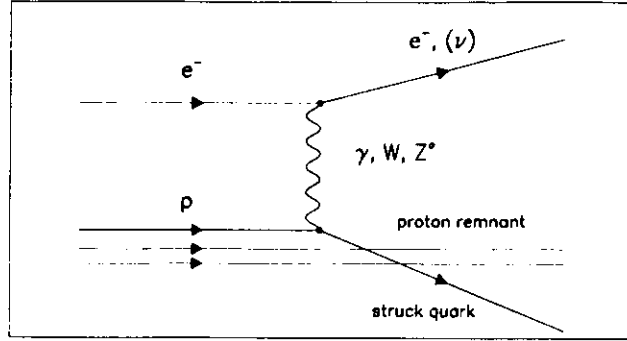
Figure 2.1: **Feynman graph of Deep Inelastic ep-Scattering**

ments into a jet of hadrons, called the *current jet*, while the remaining quarks of the proton move practically unperturbed along the incoming proton direction and form the *proton remnant jet*. The signature of this basic process is a current jet, and a scattered electron or neutrino for neutral and charged current processes, respectively, balancing each other in transverse momentum.

2.1.1   Kinematics

At fixed energies of the incoming electron and proton, for unpolarized electron and proton beams the kinematics is completely described by a set of two independent variables. For neutral current events the variables can be determined either from the scattered electron or the current jet, while for charged current events only the current jet is available. The following discussion concentrates on neutral current events where the measured quantities of the scattered electron can be used in the reconstruction of the kinematics.

The quantities that can be measured in the experiment are the energies and angles of the outgoing electron and hadrons. In deep inelastic scattering processes the outgoing hadrons are related to the current jet and the proton remnant jet. Taking into account the current jet and the scattered electron we have four quantities for the reconstruction, the energy and angle from the electron side and from the hadron system. Any combination of two of these four quantities can be used. For a detailed description of the different methods see [1]. Angles are measured in the cartesian coordinate system of the ZEUS laboratory frame where the z-direction is given by the proton beam direction, the x-axis points towards the center of the HERA ring collider and the y-axis is normal to the z-x plane. The origin of the coordinate system is at the nominal interaction point. The notation of the basic kinematical variables

of deep inelastic *ep*-scattering is given as follows:

M_p Rest mass of the proton

E_p Energy of the incoming proton

E_e Energy of the incoming electron

E'_e Energy of the outgoing electron

θ_e Polar angle of the outgoing electron, measured with respect to the positive z-axis (direction of proton beam)

p Four momentum of incoming proton

k_i Four momentum of incoming electron

k_f Four momentum of outgoing electron

These quantities are used to express the kinematics by Lorentz invariant variables such as the squared ep center of mass energy s, the invariant mass of the total hadronic system W, the energy transfer ν, the virtuality of the exchanged gauge boson given by the squared four-momentum transfer $-Q^2$ and the Bjorken-x and y variables, the so-called scaling variables, which are defined as follows:

$$q^2 = (k_i - k_f)^2 = -Q^2 \tag{2.1}$$

$$s = (k_i + p)^2 \tag{2.2}$$

$$W^2 = (p - q)^2 \tag{2.3}$$

$$\nu = \frac{q \cdot p}{M_p} \tag{2.4}$$

$$y = (q \cdot p)/(k_i \cdot p) \tag{2.5}$$

$$x = Q^2/(2q \cdot p) \tag{2.6}$$

As mentioned above, these variables are determined by two of the measured quantities. Using the energy and angle of the scattered electron, one obtains:

$$y_{elec} = 1 - \frac{E'_e}{2E_e}(1 - \cos\theta_e) \tag{2.7}$$

$$Q^2_{elec} = 2E_e E'_e(1 + \cos\theta_e) \tag{2.8}$$

One other possibility for the reconstruction of y and Q^2 is the use of the outgoing hadron flow according to the Jacquet-Blondel method with a summation over all final state hadrons.

$$y_{JB} = \frac{\sum_i (E_i - p_{zi})}{2E_e} \tag{2.9}$$

$$Q^2_{JB} = \frac{(\sum_i p_{xi})^2 - (\sum_i p_{yi})^2}{1 - y_{JB}} \tag{2.10}$$

The scaling variables x and y have simple interpretations in the naive parton model. The meaning of y becomes apparent in the rest frame of the proton. There, from the definition of y one obtains:

$$y = \frac{E_e - E'_e}{E_e} \tag{2.11}$$

i.e. in this frame y is the relative energy transfer from the electron to the proton. The interpretation of x as the fraction of the proton momentum carried by the parton entering the hard scattering must be given in a frame where the proton has infinite momentum. Neglecting proton and parton masses, the parton has a four-momentum xp, with $0 < x < 1$, where p is the four-momentum of the proton. The meaning of x follows directly from the definition of $x = Q^2/(2q \cdot p)$, which is the condition of elastic electron-parton scattering

$$0 = 2(xp)q + q^2 \tag{2.12}$$

with four-momentum xp. Since this replacement of the parton four-momentum leads to a variable parton mass $m = \sqrt{x^2 E^2 - x^2 \vec{p}^2} = xM_p$, the interpretation of x can be justified only in a frame, where the proton is moving with infinite momentum.

2.1.2 Fragmentation into Hadrons

Deep inelastic scattering in terms of the free quark-parton model language is founded basically on two characteristic features; first at short distances QCD predicts a small interaction expressed by the running coupling constant and secondly the lepton-proton scattering occurs at a time scale shorter than the typical interaction time between partons in the proton. For this reason the struck quark can be considered as a free particle during the hard interaction while the remaining partons are unaffected.

The scattering process can be divided in the hard scattering and a following fragmentation process. In the first step the exchanged electroweak gauge boson (γ, Z^0, W^+, W^-) couples to the lepton and a quark with a coupling given by the

electroweak theory of Glashow-Weinberg-Salam. In a second step the struck quark which acquired large recoil momentum escapes the proton. After a distance of some fm fragmentation begins where the colored parton is transformed into a colorless hadron jet which can be observed experimentally.

The interrelation between outgoing partons and the observable hadronic level is given by fragmentation models. Fragmentation is a non-perturbative long distance process, where the coupling constant α_s is large. In this confinement regime only phenomenological models can be applied. But there are well-developed approximation schemes such as the string fragmentation or cluster fragmentation. These and other fragmentation models give a good representation of existing data, and jet properties can be simulated by Monte Carlo (MC) studies. Jet cross section analyses show only small sensitivity to different fragmentation models, because of the advantage that jet energy and scattering angle depend only slightly on the particle content inside the jet. Nevertheless, there remains the non-trivial problem of the assignment of jet momenta to parton momenta, because it depends on the jet algorithm.

2.1.3 Structure Functions for Inelastic ep-Scattering

In Quantum Electrodynamics (QED) a formalism is available to compute scattering processes of point-like fermions. Cross sections are proportional to the lepton tensor product of the two scattered particles, where the lepton tensor is the spin summed and averaged scalar product of the incoming and outgoing lepton currents. For example, the cross section of electron-muon scattering is given by

$$d\sigma \sim L^{elec}_{\mu\nu} (L^{muon})^{\mu\nu} \tag{2.13}$$

with the electron $(L^{elec})_{\mu\nu}$ and muon $(L^{muon})^{\mu\nu}$ lepton tensor. Since the proton has a complicated structure the proton tensor cannot be calculated from the incoming and outgoing proton currents as in lepton-lepton scattering. Instead, Eqn. (2.13) is generalized to

$$d\sigma \sim L^{elec}_{\mu\nu} W^{\mu\nu} \tag{2.14}$$

where $W^{\mu\nu}$ is the proton tensor. For the proton tensor the most general Lorentz invariant form is constructed from the metric tensor $g^{\mu\nu}$ and the independent momenta p and q. The general form is simplified by parity conservation and conservation of the proton current. Under these constraints the most general form of the proton tensor can be written as

$$W^{\mu\nu} = W_1 \left(-g^{\mu\nu} + \frac{q^\mu q^\nu}{q^2} \right) + \frac{W_2}{M_p^2} \left(p^\mu - \frac{p \cdot q}{q^2} q^\mu \right) \left(p^\nu - \frac{p \cdot q}{q^2} q^\nu \right) \tag{2.15}$$

where W_1 and W_2 are functions of two Lorentz scalars describing the event kinematics. W_1 and W_2 are the structure functions of inelastic ep-scattering. If Z°-exchange is not negligible a parity violating structure function W_3 must be included. With the proton tensor the evaluation of the double differential cross section $d\sigma^2/dx\,dy$ leads to [2]:

$$\frac{d\sigma^2}{dx\,dy} = \frac{4\pi\alpha^2}{x^2y^2s}\left\{xy^2 M_p W_1 + [(1-y)-\frac{M_p^2 xy}{s}]\nu W_2\right\} \qquad (2.16)$$

with the fine structure constant α. In the simple quark-parton model, which assumes that the proton consists of non-interacting free quarks inelastic electron-proton scattering can be described by elastic scattering of electrons with point-like quarks. Since the partons are considered as point-like particles an increase of Q^2 reveals no further structures. For this reason structure functions must be independent of the transferred momenta. This is the so-called *Bjorken Scaling*, where the structure functions depend only on x and not on x and Q^2. Bjorken Scaling is expressed by the introduction of new structure functions resulting from a redefinition of W_1 and W_2:

$$M_p \cdot W_1(x, Q^2) \quad - \quad \cdot \quad F_1(x) \qquad (2.17)$$

$$\nu \cdot W_2(x, Q^2) \quad - \quad \cdot \quad F_2(x) \,. \qquad (2.18)$$

Using the structure functions F_1 and F_2 and neglecting the last term from Equ. 2.16 at HERA energies the double differential cross section can be written as:

$$\frac{d\sigma^2}{dx\,dy} = \frac{4\pi\alpha^2}{x^2y^2s}\{xy^2 F_1 + (1-y)F_2\} \,. \qquad (2.19)$$

2.1.4   The Simple Quark-Parton Model

The simple quark-parton model was introduced by Feynman and Bjorken (1969) to explain Bjorken scaling before the discovery of gluons and color interaction. This model is very attractive due to its simplicity. It is assumed that electron-proton scattering can be described by an incoherent sum of electron-parton scatters with free massless point-like partons in an infinite momentum frame with

$$\nu, Q^2 \longrightarrow \infty \qquad \text{and} \qquad x \equiv \frac{Q^2}{2\nu M_p} \,.$$

The double differential cross section $d\sigma/dx\,dy$ for scattering on a single quark can be derived in this model, assuming the partons are spin-$\frac{1}{2}$ quarks, using the cross section for fermion-fermion scattering,

$$\frac{d\sigma}{dQ^2} = \frac{4\pi\alpha^2 e_q^2}{Q^2}\left(1 - y + \frac{y^2}{2}\right) \qquad (2.20)$$

where e_q is the electric charge of the quark, and electron and quark masses are neglected. The electron-proton cross section is the sum of the corresponding electron-quark cross sections. Defining $f_q(x)dx$ as the probability to find a quark of the type q, carrying the momentum fraction x of the proton, one can write:

$$\frac{d\sigma}{dQ^2} = \frac{4\pi\alpha^2}{Q^2}\left(1 - y + \frac{y^2}{2}\right)\int\sum_q e_q^2 f_q(x)dx \qquad (2.21)$$

which leads to

$$\frac{d\sigma^2}{dx\,dQ^2} = \frac{4\pi\alpha^2}{Q^2}\left(1 - y + \frac{y^2}{2}\right)\sum_q e_q^2 f_q(x) \,. \qquad (2.22)$$

Using the relation $dQ^2 = sx\cdot dy$ one finds:

$$\frac{d\sigma^2}{dx\,dy} = \frac{4\pi\alpha^2}{sx^2y^2}\left(1 - y + \frac{y^2}{2}\right)\sum_q e_q^2 x f_q(x) \qquad (2.23)$$

After rewriting of this expression the final result is given by:

$$\frac{d\sigma^2}{dx\,dy} = \frac{4\pi\alpha^2}{sx^2y^2}\left\{xy^2\cdot\frac{1}{2}\sum_q e_q^2 f_q(x) + (1-y)\cdot\sum_q e_q^2 x f_q(x)\right\} \,. \qquad (2.24)$$

Comparing Equ. 2.24 with the cross section of Equ. 2.19 one obtains the equation:

$$2x F_1(x) = F_2(x) = \sum_q e_q^2 x f_q(x) \,. \qquad (2.25)$$

The first part is known as the Callan-Gross relation. It is a consequence of the $\frac{1}{2}$-spin of quarks and is confirmed in many experiments. Equ. 2.25 is one of many parton-model consequences. Further relations are certain sum rules; Adler (1966), Gross-Llewellyn-Smith, and Bjorken sum rule. Sum rules result from conserved quantities like the following rules which follow from the number of valence quarks

$$\int_0^1 (u(x) \quad \bar{u}(x)) dx = 2 \qquad (2.26)$$

$$\int_0^1 (d(x) \quad \bar{d}(x)) dx = 1 \qquad (2.27)$$

$$\int_0^1 (s(x) \quad \bar{s}(x)) dx = 0 \qquad (2.28)$$

where $u(x)$, $d(x)$, $s(x)$ are the quark density functions of up, down, and strange quarks, and $\bar{u}(x)$, $\bar{d}(x)$, $\bar{s}(x)$ denote the corresponding distributions of the antiquarks. The basic building blocks of all parton-model formulas are parton distributions which enter into all parton scattered cross sections and keep their meaning also in a leading-order QCD modified parton model.

In the quark-parton model, each hard scattering cross section can be calculated in a factorized form. For instance, the cross section of hadron-hadron scattering can be written as

$$\sigma_{AB} \sim \sum_{i,j} \int_0^1 \int_0^1 dx\, dx'\, \sigma_{ij}(x,x') f_{i/A}(x) f_{j/B}(x') \qquad (2.29)$$

where σ_{ij} is the perturbatively calculated cross section of partons i and j, and $f_{i/H}$ is the parton distribution of parton i in hadron H. The factorized form of Equ. 2.29 is a consequence of the QCD Factorization Theorem, discussed in the next section.

The Equivalent Photon Approximation

A specific application of the factorization method is the Equivalent Photon Approximation, which can be used to reduce the complexity of high energy photon-induced cross section calculations in small-angle electron scattering (photoproduction), where the radiation of the exchanged photon can be separated from the hard interaction. In photoproduction, the electron emits an almost real photon with a momentum $\vec{p}_\gamma = y\vec{p}_e$ which in turn interacts with the proton, producing a final state. The differential ep-cross section, therefore, can be written in the factorized form

$$d\sigma_{ep}^{photo}(p_e, p_p) = \int dy\, f_{\gamma/e}(y)\, d\sigma_{\gamma p}(p_\gamma, p_p). \qquad (2.30)$$

To a high degree of accuracy one can use the Weizsäcker-Williams approximation suggested in [3] to determine the photon flux factor (for $Q^2 >> m_e^2$)

$$f_{\gamma/e}(y) = \frac{\alpha}{2\pi} \frac{1 \cdot (1-y)^2}{y} \ln\left(\frac{E_e\Theta_{max}}{m_e}\right)^2 \qquad (2.31)$$

where Θ_{max} denotes the maximum angle of the scattered electron with respect to the direction of the incoming electron. Another form is given in reference to [4]

$$f_{\gamma/e}(y) = \frac{\alpha}{2\pi} \frac{1 \cdot (1-y)^2}{y} \ln\left(\frac{Q_{max}^2(1-y)}{m_e^2 y^2}\right) \qquad (2.32)$$

where Q_{max}^2 is the maximum virtuality of the exchanged photon that is counted as photoproduction, and which is used for the convolution of photoproduction cross sections in the PYTHIA generator.

2.1.5 QCD and the Quark-Parton Model

Quantum chromodynamics is the renormalizable, non-abelian gauge theory of the strong interaction. Due to the non-abelian character, it is more complicated than the abelian QED. A remarkable new property is the self-coupling of the gluons through a three and a four gluon vertex which has no analogue in QED. One implication of the self-coupling of gluons is the *asymptotic freedom* behaviour at high momentum transfer expressed by the *running coupling constant* α_s.

Asymptotic Freedom

Each cross section, which is calculated in perturbative QCD, can be expanded as an infinite series in powers of the strong coupling constant α_s

$$\sigma = A_1\alpha_s + A_2\alpha_s^2 + \dots$$

The coefficients are given by the appropriate Feynman diagrams. Various divergences which enter matrix elements with one or more loops can be cancelled by the renormalization formalism in different renormalization schemes. The most commonly used are the modified minimal subtraction-scheme ($\overline{MS}$) and the momentum subtraction scheme (MOM). Renormalization introduces running quark masses and analogous a running coupling constant $\alpha_s(Q^2)$ which depends on a typical momentum scale Q^2 of the hard interaction. The theory is renormalized at a particular renormalization scale μ where the coupling constant is given by $\alpha_s(\mu^2) = \alpha_s(Q^2 = \mu^2)$.

The final result of a renormalizable theory, i.e. the cross section of the infinite series, cannot depend on the scheme or the scale value μ. However, in practice the series is truncated after one or two terms and this introduces a scheme and scale dependence to the theory. The question, what scheme and what value of μ is the best choice, cannot unambiguously be answered. It is known that next-to-leading order calculations are less sensitive than leading order calculations. But next-to-leading order formulations exist only for a small number of processes. Commonly

used Monte Carlo generators as PYTHIA or HERWIG are based on leading-order matrix element calculations with leading-order and next-to-leading order structure functions.

Renormalizable field theories are parameterized by the coupling constant $\alpha_s(\mu^2)$ and the scale μ. Since observables, calculated to all orders, should not depend on μ, a change of μ must be compensated by a change of the coupling constant. This is the physical meaning of the Renormalized Group Equation (RGE), where a function β controls the μ-dependence of the strong coupling $\alpha_s = g_s^2/4\pi$ and relates different values of α_s at different values of Q^2. Renormalized group equation and the expanded β-function are given by

$$\mu\frac{\partial g_s}{\partial \mu} = \beta(g_s,\mu) \tag{2.33}$$

$$\beta(g_s) = -\beta_0\frac{g_s^3}{16\pi^2} - \beta_1\frac{g_s^5}{(16\pi^2)^2} + \mathcal{O}(g_s^7) \tag{2.34}$$

$$\beta_0 = 11 - \frac{2}{3}N_f \tag{2.35}$$

$$\beta_1 = 102 - \frac{38}{3}N_f \tag{2.36}$$

where N_f is the number of flavours. The first two coefficients (β_0,β_1), and only these, of the β-expansion are independent of the choice of a particular renormalization scheme, while for higher orders a scheme dependence must be considered. In first order, where the first β-term is kept and inserted into the RGE differential equation, one obtains the solution:

$$\alpha_s(Q^2) = \frac{12\pi}{(33-2N_f)\cdot\ln(Q^2/\Lambda^2)} \tag{2.37}$$

The integration constant Λ is the free fundamental QCD parameter which can be extracted by comparing QCD predictions with experimental data. The given expression is valid in each renormalization scheme, but with the appropriate scheme dependent values of Λ. A rough estimate with Λ_{MOM} of about 300 MeV gives $\Lambda_{\overline{MS}} \approx \frac{1}{2}\cdot\Lambda_{MOM}$.

The coupling constant Eqn. (2.37), decreases with increasing Q^2 and vanishes in the asymptotic limit $Q^2 = \infty$. This is the meaning of asymptotic freedom in hard scattering processes where Q^2 is large. Asymptotic freedom is the QCD basis of the simple parton model where contributions of the order α_s can be neglected and scaling violation is only a small correction.

Factorization Theorem

The justification of the simple parton model by perturbative QCD is based on some fundamental theorems which are real predictions of the theory. One is the Factorization Theorem [5] which gives a generalization of Eqn. (2.29):

$$\sigma_{AB} \sim \sum_{i,j}\int_0^1\int_0^1 dx\,dx'\,H_{ij}(x,x',\mu_f,\mu)f_{i/A}(x,\mu_f,\mu)f_{j/B}(x',\mu_f,\mu) \tag{2.38}$$

where σ_{ij} of Eqn. (2.29) is replaced by a hard scattering function H_{ij}, calculable in perturbation theory. Parton distributions and the hard scattering function H_{ij} depend on two mass scales, one of which is the renormalization scale μ. The separation of short-distance from long-distance contributions introduces the so-called factorization scale μ_f. Roughly speaking, the factorization scheme defines the hard scattering process and the parton distributions, whereas the factorization scale μ_f serves to separate propagators according to their virtuality. Propagators that are off-shell by μ_f^2 or more contribute to the hard scattering process while infrared propagators below this scale are absorbed into the parton density. There exist several factorization schemes and the most commonly used are the DIS and the $\overline{MS}$ scheme, see [5] for an introduction. The DIS scheme is attractive for its familiar form of the F_2 structure function, which will be the same as in the simple quark-parton model, while a remarkable feature of the $\overline{MS}$ scheme is the calculational simplicity.

The different factorization schemes reflect the freedom in the separation of the hard scattering process from the infrared long-distance effects. In principle, for a comparison of data and theory it is important to use schemes and scales consistently, especially in collisions with different types of hadrons as in resolved photon-proton scattering. In practice, however, common Monte Carlo generators use only the parton-parton Born cross sections, which are the lowest order approximation of the hard scattering cross section expansion

$$H_{ij} = H_{ij}^{(0)} + \frac{\alpha_s}{\pi}H_{ij}^{(1)} + \ldots$$

where $H_{ij}^{(0)}$ is independent from the factorization scale and is viewed as elastic parton-parton scattering.

The Altarelli-Parisi Equations

The dependence of the parton distributions on the factorization scale can be described by the Altarelli-Parisi equations. Altarelli and Parisi [6] gave an illuminating physical interpretation of the Q^2-dependence of F_2, called scaling violation, which is based on the QCD diagrams, as shown in Fig. 2.2. A parton carrying momentum fraction y

splits into two partons which share the momentum with fractions of $x = zy$ and $y - x = (1 - z)y$. In this way each parton is itself surrounded by a cloud of partons and the parton density depends on the resolution scale of the scattering process. In deep inelastic scattering this scale is given by the virtuality Q^2 of the exchanged photon. The distance resolution is given by the uncertainty principle and scales with $1/\sqrt{Q^2}$. Hence there are found more partons with small x at high Q^2, while the parton densities for high x-values decrease with increasing Q^2, because of the momentum loss due to the splitting processes.

To determine the Q^2-dependence from this intuitive picture one can follow the approach by Altarelli and Parisi. The probability for a splitting process, where a quark radiates a gluon and leaves itself with a momentum fraction $x = zy$, is found as

$$\frac{\alpha_s}{2\pi} P_{q \to q}(z) . \tag{2.39}$$

The other splitting processes are described in the same way. There are four splitting functions, corresponding to the QCD diagrams in Fig. 2.2. The splitting functions are calculated from Feynman rules and for $z < 1$ they are found to be:

$$P_{g \to q}(z) = \frac{1}{2}\left(z^2 + (1-z)^2\right) \tag{2.40}$$

$$P_{g \to g}(z) = 6\left(\frac{1-z}{z} + z(1-z) + \frac{z}{1-z}\right) \tag{2.41}$$

$$P_{q \to q}(z) = \frac{4}{3}\left(\frac{1 - z^2}{1-z}\right) \tag{2.42}$$
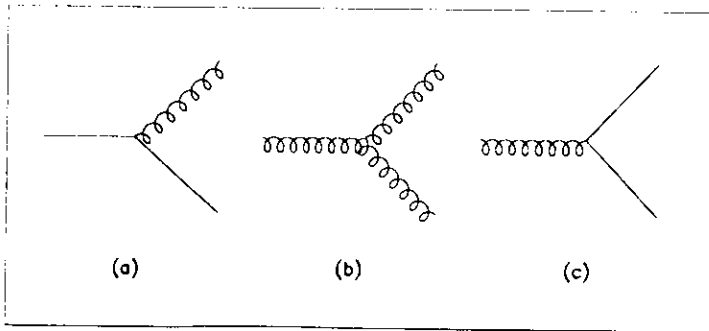
Figure 2.2: Parton splitting processes

$$P_{q \to g}(z) = \frac{4}{3}\left(\frac{1 + (1-z)^2}{z}\right) . \tag{2.43}$$

Using these probabilities the evolution of the parton distributions is given by the integrodifferential Altarelli–Parisi equations

$$\frac{df_q(x,Q^2)}{d\ln Q^2} = \frac{\alpha_s(Q^2)}{2\pi} \int_x^1 \frac{dy}{y}\{f_q(y,Q^2)P_{q \to q}(\frac{x}{y}) + g(y,Q^2)P_{g \to q}(\frac{x}{y})\} \tag{2.44}$$

$$\frac{dg(x,Q^2)}{d\ln Q^2} = \frac{\alpha_s(Q^2)}{2\pi} \int_x^1 \frac{dy}{y}\{\sum_q f_q(y,Q^2)P_{q \to g}(\frac{x}{y}) + g(y,Q^2)P_{g \to g}(\frac{x}{y})\} \tag{2.45}$$

where $f_q(x,Q^2)$ and $g(x,Q^2)$ denote the quark and gluon distributions, respectively, and the index q runs over all quark and antiquark flavours. The solution of the evolution equations depends on the hadronic input distributions f_q and g at $Q^2 = Q_o^2$, which have to be determined by experimental data. As mentioned, the violation of the order $\mathcal{O}(\ln(Q^2))$ depends on x. The presentation of F_2 as a function of Q^2 for different x-values shows approximate scaling around $0.1 < x < 0.2$. The high x range $x > 0.2$ is dominated by quark-quark splitting $P_{q \to q}$ which gives negative contributions to the scaling violation, while for low x ($x < 0.1$) the positive $P_{g \to q}$ contribution gives rise for an increase of the sea-quark distribution.

Parton Distributions of the Pion

In the next section, it will be shown that the hadronic behaviour of the photon is strongly related to the parton distributions of the pion. For this reason, a specific sum rule, which can be applied to pions is used to determine some features concerning the general x-shape of the parton distributions.

The discussion of the Altarelli-Parisi approach deals with three different kinds of parton distribution, the valence quark distribution, the gluon distribution and the sea quark distribution. The latter depends on the gluons due to the $q\bar{q}$-pair production mechanism. From the discussion it is clear that the valence quark distribution dominates the higher x-range, while gluon and sea quark distribution are large in the small x-region. More quantitatively, several aspects of the parton densities of the pion can be deduced by the *dimensional counting rule* from Brodsky and Farrar (1973) [7], which can be used to extract the general parton shape of the valence quark, the sea quark and the gluon contribution in the limit $x \to 1$. In this limit the x-shape is given by

$$f(x) \sim (1-x)^{2n_s - 1} \tag{2.46}$$

where n_s is the minimum number of partons which have to accompany the scattered parton in a pion. For instance, a valence quark of a pion is at least accompanied by the second valence quark, which leads to $n_s = 1$. The configuration for a gluon with a minimum number of additional partons is one gluon and the two valence quarks, which gives $n_s = 2$. A sea quark is at least accompanied by the two valence quarks and a second sea quark due to the $q\bar{q}$-pair production. Therefore the sea quark distribution is determined by $n_s = 3$ and the dimensional counting rule leads to the following x-shapes for the valence quark, the sea quark and the gluon distribution:

$$q_v(x) \sim (1-x) \tag{2.47}$$

$$q_s(x) \sim (1-x)^5 \tag{2.48}$$

$$g(x) \sim (1-x)^3 . \tag{2.49}$$

2.2   The Photon Structure Function

2.2.1   The Physical Photon

In the classification of elementary particles, the photon is a point-like gauge particle. However, through its couplings to quarks it has the possibility to fluctuate into a quark-antiquark pair $\gamma \to q\bar{q}$ which gives rise to several descriptions for the photon itself and for its interactions in $\gamma\gamma$ and γp reactions. In the approach of a complete description of high energy photoproduction Schuler and Sjöstrand [8] have introduced a picture of the physical photon, in which the photon can exist in three different states. In this section a description of the physical photon is given, which follows mainly this intuitive picture of the photon.

The predictive power of different models for the interactions of real photons depends basically on the degree of the virtuality of the photon fluctuation in the considered kinematic region, which is approximately given by the squared transverse momentum p_t^2 of the q and $\bar{q}$ with respect to the photon direction. Fluctuations of small virtualities correspond to a long-lived $q\bar{q}$ state with roughly collinear outgoing quarks accompanied by a cloud of soft gluons. These low-p_t fluctuations are the base of the vector-meson-dominance (VMD) model, where the photon couples to a vector meson with the same quantum numbers as the photon, $J^{PC} = 1^{--}$. In case of high virtualities the fluctuation is too short-lived to develop a hadronic state and the splitting of a real photon into two quarks with large p_t is perturbatively calculable in the simple [9] and in the QCD improved quark-parton model in both lowest order [10] and in next-to-leading order [11]. This point-like interaction is called the anomalous component. Beside the interaction via photon fluctuation, in photon-proton scattering, there exist also the bare-photon interactions, the so-called direct processes, where the photon couples directly to a parton within the proton.

In this picture the physical photon is a superposition of a bare photon $|\gamma_B\rangle$, a hadronic component described by a superposition of vector meson states, and the anomalous quark-antiquark state $|q\bar{q}\rangle$

$$|\gamma\rangle = \sqrt{Z_3}\,|\gamma_B\rangle + \sum_{V=\rho^0,\omega,\phi} \frac{e}{f_V}|V\rangle + \frac{e}{f_{q\bar{q}}}|q\bar{q}\rangle \tag{2.50}$$

where

$$Z_3 = 1 - \sum_{V=\rho^0,\omega,\phi}\left(\frac{e}{f_V}\right)^2 \left(\frac{e}{f_{q\bar{q}}}\right)^2 . \tag{2.51}$$

The factor $(e/f_V)^2 = 4\pi\alpha/f_V^2$ gives the probability for the coupling of a real photon to the vector meson. In the VMD approach with no inclusion of heavier vector mesons as in the generalized vector dominance (GVD), the coefficients $f_V^2/4\pi$ are taken to be 2.2, 23.6, and 18.4 for ρ^0, ω, and ϕ, respectively. The VMD approach [13] has led to a successful description of soft photon nucleon interactions, where γN and πN reactions are closely similar.

The squared amplitude of the anomalous photon contribution depends on a typical scale μ of the interaction and a cut-off $p_o \approx 0.5\,\text{GeV}$, see [8].

$$\left(\frac{e}{f_{q\bar{q}}}\right)^2 \approx \frac{\alpha}{2\pi}\frac{N_c}{3}\left(2\sum_q e_q^2\right)\ln\left(\frac{\mu^2}{p_o^2}\right) \tag{2.52}$$

where N_c is the number of flavours that can be assumed massless compared with μ. Due to the logarithmic dependence on the scale $\mu \approx p_t$, the anomalous contribution becomes important in hard photoproduction with the production of high-E_t jets, while it is less relevant for the VMD regime.

2.2.2   The Photon Structure Function F_2^γ

Present photon structure functions for real or almost real photons are obtained experimentally from two-photon interactions at e^+e^- colliders, where deep inelastic electron photon scattering can be used to extract F_2^γ. Deep inelastic electron photon scattering can be described similar to deep inelastic ep scattering, where a highly virtual photon probes the structure of an almost real photon. The experimental signature of these events is one tagged electron (positron) requiring a minimum scattering angle to provide a sufficiently large virtuality for one photon, and an unobserved positron (electron) with small deflection, to ensure a second photon with low virtuality.

In deep inelastic electron-photon interactions, two contributions of the physical photon have to be taken into account, the hadronic component, as given by the VMD

model, and the point-like anomalous part, as shown in Fig. 2.3. Motivated by the separation of photon-photon physics into hadron-like and point-like coupling, it seems reasonable that the photon structure function F_2^γ can be expressed by a combination of a point-like and a hadron-like part.

$$F_2^\gamma \cong F_2^{point} + F_2^{had} . \tag{2.53}$$

The nonperturbative hadronic contribution can be taken from the VMD model as a superposition of the lowest vector meson states:

$$F_2^{had} = \frac{4\pi\alpha}{f_\rho^2} F_2^\rho + \frac{4\pi\alpha}{f_\omega^2} F_2^\omega + \frac{4\pi\alpha}{f_\phi^2} F_2^\phi . \tag{2.54}$$

Using the assumption that the lowest vector meson states are described by the pion structure function, gives:

$$F_2^{had} = \alpha \left(\frac{4\pi}{f_\rho^2} + \frac{4\pi}{f_\omega^2} + \frac{4\pi}{f_\phi^2} \right) F_2^\pi , \tag{2.55}$$

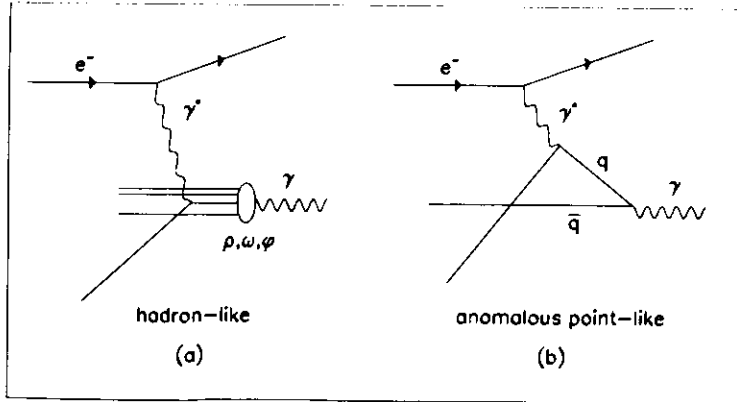Figure 2.3: Two Photon Scattering
An almost real photon γ interacting with a highly virtual photon γ^* through hadron-like (a) and point-like (b) coupling.

which leads to a hadronic photon structure completely determined by the pion structure function. Neglecting sea quark and gluon contributions the dimensional counting rule gives the ansatz for F_2^γ with a $(1 - x_\gamma)$ dependence, yielding by comparison with experiments to [14]:

$$F_2^{had} \approx \alpha(0.2 \pm 0.05)(1 - x) . \tag{2.56}$$

The anomalous point-like component of the photon structure function can be calculated in lowest-order QED (simple parton model) and in both leading-order and next-to-leading order perturbative QCD. The lowest-order QED calculation of the photon structure functions was done by Walsh and Zerwas [9] in a framework of the free quark-parton model. In contrast to the nucleon, F_2^{point} can be calculated completely from the QED splitting process $\gamma \to q\bar{q}$, as shown in Fig. 2.3 (b). Neglecting terms of $\mathcal{O}(m_q^2)$ one obtains [12]:

$$F_{2_{QED}}^{point} = \frac{3\alpha}{\pi} \sum_q x e_q^4 \left[\left(x^2 + (1 - x)^2 \right) \ln \frac{W^2}{m_q^2} + 8x(1 - x) - 1 \right] \tag{2.57}$$

where W is the invariant mass of the photon-photon system and W and Q^2 are related through

$$W^2 = Q^2 \frac{1 - x}{x} . \tag{2.58}$$

The first term in the sum shows a logarithmic scaling violation, the typical signature of the QCD improved parton model. But in this case the scaling violation is caused by the increasing phase space for transverse momenta with increasing Q^2.

It should be mentioned, that the partonic structure of the photon has some important differences compared with common hadrons. First, contrary to hadron structure functions, in case of the photon for $F_{2_{QED}}^{point}$ not only the Q^2 and the x dependence but also the absolute normalization can be calculated from the analytical form of Equ. 2.57.

Then, in deep inelastic electron-hadron scattering the probed parton of the hadron is free and on mass shell, while for a photon target the interacting quark is a virtual part of the inner splitting process.

Further, while counting rules predict small values for the nucleon structure function F_2 in the high x region, the photon structure function $F_{2_{QED}}^{point}$ increases at high x values according to Equ. 2.57, as shown in Fig. 2.4.

Finally, Equ. 2.57 exhibits also a critical point, concerning the quark mass term in the logarithm. The quark-parton model neglects all mass effects and deals with massless partons. In many applications the following leading log Q^2 approximation of the simple quark-parton model is used, where constant terms are neglected and

the quark-mass is replaced by an arbitrary scale parameter, which can be put equal to the QCD scaling parameter Λ:

$$F_{2_{\text{QED}}}^{\text{point}} = \frac{3\alpha}{\pi} \sum_q x e_q^4 \left(x^2 + (1-x)^2\right) \ln \frac{Q^2}{\Lambda^2} . \tag{2.59}$$

Using the parton model relation Equ. 2.25 one obtains for the quark distributions:

$$f_q(x, Q^2) = \frac{3\alpha}{2\pi} e_q^2 \left(x^2 + (1-x)^2\right) \ln \frac{Q^2}{\Lambda^2} . \tag{2.60}$$

2.2.3 F_2^γ in the QCD Improved Quark-Parton Model

In the QCD improved QPM, the simple QPM prediction is modified by gluon radiation that can be emitted and absorbed by the strongly interacting quarks from the splitting process $\gamma \to q\bar{q}$. An implementation of the anomalous point-like coupling in perturbative QCD can be achieved through regularization followed by renormalization. This was done by Witten [10], who carried out the renormalization of the free QPM solution by calculating the moments of the photon structure function $F_{2_{\text{QCD}}}^{\text{point}}$ using the Operator Product Expansion method.

Considerable interest in the experimental program of a measurement of $F_{2_{\text{QCD}}}^{\text{point}}$ was pushed by the fact that the the photon structure function can be absolutely predicted in the asymptotic limit $(Q^2 \to \infty)$. Witten found, that the Q^2 dependence of the photon structure function as predicted by Equ. 2.57 is correct, while the form of the asymptotic solution has to be computed numerically. If the asymptotic solution is also relevant for finite Q^2-values, Witten's observation would be one of the cleanest tests of QCD. But unfortunately, it turned out that singularity problems in the small x-region do not vanish for finite Q^2-values, as expected by Witten. The leading order QCD result diverges for $x = 0$ and it has been shown by Rossi [15] that this behaviour becomes even worse in higher order calculations.

Fig. 2.4 shows for values of $Q^2 = 10\,\text{GeV}^2$ and $Q^2 = 1000\,\text{GeV}^2$ the point-like part of the photon structure function F_2^γ for the full solution of the free QPM, Equ. 2.57, the leading $\log Q^2$ approximation of the free QPM, Equ. 2.59, and the asymptotic QCD prediction, where the Duke Owens parameterization [16] is used for the photon parton distributions. All predictions are characterized by a large quark-content at high x-values in contrast to the parton distributions of hadrons. This behaviour is a trivial result from the photon splitting into a quark-antiquark pair, which carries the total four momentum of the photon.

The observed deviation between the full solution and the leading $\log Q^2$ approximation of the free QPM in the high x region is caused by the x dependent term neglected in the leading $\log Q^2$ approximation. This term describes the decreasing phase space for transverse momenta at high x.
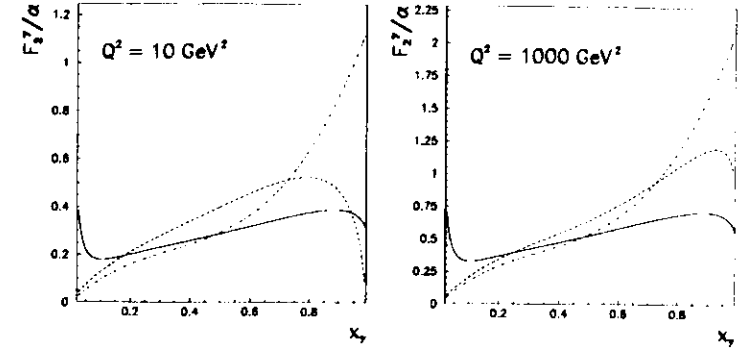
Figure 2.4: Photon structure function
The dashed curve shows the Equ. 2.57 of the free quark-parton model with three flavors, where the quark masses are roughly approximated through the QCD scale parameter $\Lambda = 0.2\,\text{GeV}$. The dash-dotted curve shows the leading $\log Q^2$ approximation of the free QPM, Equ. 2.59, where all Q^2-independent terms of Equ. 2.57 are neglected. The full line is the Duke Owens parameterization of the asymptotic solution in leading order QCD.

The small x behaviour of the asymptotic QCD solution illustrates clearly the singularity problem at $x = 0$, which cannot be treated as a small correction. Bardeen [11] realized that the singularity problem is related to the separation of the photon structure function into a perturbative point-like and a nonperturbative hadron-like VMD part. As shown by Frazer [17], this separation cannot be achieved in a consistent way because infrared singularities of the point-like part must be cancelled by infrared singularities which are associated with the VMD component of the resolved photon. How the singularity problem is embedded in this physical picture is shown by the higher order diagrams of Fig. 2.5 [18], which are responsible for infrared divergences. The first two diagrams (a), (b) are related to singularities in the point-like asymptotic solution, while the third one (c) is associated with the bound vector state. For this reason, the VMD term cannot be separated, and in this respect the suggested prescription $F_2^\gamma = F_2^{\text{had}} + F_2^{\text{point}}$ is wrong.

It was shown by Glück et al. [18] that the singularity problems can be eliminated only if the nonperturbative hadronic part and the perturbative point-like part are combined and treated together in a formalism like the Altarelli-Parisi ansatz; similar to the evaluation of normal hadron structure functions. In order to obtain a general solution, input distributions must be given at a value $Q^2 = Q_o^2$ as boundary conditions

Figure 2.5:
Diagrams of infrared singularities assigned to the point-like part and the VMD part of the photon structure function.

to the Altarelli-Parisi equations, which include the nonperturbative hadronic part of the photon. These parton distributions have to be determined experimentally and are not predicted by the theory.

2.2.4 The Photon in the Altarelli-Parisi Formulation

In contrast to the deep inelastic electron-nucleon case, the parton distributions in the photon satisfy inhomogeneous evolution equations. While the nonperturbative hadronic part of the g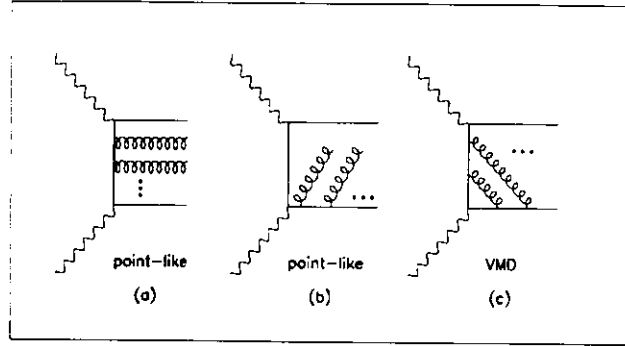eneral parton distribution can be evolved through the same Equ. 2.55 as in the nucleon case, an additional inhomogeneous term must be introduced to take into account the splitting process of a photon into a quark-antiquark pair. The splitting process is described by the leading-order splitting function $P_{\gamma \to q}$:

$$P_{\gamma \to q} = \frac{3\alpha}{2\pi} e_q^2 \left(x^2 + (1 - x)^2 \right) . \qquad (2.61)$$

Note, that the multiplication of $\ln(Q^2/\Lambda^2)$ with $P_{\gamma \to q}$ recovers the quark distribution of the free QPM leading log Q^2 approximation, as given in Equ. 2.60. With the use of $P_{\gamma \to q}$ and the evolution variable $t = \ln Q^2/\Lambda^2$ the Altarelli-Parisi equations for the photon can be written as:

$$\frac{df_q(x,Q^2)}{dt} = P_{\gamma \to q}(x) + \frac{\alpha_s(Q^2)}{2\pi} \int_x^1 \frac{dy}{y} \{ f_q(y,Q^2) P_{q \to q}(\frac{x}{y}) + g(y,Q^2) P_{g \to q}(\frac{x}{y}) \}$$

$$\frac{dg(x,Q^2)}{dt} = \frac{\alpha_s(Q^2)}{2\pi} \int_x^1 \frac{dy}{y} \{ \sum_q f_q(y,Q^2) P_{q \to g}(\frac{x}{y}) + g(y,Q^2) P_{g \to g}(\frac{x}{y}) \} .$$

The second equation for the evolution of the gluon distribution contains no inhomogeneous term because there is no photon-gluon vertex in the theory, which connects directly a photon with a gluon.

The point-like contribution is described through the inhomogeneous term while the nonperturbative hadron-like part is given by the homogeneous equation system. If the point-like interaction is switched off, the same situation remains as for hadrons and the resulting parton distributions exhibit properties as known from meson-states. But due to the inhomogeneous term the general solution is given by the solution of the corresponding homogeneous and a particular solution. In contrast to the homogeneous solution the inhomogeneous term causes a nonvanishing quark distribution in the asymptotic solution ($Q^2 \to \infty$) which is independent of the boundary condition at finite Q^2. But at finite Q^2-values there remains a dependence on the initial quark input, and the solution is not unique. The required input quark distribution at $Q^2 = Q_o^2$ is orientated on VMD quark distributions, which give a good agreement for $\gamma\gamma$ scattering at $Q^2 = 1\,\mathrm{GeV}^2$. A clean test of QCD predictions is only possible, if the required boundary conditions (input parton distributions) are extracted from experimentally measured structure functions.

2.2.5 Parton Distributions of the Photon

The parameterization of Q^2-dependent parton distributions is generally divided into two approaches, one using the separation of F_2^γ into a point-like and hadron-like part and a second where the parton distributions are obtained from full solutions of the leading order Altarelli-Parisi equations.

In the first approach, the point-like distribution can be calculated directly from the free quark-parton model prediction Equ. 2.57 or from a parameterization of the asymptotic leading order solution. A parametrization of the latter is the one from Duke and Owens [16]. The hadronic distributions are taken via VMD from the pion structure function through Equ. 2.55. The most commonly used hadronic input of the form

$$F_2^\pi = 0.2(1 - x) \qquad (2.62)$$

where only the contribution from the valence quark is considered, gives hadronic parts of the photon structure functions, which seem to be much weaker than what

was found in recent investigations of the pion-nucleon Drell Yan process, Castorina and Donnachie [19]. The published parametrizations of the pion parton distributions for $Q^2 = 2.5\,\text{GeV}^2$, which also represent low Q^2 photon structure function results very well, are

$$xq_v(x, Q_o^2) = 0.766\sqrt{x}(1-x)^{0.6} \qquad (2.63)$$

$$xq_s(x, Q_o^2) = 0.112(1-x)^5 \qquad (2.64)$$

$$xg(x, Q_o^2) = 1.408(1-x)^3 \qquad (2.65)$$

where q_v, d_s and g denote the valence quark, sea quark and gluon distribution, respectively. These parametrizations are used as input distributions in an Altarelli-Parisi evolution to obtain a Q^2-dependent pion structure function. One can take the quark-distribution to calculate the hadron part of the photon structure function, which leads to

$$F_2^{\text{had}} = 0.31\sqrt{x}(1-x)^{0.6} + 0.11(1-x)^5 \; . \qquad (2.66)$$

A similar expression can be derived using the pion parameterization of Owens and Reya;

$$F_2^{\text{had}} = 0.42\sqrt{x}(1-x) + 0.11(1-x)^5 \; . \qquad (2.67)$$

It should be noted, that only the valence quark distributions are tightly constrained through the Drell Yan $q\bar{q}$ annihilation, while there is a considerable freedom for the sea quark and gluon distribution. Unfortunately, our knowledge about the gluon content of all hadrons is rather poor, since $F_2(x, Q^2)$, the main source of information, is quite insensitive to the gluon distribution.

The approach to parameterize parton distributions from full solutions of the Altarelli-Parisi evolution equations has been undertaken by Drees and Grassie (DG) [20], Abramowicz, Charchula and Levy (LAC) [21] and Glück, Reya and Vogt (GRV) [22]. The first analysis is based on seven available data points from PLUTO at only one value $Q^2 = 5.9\,\text{GeV}^2$. The second analysis made use of the Drees and Grassie study with all data of PETRA, PEP and TRISTAN with Q^2 above the considered initial value Q_o^2. The LAC and GRV parametrizations shall be discussed in more detail. While GRV predicts a moderate gluon contribution at low x_γ-values, the parametrizations of LAC1 and LAC2 are characterized by a large gluon content in that region.

The Abramowicz-Charchula-Levy Parametrizations

In order to determine a parameterization for the solution of the evolution equations the Abramowicz, Charchula and Levy approach uses four flavors, neglecting possible

contributions from b and t quarks. The charm contribution is considered only if the invariant $\gamma\gamma$ mass is above the mass threshold of two charm quarks with an assumed mass of $m_c = 1.5\,\text{GeV}$. For the QCD scale parameter $\Lambda = 0.2\,\text{GeV}$ is taken, and checks with $\Lambda = 0.4\,\text{GeV}$ give stable results, i.e. no changes within the errors. A particular inhomogeneous solution for the $P_{\gamma \to q}$ term and a general solution of the homogeneous equation system are needed to solve the AP equations for the photon. For the four quark distributions an ansatz with 10 free parameters was used:

$$xq(x) = Ae_q^2 x \frac{x^2 + (1-x)^2}{1 - B\ln(1-x)} + C_q X^{D_q}(1-x)^{E_q} \; . \qquad (2.68)$$

The first term reflects the photon splitting behaviour, while the second term describes the typical form of quark distributions in the nucleon. Isospin invariance of u and d quarks leads to the same coefficients $C_u = C_d$, $D_u = D_d$ and $E_u = E_d$. Furthermore, it is assumed that the hadronic motivated sea quark contents (second term) of strange and charme quark differ only in amplitude, but not in shape, i.e. $D_s = D_c$, $E_s = E_c$ and $C_s \neq C_c$. For the gluon distribution the following assumption is used:

$$xg(x) = C_g x^{D_g}(1-x)^{E_g} \; . \qquad (2.69)$$

At the end, 13 free parameters were fitted to 62 (51) data points from the experiments PETRA, PEP and TRISTAN with initial values of $Q_o^2 = 1\,\text{GeV}^2$, $(4\,\text{GeV}^2)$. The $Q_o^2 = 1\,\text{GeV}^2$ fit was performed for a comparison with the Drees and Grassie parameterization. The result of this fit is the LAC3 parameterization with a very strange gluon distribution. The LAC3 gluon distribution peaks at high x-values in contrast to the normal behaviour, where gluons produced through parton radiation dominate the low-x range. This normal gluon distribution is reproduced by the other two parametrizations LAC1 and LAC2. They used a higher starting value of $Q_o^2 = 4.0\,\text{GeV}^2$.

The difference between LAC1 and LAC2 is the result of an artificial difference of the gluon input in the LAC2 parameterization. In order to estimate the spread of the gluon distribution in the small x-region D_g was set to zero for the LAC2 parameterization. A table of the fitted parameters is given in [21]. The final parton distributions are tabulated for the range $10^{-4} < x < 1$ and $Q_o^2 < Q^2 < 10^5\,\text{GeV}^2$ and can be interpolated for any given x and Q^2 within this range.

The Glück-Reya-Vogt Photon Parameterization

The GRV approach is of particular interest because of its unusual methodical ansatz. Glück, Reya and Vogt evolved parton parametrizations for proton [23], pion [24] and photon [22] by the requirement of a valence-like structure of all parton distributions at

a low scale $\mu^2 \approx 0.25\,\text{GeV}^2$. Common evolutions of the Altarelli-Parisi equations start at much higher values of about $\mu^2 = 1\text{-}5\,\text{GeV}^2$. Now, this method will be described for the pion case, giving parton densities which are later used for the photon structure function via the vector meson dominance model.

The experimental input of the valence-like quark distribution is taken at $Q_o^2 = 2\,\text{GeV}^2$ from $\pi^{\pm}p \rightarrow \gamma X$ direct-γ measurements with a quark distribution ($q(x) = \bar{q}(x)$) of

$$xq(x, Q_o^2) = 0.681 x^{0.48}(1 \quad x)^{0.85} . \tag{2.70}$$

This distribution together with the constraints of valence-like distributions at $\mu^2 = 0.25\,\text{GeV}$ allows the evolution of parton densities for valence quarks, sea quarks and gluons in the range $10^{-5} < x < 1$ and $0.3 < Q^2 < 10^8\,\text{GeV}^2$. For the pion, the valence-like gluon distribution is coupled to the quark distribution through

$$g_\pi(x, \mu^2) = k q_\pi(x, \mu^2) \tag{2.71}$$

at the low input scale $Q^2 = \mu^2$, where k is uniquely fixed by the energy-momentum sum rule

$$\int_0^1 x \left[2q_\pi(x, \mu^2) + g_\pi(x, \mu^2) \right] dx = 1 . \tag{2.72}$$

In a first approximation it is assumed that the sea quark density vanishes at μ^2. Through the connection of the gluon to the quark distribution, no further gluon parameter is introduced, and gluon and sea quark densities are dynamical results of the Altarelli-Parisi evolution. It is worth to note that the low-x behaviour is independent of arbitrary input parametrizations for $x \rightarrow 0$, due to the vanishing of valence-like inputs.

The same method was applied to the photon using the pion input distributions also for the photon at the same μ^2. Quark and gluon input distributions of the pion are invoked through the VMD model:

$$q^\gamma(x, \mu^2) = \kappa \frac{4\pi\alpha}{f_\rho^2} q^\pi(x, \mu^2) \tag{2.73}$$

$$g^\gamma(x, \mu^2) = \kappa \frac{4\pi\alpha}{f_\rho^2} g^\pi(x, \mu^2) . \tag{2.74}$$

The free parameter κ corresponds to ambiguities through the coherent or incoherent addition of the ω and ϕ mesons. Using this input distributions for the photon leaves only a one parameter fit where κ has to be extracted by a least-squares fit from

the experiment by performing the Q^2 evolution for different values of κ. The best fit is found for $\kappa = 2.0$. A parameterization of the leading order parton distributions can be found in [22].

Comparison of GRV and LAC Distributions

Fig. 2.6 shows the quark and gluon distributions for LAC1, LAC2 and GRV-LO. Fig. 2.6(f) shows only the gluon distribution of LAC3 and is not discussed further, because recently results from TOPAZ [25] and AMY [26] taken at the e^+e^- collider TRISTAN ruled out LAC3. They measured inclusive jet cross sections in $\gamma\gamma$ scattering with two quasi-real photons. This process is sensitive to the gluon content of the photon in contrast to deep inelastic electron photon scattering with one highly virtual photon, which couples only to the charged quarks.

The Figs. 2.6(a)–(e) present the gluon and quark distributions for u, d, s and c quarks at $Q^2 = 4.0\,\text{GeV}^2$. At first, one can see that LAC1 and LAC2 are very similar parametrizations with only small differences in the low x-region. Then it is shown that the quark distributions of LAC1 and GRV in the high x-region are also similar at least within a factor of 2. From an experimental point of view, a distinction between LAC1, LAC2 and GRV must be based on the strong difference of the gluon distributions, which are much higher for the LAC parametrizations in the region $x < 0.2$ as shown in Fig.2.6(e). Unfortunately, this kinematic region is difficult to measure due to the reduced parton-parton center of mass energy. In particular at HERA with its unsymmetric event topology due to the 820 GeV proton beam and a 26.7 GeV electron beam, for hard photoproduction there is an intrinsic experimental restriction to the region approximately given by $x > 0.1$.

The photonic gluon contribution

In this work the study of the parton distributions of the photon concentrates on the comparison of data with the leading-order predictions from GRV and LAC1, which differ mainly for the gluon distributions at low x_γ. Most of the current available photon parametrizations agree reasonably well in their quark distributions, because they are based on existing data from the same e^+e^- experiments, which are sensitive only to the quark contribution of the photon. Since there exist no useful momentum sum rules for the photon as in the case of hadrons the gluon parametrizations contain still ambiguities. Most of the current photon parametrizations use the form of Equ. 2.69.

Gordon and Storrow (GS) [27] used a fixed gluon input distribution $xg(x, Q_o^2) = \alpha 1.711(1 - x)^3$ at the input scale $Q_o^2 = 5.3\,\text{GeV}^2$, which is similar to the gluon distributions obtained from the Drees-Grassie (DG) [20], Duke-Owens (DO) [16] and Glück-Reya-Vogt (GRV) [22] parametrizations. All these photon parametrizations are characterized by a moderate increase of the gluon density at low-x values, while the Levy-Charchula-Abramowicz (LAC) [21] approach predicts a much stronger increase of $g(x)$ for $x_\gamma \rightarrow 0$, as shown in Fig. 2.6(e). Fig. 2.7 shows a comparison of the
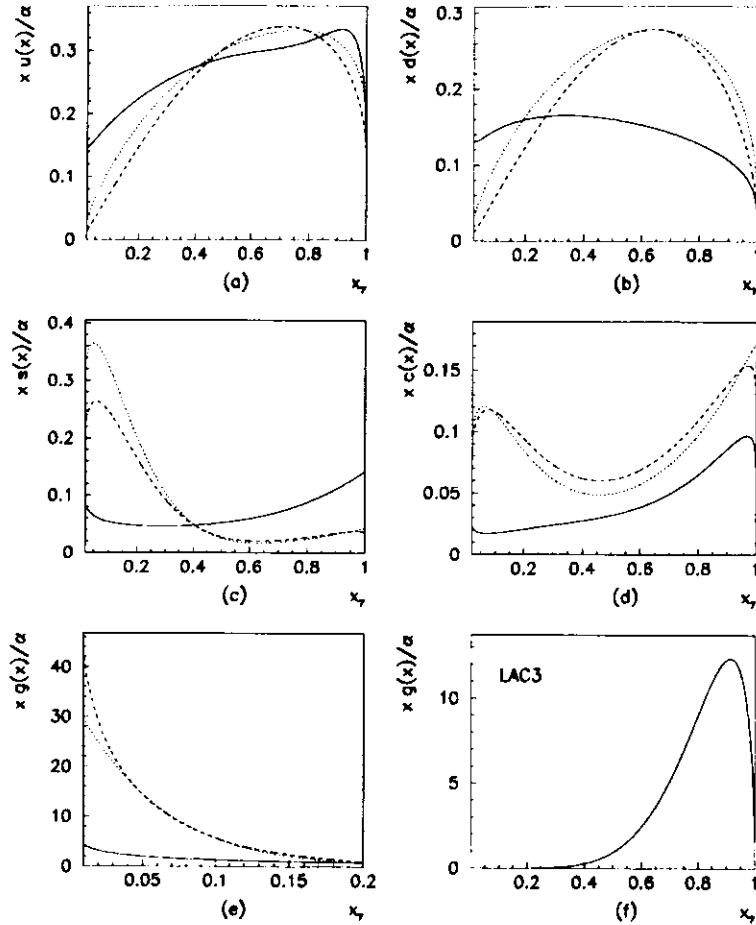
Figure 2.6: Quark and gluon distributions of the photon

Figures (a)-(d) show quark distributions $xu(x)$, $xd(x)$, $xs(x)$, $xc(x)$ for the up, down, strange and charm quark. In figure (e) the gluon distribution is shown. Dashed, dotted and full lines represent the parametrizations LAC1, LAC2 and GRV-LO at $Q^2 = 4.0\,GeV^2$. Figure (f) shows the gluon distribution of LAC3.
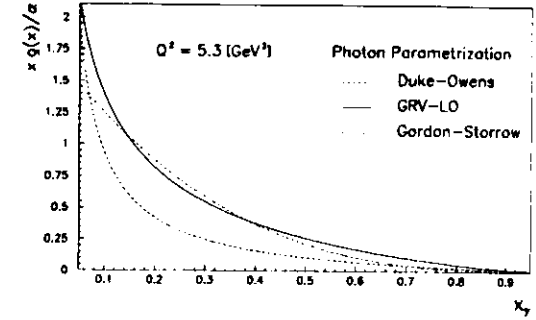
Figure 2.7:

Gluon distributions $xg(x)/\alpha$ of the photon. Dashed, dashed-dotted and full line represent the Duke-Owens, the GRV-LO and the Gordon-Storrow leading-order photon parametrizations.

gluon distributions from the GRV-LO, DO and GS parametrizations at the scale $Q_o^2 = 5.3\,GeV^2$. It is seen, that the distributions differ only slightly compared with the difference between the GRV-LO and the LAC1 predictions, as shown in Fig. 2.6(e). Therefore, in this work the GRV-LO parametrization is taken as a typical candidate with a moderate gluon distribution in the low x region, and it will be compared with the expectations from LAC1.

2.3 Photoproduction in ep Scattering

In high energy ep scattering at low Q^2, the electron emits an almost real photon approximately in the direction of the incoming electron, which then interacts with the proton. Therefore, the electron-proton collider HERA can be regarded as an photon-proton collider.

So far, the discussion of the photon structure was mainly related to deep inelastic electron-photon scattering experimentally measured in e^-e^- colliders. In contrast to deep inelastic $e\gamma$ scattering, where the photon structure functions are determined via inclusive lepton measurements, and (x_γ, Q^2) are fixed by the scattered electron, the inclusive scale $\hat{Q}^2$ off the hard interaction is not known in γp scattering. In perturbative leading order QCD calculations it is common to take the transverse momentum of the scattered partons, but there is a considerable freedom in the choice of the hard scale. Therefore, a direct measurement of the photon structure function is not possible at the ep collider HERA.

Photoproduction at an *ep* collider is more related to hadron-hadron collisions, where a parton of the resolved photon interacts with a parton of the proton including the gluon contributions from the photon and the proton side. It is this sensitivity to the gluon content of the photon which makes resolved photoproduction at the *ep* collider HERA interesting, while measurements of F_2^γ depend only on the quark distributions and are quite insensitive to the gluon content of the photon.

2.3.1 Direct and Resolved Processes

In high-energy γp interactions jet photoproduction can be used to study the partonic structure of the resolved photon and the proton. In leading order perturbative QCD two classes of processes contribute to jet production, the *direct* and the *resolved* processes. Fig. 2.8 shows Feynman diagrams of the *QCD Compton Scattering* and the *Boson-Gluon Fusion* direct processes and a *resolved* photoproduction process. The signature of the leading order direct and resolved diagrams is the production of two jets coming from the hard interaction. Both jets are scattered back-to-back in the xy-plane with a difference of the jet azimuth angles of $\Delta\phi \approx 180°$ and with almost identical transverse momenta p_t. In addition to the outgoing jet-pair, there is a low-p_t photon remnant in resolved processes. It is expected [28], [29] that the photon remnant can be used to separate resolved and direct processes. The hard interacting parton of the resolved photon carries only a fraction x_γ of the photon four-momentum leaving a photon remnant with the remaining momentum fraction of $(1 - x_\gamma)$, while in direct processes the whole photon is absorbed, i.e. $x_\gamma = 1$.

The pseudorapidity distribution of high-E_t jets

The polar angle θ, measured with respect to the positive z direction, is conveniently expressed by a variable η known as pseudorapidity, in the following called rapidity for short, given by:

$$\eta = \frac{1}{2}\ln\left(\frac{1 + \cos\theta}{1 - \cos\theta}\right) = -\ln\left(\tan\left(\frac{\theta}{2}\right)\right) . \qquad (2.75)$$

Rapidity distributions of high-p_t jets have been successfully used in the determination of parton distributions at $p\bar{p}$-colliders [30]. Because of its large cross section, jet production offers a good opportunity to distinguish between various theoretical models of the photon. Rapidity distributions of jets are strongly related with the x-behaviour of the parton distributions. Therefore, it is natural to use the rapidity dependence of cross sections to get information about parton densities. Fletcher *et al.* [31] suggested a measurement of the sum of the rapidities $d\sigma/d(\eta_1 + \eta_2)$ in dijet events to decipher the quark-gluon structure of the photon. In [32] M. Drees and R.M. Godbole discuss cross sections of dijet events with the same rapidity $\eta_1 = \eta_2$. In
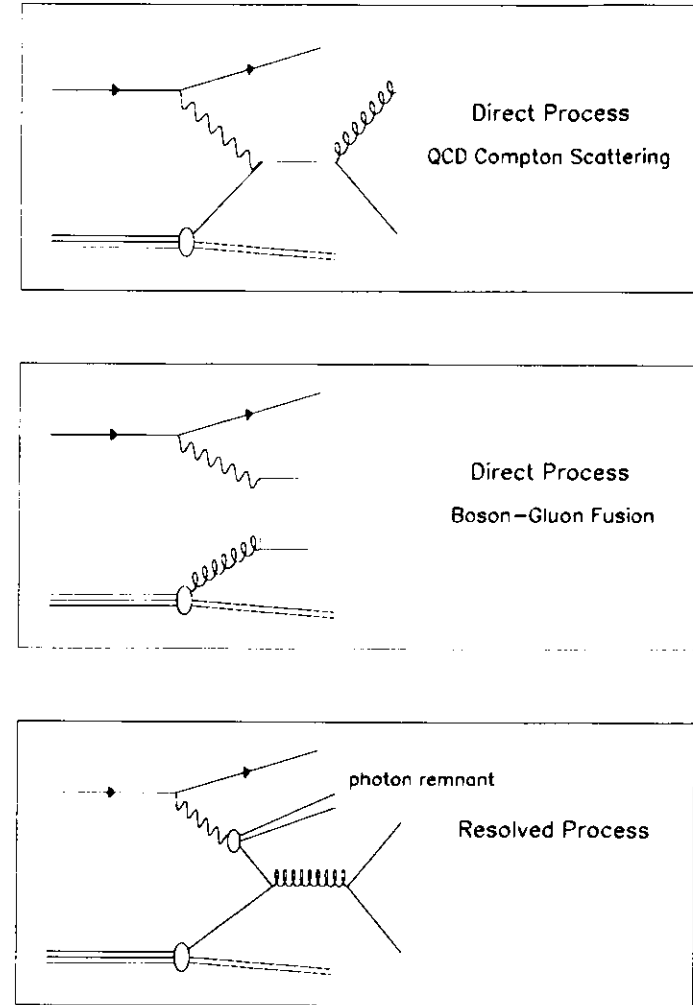
Figure 2.8:
(a) QCD Compton-scattering, (b) boson-gluon fusion, (c) resolved photoproduction.

this work the differential dijet cross section $(d\sigma/d\eta)_{\eta_1,\eta_2}$ with two jet rapidity entries per event are discussed, where a dijet event is in this paper defined by:

- two or more jets with a minimum transverse energy $E_{t,jet} > 6\,\text{GeV}$,

- if more than 2 jets, then take the 2 jets with the highest transverse energy.

The following additional conditions are:

- rapidity $1 < \eta_{jet} < 2$

- $0.15 < y < 0.8$ and $Q^2 < 4\,\text{GeV}^2$.

A discussion of the used kinematic region will be given in chapter 6.

2.3.2   Reconstruction of the parton kinematics

In order to study the partonic structure of the photon, it is desirable to reconstruct the initial state parton kinematics, given by the longitudinal momentum fraction of the proton x_p and the photon x_γ carried by the interacting partons and y, which can be measured using the Jacquet-Blondel method.

The conventional reconstruction method of x_γ

In a conventional jet analysis the Bjorken-x of the photon and the proton can be reconstructed by measuring the jets, which are associated with the hard interacting partons. The leading-log picture of hard photoproduction is described by a $2 \to 2$ scattering process with momenta $x_p E_p$ and $x_\gamma y E_e$ of the incoming partons. Assuming that the dijet kinematics is completely determined by the two scattered partons, without any additional effects, both x-values can be deduced from the simple two body scattering dynamics with the result

$$x_\gamma^{meas} = \frac{1}{2yE_e}(E_{t,jet1}\exp(-\eta_{jet1}) + (E_{t,jet2}\exp(-\eta_{jet2})) \qquad (2.76)$$

$$x_p^{meas} = \frac{1}{2E_p}(E_{t,jet1}\exp(\eta_{jet1}) + (E_{t,jet2}\exp(\eta_{jet2})) \qquad (2.77)$$

where $E_{t,jet1}$, $E_{t,jet2}$ and η_{jet1}, η_{jet2} are transverse energies and rapidities of the two highest E_t-jets in the event. The measured dijet x-values are denoted by x_γ^{meas} and x_p^{meas}. The relationship between x_γ^{meas} and the true leading order x_γ depends

upon how well the event structure is described by LO QCD. Another form of these equations, where a measurement of y_{JB} is used to evaluate the photon energy is

$$x_\gamma^{meas} = \frac{\sum_{jets}(E - E_z)}{\sum_{had}(E - E_z)} \qquad (2.78)$$

$$x_p^{meas} = \frac{\sum_{jets}(E + E_z)}{2E_p} \qquad (2.79)$$

where the sum in the denominator of equation (2.78) runs over all final state hadrons. In the following, Equ. 2.76 and Equ. 2.77 are taken, because of the explicit dependence on jet rapidities and jet momenta. Both pairs of equations follow from the conservation of energy and longitudinal momentum. For massless partons one has

$$x_p E_p + y x_\gamma E_e = E_1 + E_2 \qquad (2.80)$$

$$x_p E_p - y x_\gamma E_e = E_1\cos\theta_1 + E_2\cos\theta_2 \qquad (2.81)$$

where the left and right side come from the initial and the final state, respectively. The energy of the outgoing partons is denoted by E_1 and E_2. Subtraction and addition of both equations lead to

$$x_\gamma = \frac{1}{2yE_e}(E_1(1 - \cos\theta_1) + E_2(1 - \cos\theta_2)) \qquad (2.82)$$

$$x_p = \frac{1}{2E_p}(E_1(1 + \cos\theta_1) + E_2(1 + \cos\theta_2)) \qquad (2.83)$$

which directly give equations 2.78, 2.79, where y is replaced by the Jacquet-Blondel expression 2.9. Equ. 2.76 and Equ. 2.77 follow using the definition of η and

$$\tan\frac{\Theta}{2} = \frac{(1 - \cos\Theta)}{\sin\Theta} = \frac{\sin\Theta}{(1 + \cos\Theta)} . \qquad (2.84)$$

Reconstruction of x_γ using the photon remnant

In the case of the resolved process, the dijet system of the hard scattering is accompanied by a photon remnant with an energy deposition close to the direction of the incoming electron. After a hard interaction, where the photon-parton carries the energy $x_\gamma E_\gamma$, the photon remnant is left with

$$E_{rem} = (1 - x_\gamma)E_\gamma = (1 - x_\gamma)yE_e$$

In principle, a measurement of the remnant energy allows the calculation of x_γ without any knowledge about the final jet configuration. This is an interesting possibility, in particular for low-x_γ events with a high probability that one jet is not in the accepted rapidity region of the detector. But in practice, it is very difficult to measure the remnant energy with satisfactory precision, because a large amount of remnant energy can leave undetected through the beam pipe. D'Agostini and Monaldi [28] proposed a method, where the final jets and a measurement of the photon remnant energy are used to calculate x_γ in an iterative procedure. In the final state two hadronic invariant masses are of importance: the first, the hard scattering invariant mass $\hat{s}$, is given by the four momenta of the two hard jets $\hat{s} = (p_{jet1} \cdot p_{jet2})^2$ and the other one $\bar{s} = (p_{jet1} + p_{jet2} + p_{rem})^2$ in addition includes the photon remnant. Using these masses, one obtains the two relations

$$x_\gamma = \frac{\hat{s}}{\bar{s}} \tag{2.85}$$

$$x_p = \frac{\bar{s}}{ys}. \tag{2.86}$$

The idea is to artificially add a remnant jet with the four momentum $p_{rem} = (E_{rem}, 0, 0, -E_{rem})$ to calculate $\bar{s}$. A first approximation of the remnant energy is given by the total energy backward of the hard jets, the so-called backward energy E_{back}. It is defined by the energy collected in a cone around the beam pipe with

$$\eta < min(\eta_{jet1}, \eta_{jet2}) - \Delta\eta, \tag{2.87}$$

where $\Delta\eta = 1$ is selected to exclude the energy deposition of the most backward scattered jet. Setting $E_{rem} = E_{back}$ a first value of x_γ can be found, which is taken to determine a more precise remnant energy $E_{rem} = (1 - x_\gamma)yE_e$ and the new four momentum of the remnant jet. Repeating this procedure, after a few iterations leads to a stable determination of x_γ and x_p.

Separation of direct and resolved events by the backward energy

It is natural to expect that the backward energy can be used to separate resolved and direct contributions. Indeed, it should be possible to separate a resolved sample by a simple cut on E_{back}. But in the case of the direct sample, such a cut is not able to reject the resolved high-x_γ contamination. The problem with this method is the measurement of E_{back} in high-x_γ events with one jet close to the beam pipe. In this case, the most backward scattered jet and the remnant overlap in the same rapidity region. A separation of the remnant energy from the energy flow of the jet is not possible with the simple cone definition of equation 2.87, which works only well, if the

most backward scattered jet is well separated from the photon remnant. For events with low-η jets, the cone condition leads to very small values of E_{back}, the signature of direct events. On the other hand, the separation of a resolved sample by an E_{back}-cut is characterized by the suppression of high-x_γ events. Therefore, it works similar to an x_γ-cut, and both separation methods should lead to comparable results.

2.4 Direct and resolved processes in NLO QCD

In the previous section, hard photoproduction has been discussed in lowest order and a simple expression 2.76 for the computation of x_γ has been derived. The meaning of the direct and resolved processes is well defined. Neglecting smearing and acceptance effects, in the direct case all of the photon momentum is transformed to the jets with

$$x_\gamma = 1$$

while events with

$$x_\gamma < 1$$

are referred to resolved photoproduction. In the next-to-leading order (NLO) perturbation theory, the situation is more complex, and direct and resolved processes cannot be interpreted unambiguously. The signature of the next-to-leading order calculations is the occurrence of a third jet, so that x_γ cannot be extracted from simple elastic two body scattering. In $2 \to 3$ processes the simple definition of the hard process, as in the leading-log diagrams of figures 2.8, is not possible and must be done more carefully. The first order $\mathcal{O}(\alpha\alpha_s)$ direct diagrams

$$\gamma q \to qg$$

$$\gamma g \to q\bar{q}$$

are changed to next order $\mathcal{O}(\alpha\alpha_s^2)$ diagrams, where an extra parton is added.

$$\gamma q \to qgg$$

$$\gamma g \to q\bar{q}g$$

$$\gamma q \to q q\bar{q}$$

A diagram of the last process is shown in figure 2.9(a). Bodwin and Repond [33] used it to discuss next-to-leading order ambiguities in the definition of the direct and
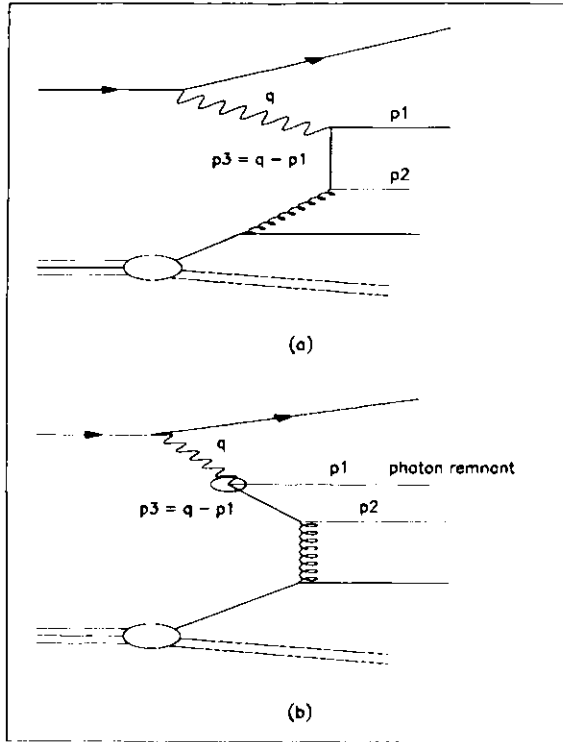
Figure 2.9: Direct versus resolved photoproduction
The figure shows two different interpretations of the same scattering process. Figure (a) represents a next-to-leading order direct process, which can be interpreted also as resolved dijet production, figure (b).

resolved process. The following is a short summary of their analysis. With $2 \to 3$ subprocesses one encounters soft divergences and collinear divergences, which require the distinction of hard photoproduction into a direct and a resolved contribution. This separation is essential to absorb collinear singularities in the parton distribution of the photon. The hardness of the process in Fig. 2.9(a) is given by the squared four momentum of the internal line $p3$. If p_{1t} is large, the balancing p_{3t} is far off mass shell, and Fig. 2.9 shows a $2 \to 3$ hard scattering process. If p_{1t} is small and approximately collinear to q, p_{3t} is also small and close to mass shell. Thus a collinear divergence

results for $p_{1t} \to 0$. The singularity must be factorized so that it can be absorbed in the bare quark distribution of the resolved process, shown in figure 2.9(b).

The distinction between the $\mathcal{O}(\alpha, \alpha_s^2)$ direct process and the resolved two jet production is given roughly by the factorization scale μ_{fac}, that appears in structure functions of higher order processes. A simple division into resolved and direct photon contribution can be made by:

$$p_{1t} < \mu_{fac} \qquad \text{resolved process}$$

$$p_{1t} > \mu_{fac} \qquad \text{direct process}$$

This distinction is somewhat arbitrary and depends on the factorization scheme and scale. The discussed example is one of a class of next-to-leading order graphs, which can contribute to both, direct and resolved processes.

Beside theoretical complications, Equ. 2.76 for x_γ is not correct for the kinematics of a $2 \to 3$ scattering. Using this formula for the next-to-leading order diagrams, the direct peak at $x_\gamma = 1$ is reduced and smeared out. A more satisfactory description by use of all jets becomes very difficult because a large part of all $2 \to 3$ events will have a jet outside the accepted η-region. Nevertheless, Equ. 2.76 remains a well defined quantity strongly related to the hard scattering, which can be used as an approximation of the true x_γ.

Next-to-leading order calculations

At the time of the analysis of this work, next-to-leading order calculation of dijet photoproduction were not available for a comparison with the measured dijet cross section $(d\sigma/d\eta)_{\eta_1,\eta_2}$ presented in this work. However, recent calculations from Klasen et al. [34] for the inclusive NLO jet cross section $d\sigma/d\eta$ using events with

- transverse jet momenta $E_t > 8\,\text{GeV}$

- $0.20 < y < 0.85$, $Q^2 < 4\,\text{GeV}^2$

have shown that NLO effects lead to an increase of the inclusive cross section of approximately 20 - 30 % in the rapidity range $-1.5 < \eta < 2.5$ as compared with LO predictions. Due to the similarity of the kinematic region, one can expect that the influence of NLO effects in the present dijet analysis can be roughly estimated by a correction factor (the so-called K factor) of 1.2–1.3.

Resolved and direct contributions in NLO QCD

As a consequence of higher order effects, Owens [35] suggested to put less emphasis on the decomposition into a resolved and a direct contribution. These are convention

and cut dependent. However, for some applications it is very fruitful to carry out the decomposition. For instance, the phenomenon of multiple interactions (see the discussion of the next section) is related to the resolved process and does not appear in the direct process.

The current technique to separate both processes can be summarized as follows:

1. select a sample of 2-jet events

2. measure the x_γ-distribution using Equ. 2.76

3. separate the sample into a direct and a resolved part by an x_γ-cut, where high-x_γ and low-x_γ samples are dominated by direct and resolved processes, respectively.

Another approach for the decomposition is given by Owens [35]. He suggests a method which is based on the energy deposition in a cone of radius R around the direction of the incoming photon in the γp-c.m. system or in the laboratory frame [36]. This kind of separation leads to two classes of events, and each cross section can be divided into:

$$\sigma_{inc} = \sigma_{iso} + \sigma_{acc} \qquad (2.88)$$

where *acc* and *iso* stand for accompanied and isolated to characterize the energy deposition in the cone. If the hadronic energy E_h inside the cone exceeds a fraction ϵ of the photon energy, the event is counted in σ_{acc} and vice versa. The decomposition of both classes is given by:

$$\sigma_{acc} \;:\;\; E_h > \epsilon \cdot E_\gamma \qquad (2.89)$$

$$\sigma_{iso} \;:\;\; E_h < \epsilon \cdot E_\gamma \qquad (2.90)$$

This separation is theoretically well defined by ϵ and R. Similar to the x_γ decomposition one expects that each class is dominated by one type of hard photoproduction processes:

$$\sigma_{acc} \;\approx\; \sigma_{res}$$

$$\sigma_{iso} \;\approx\; \sigma_{dir}$$

where σ_{res} and σ_{dir} are the pure theoretical resolved and direct cross sections. A specific advantage of this method is the possibility that it can be applied to all types of jet-events; 1-jet, 2-jet, 3-jet, ... , since no kinematic jet calculation is necessary.

2.5 Multiple Interactions

In this section a discussion of the so-called multiple interactions is presented. Multiple Interactions (MI) are hard interactions in a hadron-hadron collision, where more than one parton pair undergoes a hard scattering. They are imperfectly understood, and there are only a few models available to simulate the behaviour of this phenomenon. One of the first models was the multiple interactions scenario of Sjöstrand and Van Zijl [37], developed for hadron-hadron collisions and also valid for the resolved photon-proton process. An implementation of this model for the resolved process is available in the multi purpose Monte Carlo generator PYTHIA 5.7 and the main ideas of this concept are given in this section.

In the kinematic region studied in this work, the photon and the proton are probed down to $x_\gamma \approx 0.1$ and $x_p \approx 0.003$, respectively, where the parton densities can be very high. Due to the high number of partons, there exists a significant probability for several hard scatterings in a single hadron-hadron collision. A nonperturbative approach to describe the overall hadronic activity is the concept of soft underlying events, where inelastic, non-diffractive hadron-hadron interactions are described by a hard scattering in addition with a nonperturbative soft collision of the hadron remnants. In contrast to this empirical model, the attempt of Sjöstrand and Van Zijl was driven by the idea to give the total rate of hard parton-parton interactions by a perturbative QCD computation, which requires an extrapolation of high-p_t interactions into the low-p_t region.

The description of multiple interactions is mainly based on the assumptions that the total rate of parton-parton interactions as a function of the transverse momentum scale p_t is given by perturbative QCD, and it is assumed that the different pairwise interactions take place essentially independently of each other. The first assumption leads to the cross section of a hard parton-parton scattering, given by

$$\sigma_{hard}(s_{\gamma p}) \sim \int_{p_{t,min}^2}^{s/4} \frac{d\sigma}{dp_t^2} dp_t^2. \qquad (2.91)$$

In addition to the use of a sharp cut-off $p_{t,min}$, the Sjöstrand–Van Zijl model provides also a continuous regulariztion of σ_{hard} by substitution of $d\sigma/dp_t^2$, which diverges at the low limit like $1/p_t^4$, by $(d\sigma/dp_t^2) \cdot p_t^4/(p_{t,o}^2 + p_t^2)^2$ to remove the $1/p_t^4$ behaviour and an evaluation of α_s at the scale $(p_{t,o}^2 + p_t^2)$. These substitutions allow a continuous p_t spectrum from $p_t = 0$ to $p_t = \sqrt{s}/2$ and recover the standard perturbation cross section for $p_t >> p_{t,o}$. The $p_{t,o}$ scale is one of the main parameters of the Sjöstrand model. It is of the same order of magnitude as the cut-off $p_{t,min}$. A comparison with the measured mean charged multiplicity at the CERN S$p\bar{p}$S led to values of $p_{t,o}$ between 1.3 GeV and 2.0 GeV with a slow dependence on the c.m. energy [37].

Multiple Interactions and the total photoproduction cross section

The basic idea of multiple interactions is strongly connected with the behaviour of the total photoproduction cross section σ_{tot} at high energies. Therfore, it is instructive to discuss the phenomena of multiple interactions together with the total photoproduction cross section and the various models which are used to describe this cross section as a function of the photon-proton center-of-mass energy $\sqrt{s_{\gamma p}}$. Most of these models are based either on a phenomenological Regge-type approach, or on perturbative QCD predictions.

In Regge-type inspired models the total photoproduction is treated similar to hadron-hadron interactions and can be parameterized in the form [8]:

$$\sigma_{tot}^{\gamma p}(s_{\gamma p}) = X \cdot s_{\gamma p}^{\epsilon} + Y \cdot s_{\gamma p}^{-\eta} \tag{2.92}$$

where ϵ and η are universal parameters in the description of pp, $\pi^{\pm}p$, $K^{\pm}p$ and γp scattering with fit values of $\epsilon \approx 0.0808$ and $\eta \approx 0.4525$. The parameters X and Y depend on the specific process. A fit to existing fixed target photoproduction data below $\sqrt{s_{\gamma p}} < 20\,\mathrm{GeV}$ leads to

$$\sigma_{tot}^{\gamma p}(s_{\gamma p}) = 67.7\, s_{\gamma p}^{\epsilon} \cdot 129\, s_{\gamma p}^{-\eta} , \tag{2.93}$$

where $s_{\gamma p}$ and $\sigma_{tot}^{\gamma p}$ are given in units of GeV^2 and μb, respectively. The predicted value at 200 GeV is $160\,\mu b$ which is in good agreement with the data published by H1 $(159 \pm 7 \pm 20\,\mu b)$ and ZEUS $(154 \pm 16 \pm 32\,\mu b)$, at about the same energy.

In the perturbative QCD motivated models [38] $\sigma_{tot}^{\gamma p}$ is calculated using the perturbative QCD cross section of Equ. 2.91. The so-called additive models calculate $\sigma_{tot}^{\gamma p}$ simply by adding together a non-perturbative (soft) and the perturbative QCD contributions. In this description the cross section grows rapidly with increasing center-of-mass energy and depends strongly on the resolved photon parametrization and the choice of the cut-off value $p_{t,min}$. Using the Drees Grassie photon parametrization the total photoproduction cross section measured at ZEUS becomes comparable with the prediction of the additive model for $p_{t,min} > 2\,\mathrm{GeV}$, while the LAC1 photon parametrization leads also for $p_{t,min} = 2\,\mathrm{GeV}$ to a drastic rise not described by the data, see [39].

The additive model assumes that one can obtain the total cross section by the sum $\sigma_{tot} = \sigma_{soft} + \sigma_{hard}$ ignoring the possibility of more than one parton-parton interaction per event. As shown by Forshaw and Storrow [40] the rise in the γp total photoproduction cross section for $s_{\gamma p} > 100\,\mathrm{GeV}$ is considerably reduced including multiple interactions and *shadowing* of the gluon density distribution.

The total photoproduction cross section can be subdivided into an elastic σ_{el}, a single-diffractive σ_{SD}, a double-diffractive σ_{DD} and the inelastic, non-diffractive cross

section σ_{ND}.

$$\sigma_{tot}(s_{\gamma p}) = \sigma_{el}(s_{\gamma p}) + \sigma_{SD}(s_{\gamma p}) + \sigma_{DD}(s_{\gamma p}) + \sigma_{ND}(s_{\gamma p}) \tag{2.94}$$

The perturbatively calculated QCD cross section is part of the non-diffractive, inelastic cross section σ_{ND}, which contains contributions of high-p_t events with visible jet structures and (soft) events without any visible jet activity, $\sigma_{ND} = \sigma_{soft} + \sigma_{hard}$. This subdivision depends of course strongly on the choice of $p_{t,min}$. As mentioned above, Equ. 2.91 diverges for $p_{t,min} \to 0$. Since the multiple interactions approach extrapolates the high-p_t interactions into the low-p_t region, this will lead to $\sigma_{hard} > \sigma_{ND}$ and $\sigma_{soft} = \sigma_{ND} - \sigma_{hard} < 0$, which seems to be a contradiction. However, note that σ_{hard} is a parton-parton cross section, while σ_{ND} gives a photon-proton cross section. Each of the incoming hadrons (resolved photon and proton) consists of many partons, with the possibility of heaving several parton-parton interactions.

In order to ensure $\sigma_{soft} \geq 0$ allowing simultaneously $\sigma_{hard} > \sigma_{ND}$ a number of parton-parton interactions must be distributed among a smaller number of non-diffractive, inelastic events. In this model the average number of hard interactions per event is given by the ratio

$$< n_{int}(s_{\gamma p}) > = \frac{\sigma_{hard}(s_{\gamma p}, p_{t,min})}{\sigma_{ND}(s_{\gamma p})} . \tag{2.95}$$

Assuming independent pairwise interactions the number of scatterings in a photon-proton collision is given by a Poissonian distribution with mean $<n_{int}(s_{\gamma p})>$.

Fig. 2.10 shows the distribution of the number of parton-parton interactions per event for dijet events with transverse jet energies $E_t > 6\,\mathrm{GeV}$ in the kinematic region defined by $Q^2 < 4\,\mathrm{GeV}^2$, $\sqrt{s_{ep}} = 296\,\mathrm{GeV}$, $0.2 < y < 0.8$ and $1 < \eta_{jet1,jet2} < 2$.

The simple model

In the simple approach of the Sjöstrand model it is not necessary to use a continuous regularization as described above. The average number per event $< n_{int}(s_{\gamma p}) >$ is calculated using a sharp cut-off of $p_{t,min} = 1.4\,\mathrm{GeV}$. For the use of Monte Carlo generators the scatterings are arranged in a falling sequence according to $x_t = 2p_t/\sqrt{s}$, where $\hat{s}$ is the invariant mass of the parton-parton system:

$$x_{t,1} > x_{t,2} > \ldots > x_{t,n} > x_{t,min} \tag{2.96}$$

with $x_{t,min} = 2p_{t,min}/\sqrt{\hat{s}}$. The probability of a parton-parton interaction at x_t in a non-diffractive, inelastic collision is given by the probability distribution $f(x_t)$,
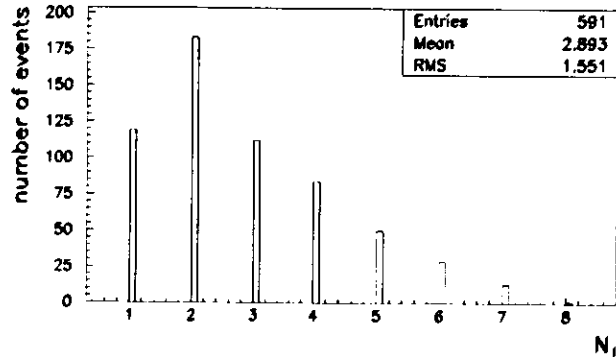
Figure 2.10: Distribution of the number of parton-parton interactions per event for resolved photoproduction dijet events in the kinematic range $132\,\text{GeV} < \sqrt{s_{\gamma P}} < 265\,\text{GeV}$ and transverse jet energies $E_t > 6\,\text{GeV}$ in the rapidity range $-1 < \eta_{\text{jet1,jet2}} < 2$. Photon and proton are parameterized by the GRV-LO and MRSD- parton distributions.

see [41], which is defined by analogy with the differential QCD cross section $d\sigma/dp_t$:

$$f(x_t) = \frac{1}{\sigma_{ND}} \frac{d\sigma}{dx_t} \tag{2.97}$$

For the hardest scattering, the ordinary structure function is used, while the subsequent interactions depend on the x values and flavours of all preceding scatterings. The standard procedure in PYTHIA considers the decreased hadron energy of the subsequent scatterings by the evolution of the structure function at the rescaled value

$$x_i' = \frac{x_i}{\sum_{j=1}^{i-1} x_j}. \tag{2.98}$$

A model with varying impact parameter

In the simple model it has been assumed that the initial state of all collisions is independent of the hadron structures. In a more sophisticated approach, each hadron is described by a spatial distribution of the hadronic matter, and the probability of a parton-parton interaction depends on the time-integrated overlap $\tilde{O}$ of both hadrons.

This picture is equivalent to classical scattering of two clouds of point-like particles, where the scattering rate depends on the impact parameter b. For a collision with the impact parameter b the time-integrated overlap is given by:

$$\tilde{O}(b) = \int\int d^3x\, dt\, \rho_{\text{boosted}}\left(x - \frac{b}{2}, y, z - vt\right) \cdot \rho_{\text{boosted}}\left(x + \frac{b}{2}, y, z + vt\right) \tag{2.99}$$

where v is the velocity in the c.m. frame and ρ_{boosted} is the Lorentz contracted matter distribution. After comparison of several distributions, a spherically symmetric double Gaussian was chosen by Sjöstrand and Zijl:

$$\rho(r) \sim (1-\beta)\frac{1}{a_1^3}\exp\left(-\frac{r^2}{a_1^2}\right) \cdot \beta\frac{1}{a_2^3}\exp\left(-\frac{r^2}{a_2^2}\right) \tag{2.100}$$

a distribution with a small core region of radius a_2 embedded in a large hadron of radius a_1. This matter distribution can be seen as a realization of the chiral bag model, where a hard hadronic core is surrounded by a cloud of pions. The number of scatterings $\bar{n}(b)$ as a function of b depends on the overlap $\tilde{O}(b)$ where it is assumed that the relationship is a linear one, with

$$< \bar{n}(b) > = k\tilde{O}(b) \tag{2.101}$$

The absolute normalization of $\tilde{O}(b)$ does not enter in the calculation, since the total inelastic, non-diffractive hadron-hadron cross section is taken from literature and is not calculated from the matter distribution $\rho(r)$. Therefore, it makes sense to define an enhancement factor

$$e(b) = \frac{\tilde{O}(b)}{<\tilde{O}>} \tag{2.102}$$

which describes the variation of $\tilde{O}(b)$ by comparison with the average $<\tilde{O}>$. The definition of the average is not unambiguous, and the exact meaning can be found in [37]. The enhancement factor $e(b)$ is used to generalize the probability $f(x_t)$, which is replaced by

$$f(x_t, b) = e(b)f(x_t) \tag{2.103}$$

where the probability of an interaction at x_t with an impact parameter b appears in a factorized form. This property is used extensively in the event-generation formalism of PYTHIA, where now $f(x_t, b)$ is used to find the chain of hard interactions.

Chapter 3

HERA and the ZEUS experiment

3.1   The HERA Storage Ring

The Hadron Electron Ring Accelerator, HERA, located at the DESY (Deutsches Elektronen-Synchrotron) laboratory in Hamburg is the first electron-proton collider in the world. HERA offers the possibility to study electron-proton interactions in a kinematic regime with center-of-mass energies which exceed the values of previous fixed target experiments by an order of magnitude. During the 1993 running period, electrons and protons collided with energies of 26.7 GeV and 820 GeV respectively, resulting in a center-of mass energy of $\sqrt{s} = 296$ GeV. This is equivalent to a 45 TeV electron beam in a fixed target experiment. A plan of the HERA ep-collider with its preaccelerator system and the injection scheme at DESY is shown in Fig. 3.1. Some HERA parameters referring to the 1993 physics runs are listed in Tab. 3.1.
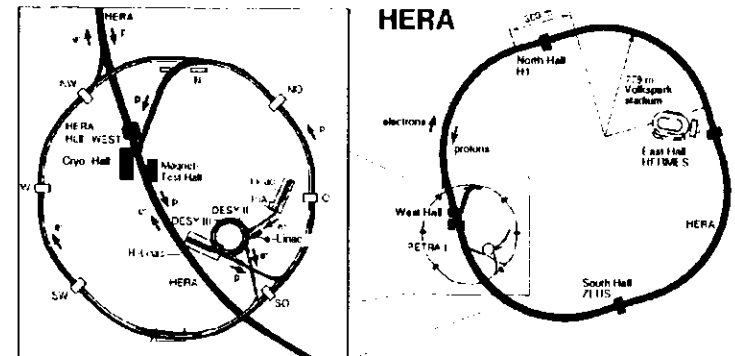

Figure 3.1: Layout of HERA and the injection facilities at DESY

General Parameters of HERA		
Physics start date	1992	
Circumference of the HERA tunnel	6336 m	
Depth underground	10 m · 25 m	
Inner diameter of the tunnel	5.2 m	
Number of pre-accelerators	6	
The HERA Beams	Electron	Proton
Beam energy	26.7 GeV	820 GeV
Injection energy	14 GeV	40 GeV
Center-of-mass energy	296 GeV	
Luminosity	$(0.2-1.6) \cdot 10^{30} cm^{-2} s^{-1}$	
Crossing angle	head-on collisions, 0 rad	
Colliding bunches	84	
Bunch crossing time	96 ns	
Average beam current	13 mA	13 mA
Horizontal beam size σ_x	0.26 mm	0.29 mm
Vertical beam size σ_y	0.07 mm	0.07 mm
Longitudinal beam size σ_z	0.8 cm	11 cm
The HERA Storage Rings		
Main dipoles in ring	456	422
Main quadrupoles in ring	605	224
Magnetic field	0.165 T	4.68 T
Frequency of the rf cavities	500 MHz	52 MHz
		208 MHz

Table 3.1: Parameters of HERA for the 1993 data taking period.

The HERA tunnel has a circumference of 6.3 km and is situated 10-25 m underground. Electrons and protons are guided in two separate storage rings which cross each other in the three interaction points and are used for the experiments ZEUS (Hall South) and H1 (Hall Nord). Hall East has been allocated to the HERMES experiment, which is presently under construction.

One of the remarkable features of the HERA collider, which distinguishes HERA from other conventional collider, are the asymmetric beam energies. While the high momentum of the proton beam requires superconducting magnets, the electrons are controlled with conventional magnets. The HERA proton ring consists of 422 main dipoles delivering a bending field of 4.68 T and 224 main quadrupoles. Standard cells of 47 m length combining 4 dipoles, 4 quadrupoles, 4 sextupoles and correction magnets are installed in the arcs of the proton ring and are cooled down to 4.2 K.

The conventional electron ring consists of 456 main dipoles of 0.164 T and 605 main quadrupoles grouped in 12 m long magnet modules which contain one dipole, one quadrupole, one or two sextuploes and several correction dipoles. The energy loss

due to synchrotron radiation is compensated by 500 MHz copper cavities installed in the straight sections of HERA. In addition 16 superconducting 4-cell cavities with an field gradient of 5 MV/m are used to accelerate the electrons from 14 GeV (injection energy) to the maximum energy of 26.7 GeV.

The HERA injection system as shown in Fig. 3.1 is based on a chain of preaccelerators including the ring accelerators DESY and PETRA. Electrons or positrons are pre-accelerated in the linear accelerators LINAC I (220 MeV) or LINAC II (450 MeV) followed by an acceleration up to 9.0 GeV in the DESY II synchrotron. Then the electrons are transferred to PETRA where the energy is increased to 14 GeV after which the electrons are injected into the HERA electron ring. The proton injection starts with negative hydrogen ions (H^-) from the 50 MeV Proton Linac. After stripping off the two electrons, the protons are accelerated via DESY III and PETRA to 7.5 GeV and 40 GeV, respectively, which is the injection energy for the HERA proton ring.

The electrons and protons are stored in separate bunches with a distance of 28.8 m between two successive bunches. This distance corresponds to a bunch crossing time of 96 ns. In order to achieve an adequate luminosity each ring can be filled with 210 bunches of particles. During the 1993 data taking period 84 paired bunches were used together with 10 unpaired electron and 6 unpaired proton bunches, the so-called pilot bunches, which have been used to study beam-gas induced background events.

3.2 The ZEUS Experiment

The ZEUS detector is a large multipurpose detector designed to study the wide spectrum of HERA physics observed in electron-proton scattering. A summary of the HERA physics topics, their typical signatures, the necessary detection methods and equipment, and the ZEUS specification of these detectors is given in ref. [42]. A schematic view of the ZEUS detector is shown in Fig. 3.2. Cross sectional views of the ZEUS detector perpendicular and parallel to the beam axis are presented in Fig. 3.3. The essential subcomponents of the detector for particle identification, tracking measurements, energy measurements and beamgas suppression are:

- The inner tracking systems:
  - Vertex Detector (VXD)
  - Central Tracking Detector (CTD)
  - Transition Radiation Detector (TRD)
  - Forward and Rear Tracking Detectors (FTD, RTD)
- Hadron Electron Separator (HES)
- High Resolution Calorimeter (CAL)

- Backing Calorimeter (BAC)

- Muon Detection (MUON)

- Leading Proton Spectrometer (LPS)

- Luminosity Monitor (LUMI)

- Vetowall

- C5 counter

A complete technical description of the detector is given in [43]. The detector components can be divided into the inner tracking system with VXD, CTD, TRD, FTD, RTD located in the magnetic field of the superconducting magnetic solenoid which surrounds the central drift chamber and parts of the central tracking and transition detectors, the high resolution calorimeter outside the magnetic field of the superconducting solenoid with the forward (FCAL), barrel (BCAL) and rear (RCAL) calorimeter, the iron yoke carrying the backing calorimeter, the barrel and rear muon
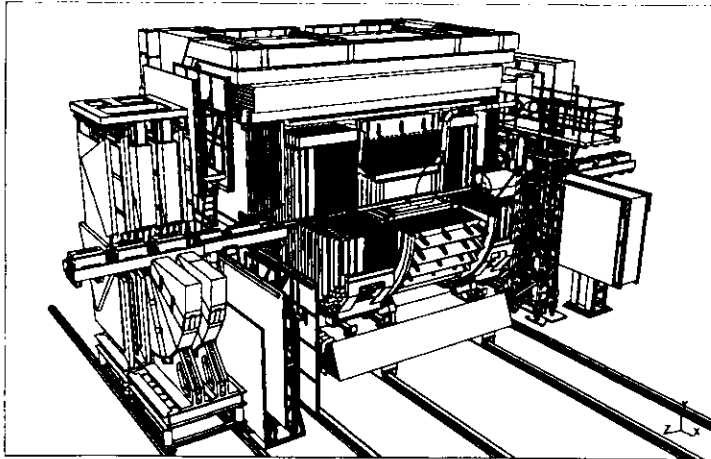
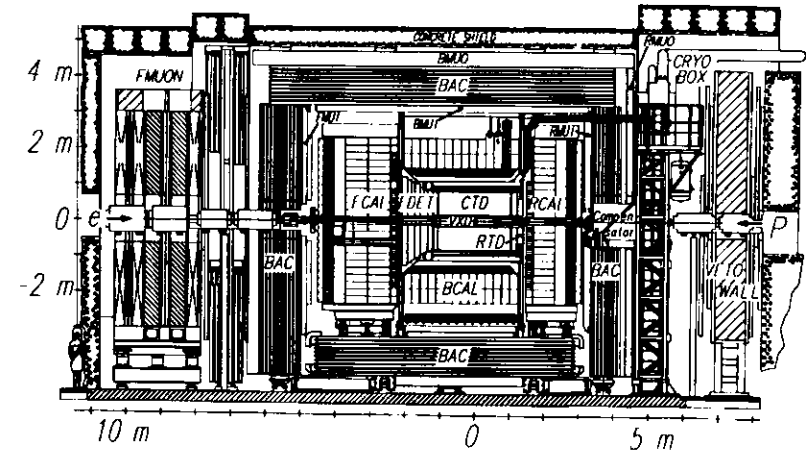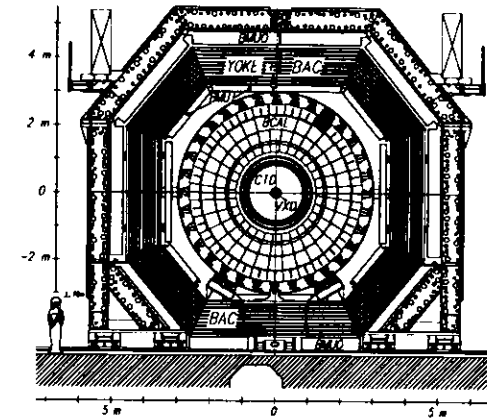Figure 3.2: Schematic view of the ZEUS detector.

Figure 3.3:
Cross section of the ZEUS detector perpendicular and parallel to the beam.

detectors, and finally the detector components outside the central detector such as the forward muon detector (FMUON), the vetowall and the components along the beam pipe such as the LPS and the LUMI detector.

In this chapter, only the components used for the analysis of jet photoproduction are described in some detail. These are the inner tracking chambers VXD and CTD, the high resolution calorimeter CAL, the luminosity monitor and the components for beam-gas suppression, the Vetowall and the C5 counter.

3.2.1 Detector Components

The Vertex Detector

The main purpose of the vertex detector (VXD) is the detection of short-lived particles which give rise for secondary vertices and the improvement of the vertex determination combining the information of the vertex detector and the central drift chamber. The VXD is a high precision drift chamber with 3000 drift wires, 1560 field wires and 1440 sense wires parallel to the beam axis. The drift chamber is divided into 120 cells which surround the beam pipe axis at a distance of 99 mm cylindrical with an active radial length of 36 mm and an active wire length parallel to the beam pipe of 1590 mm. The drift chamber is filled with dimethylether (DME) to attain a slow drift velocity ($5 \mu m/ns$) for the electrons which allows a spatial resolution of $35 \mu m$. The vertex detector covers the angular region between $8.6°$ and $165°$ with respect to the beam axis.

The Central Tracking Detector

The central tracking detector (CTD) is used to reconstruct tracks of charged particles at polar angles from $15°$ to $164°$. The CTD is a cylindrical drift chamber with nine planes of wires called super-layers, each with eight planes of sense wires constructed in a cylindric shape. The detector is 2.41 m in length and has an inner/outer radius of 16.2/85.0 cm. Fig. 3.4 shows one octant of the the wire layout. The odd numbered superlayers have wires parallel to the beam axis while the even ones are tilted by small stereo angles of approximately $\pm 5°$ to allow a three dimensional reconstruction of tracks. The design resolution in the r–ϕ plane is about 100–120 μm depending on the polar angle θ and 1.0–1.4 mm in the z direction. The momentum resolution at 90 degrees is $\sigma_p/p = 0.0021 p\,[\mathrm{GeV}] \div 0.0029$.

The C5 Counter and the Vetowall

The Vetowall detector consists on an iron wall located about 7.5 m upstream the interaction point near the tunnel exit and two scintillator counters on both sides of the wall. The Vetowall serves as an absorber to protect the detector against particles from the beam halo produced by interactions of the protons with the residual gas in the vacuum pipe. Particles, which pass through the iron wall, can be detected by the
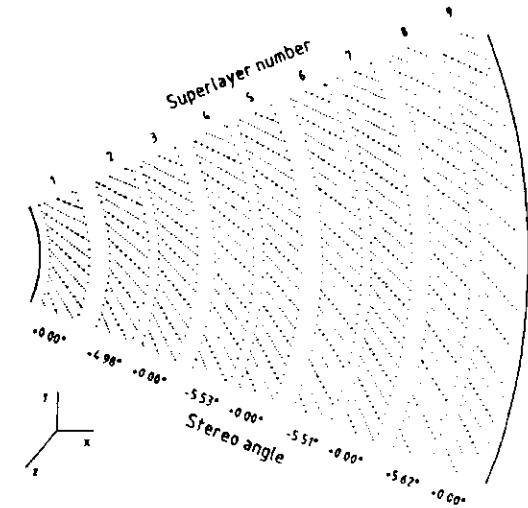
Figure 3.4: Wire layout of the Central Tracking Detector for one octant.

scintillator counters. If these particles arrive in coincidence with the proton beam bunch the position of the passing particles is estimated and these information can be used to reject beam-gas induced events.

The ring counter C5 Counter is made of two lead-scintillator sandwich counters and is situated at position $z = -3.15$ m. This counter is used to measure timing and longitudinal spread of proton and electron bunches and to register halo particles outside the beam pipe.

The Luminosity Monitor

The measurement of the luminosity is based on the Bethe-Heitler bremsstrahlung process $ep \rightarrow e'p\gamma$. This process has a clean experimental signature, which is the coincidence of a final state electron and a photon at small angles with respect to the electron direction and with an energy sum $E'_e + E_\gamma = E_e$. The final state electron and photon produced under very small angles are measured in electromagnetic calorimeters of the luminosity monitor (LUMI) positioned at 33 m (electron tagger) and 100 m (photon tagger) upstream of the central detector. A layout of the luminosity monitor is given in Fig. 3.5. Final state electrons with energies lower than the beam pipe energy are deflected by beam magnets and hit the electron tagger, while the bremsstrahlung photons leave the the beam pipe at $z = 92$ m.

Figure 3.5:
The layout of the electron and photon branches of the ZEUS luminosity monitor located at 35 m and 108 m downstream from the interaction point. The figure shows the configuration used in the 1992 running period including the carbon filter in front of the photon calorimeter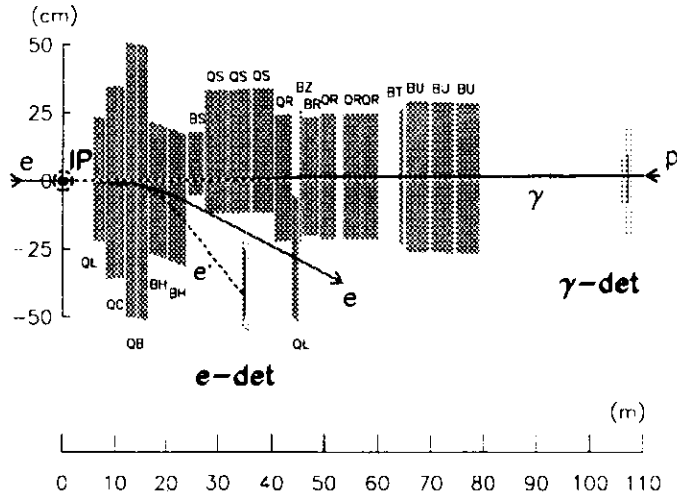 which was removed for the 1993 runs. Dipole (bending) magnets are denoted by B and quadrupoles by Q for the first character.

Studies from the first running in Summer 1992 have shown that the background in the photon calorimeter due to proton halo and other sources is negligible and the coincidence between the electron and the photon calorimeter is not required for the identification of the Bethe-Heitler process. Therefore, the luminosity can be obtained without use of the electron calorimeter from a measurement of $R_{ep}(E_\gamma^{th})$, the rate of ep-bremsstrahlung photons above an energy threshold $E_\gamma^{th} = 5\,\text{GeV}$, and $\sigma_{ep}^{acc}(E_\gamma^{th})$, the corresponding bremsstrahlung cross section calculated from the Bethe-Heitler formula [44] and corrected for the detector acceptance and resolution,

$$L = \frac{R_{ep}(E_\gamma^{th})}{\sigma_{ep}^{acc}(E_\gamma^{th})}.$$ (3.1)

The luminosity monitor allows also the tagging of photoproduction events due to a signal from the electron tagger combined with the absence of an energetic photon measured with the photon tagger. For photoproduction, the electron tagger covers the range from $4 \cdot 10^{-8}\,\text{GeV}^2$ to $2 \cdot 10^{-2}\,\text{GeV}^2$. In this thesis events will be

referred to as *tagged events* if the energy of the scattered electron is in the range $5\,\text{GeV} < E_e' < 25\,\text{GeV}$ and the energy of the photon tagger is below $0.5\,\text{GeV}$.

The High Resolution Calorimeter

In high energy experiments the energy of particles and jets is measured with *calorimeters* which are the central components of the large experiments at present storage rings. One of the essential properties of calorimeters is their sensitivity to both charged and neutral particles. Calorimeters have the attractive capabilities that the energy resolution of the measurement scales with increasing energies as

$$\frac{\sigma(E)}{E} \sim \frac{1}{\sqrt{E}},$$ (3.2)

and that the depth L required to stop incoming particles increases only logarithmically with the particle energy E as

$$L \sim a + b \cdot \ln E.$$ (3.3)

Calorimetry

High-energy particles entering a layer of material produce a cascade of particles. In case of an incoming electron or photon an electromagnetic shower of secondary photons, electrons and positrons is initiated. The shower development depends on the energy of the incoming particle and the absorber material characterized by its specific density, the atomic number Z and the atomic mass A. The longitudinal and transverse shower dimensions are commonly measured in units of the radiation length X_0. The radiation length is the mean distance over which a high-energy electron loses all but $1/e$ of its energy by bremsstrahlung. An appropriate energy scale is given by the *critical energy* E_c which can be defined as the energy where the energy loss of an electron due to bremsstrahlung is equivalent to the energy loss through ionization of the passed matter. Since energy loss of an electron by bremsstrahlung is approximately proportional to its energy and the ionization loss increases only logarithmically, the longitudinal development is determined by the high-energy part of the shower and scales as the radiation length in the material. Good approximations of the radiation length and the critical energy can be parameterized as follows [45]:

$$X_0 \approx 180\frac{A}{Z^2}$$ (3.4)

$$E_c \approx \frac{550}{Z}$$ (3.5)

where X_o is measured in units of $[g/cm^2]$. Using E_c and X_o it is convenient to measure energies and shower dimension by the dimensionless variables $t = x/X_o$ and E/E_c. The maximum number of shower particles initiated by a particle with the energy E is reached at a depth t_{max} which can be approximated by [46]:

$$t_{max} \approx \ln\left(\frac{E}{E_c}\right) \cdot C_i \tag{3.6}$$

with $C_i = 1.1$ ($C_i = 0.5$) for an incoming electron (photon). The length L_{98} after which 98% of the the electromagnetic shower energy is contained in a calorimeter can be approximated by [47]:

$$L_{98} \approx 3 \cdot t_{max}. \tag{3.7}$$

Using Equ. 3.7 and Equ. 3.5 an estimation of the depth required to contain 98% of an electromagnetic shower produced by a 25 GeV electron leads to $L_{98} = 22 X_o$.

In contrast to electromagnetic showers, cascades produced by an incoming hadron are more complex, because in addition to the mentioned electromagnetic processes pure hadronic interactions such as spallation processes and fission of heavy nuclei lead to neutral hadrons, nuclear fragments and excited nuclei so that the measurable signal is reduced due to nuclear binding energy, neutrino production and fragments of nuclei leaving no visible signal in the calorimeter. The length scale appropriate for hadronic showers is the nuclear interaction length λ_{int} defined by $\lambda_{int} = A/N_A \sigma_i$, where N_A is the Avogadro number and σ_i denotes the inelastic cross section. A good approximation of λ_{int} [45] is given by:

$$\lambda_{int} = 35\frac{A^{1/3}}{\rho}[cm] \tag{3.8}$$

where ρ is the density in units of $[g/cm^3]$. The depth required for containment of 95% of the hadronic shower energy is given by the parametrization [48]:

$$L_{95} \approx 0.2\ln E + 2.5\,E^{0.13} + 0.7 . \tag{3.9}$$

with E and L_{95} measured in [GeV] and units of $[\lambda_{int}]$. According to this equation a shower of a 300 GeV hadron can be contained in calorimeter with a depth of 7.1 λ_{int}. The transverse dimension of hadronic showers is small. 95% of the shower energy are located in a cylinder of a radius $R_{95} < \lambda_{int}$.
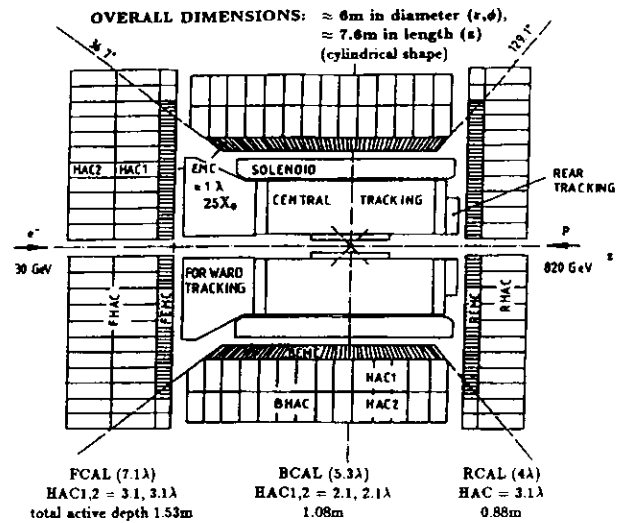
The ZEUS Calorimeter

In practice, the most important types of calorimeters are the *homogeneous* and the *sampling* calorimeters. Homogeneous calorimeters are made of a material that simultaneously absorbs the particle energy and transfers a small fraction of the energy into a measurable signal. Sampling calorimeters are made of alternating passive and active layers where the active layers produce a measurable signal (scintillation light or ionization charge) while the shower is mainly developed in the heavy (high Z) material of the passive layer.

The high resolution ZEUS calorimeter is a compensating sampling calorimeter with equal response to electrons and hadrons ($e/h=1$) using absorber plates of depleted uranium (DU) and plastic scintillator layers for the active plates. The depleted uranium plates are a composition of 98.1% U^{238}, 1.7% Nb and less than 0.2% U^{235}. The optical readout is performed via plastic wavelength shifters, lightguides and photomultipliers. In order to obtain equal calorimeter response to electrons (photons) and hadrons 3.3 mm thick uranium plates corresponding to one radiation length alternate with 2.6 mm thick scintillator plates. For a detailed description of calorimetry and the ZEUS high resolution calorimeter see [42], [49]. Main features of the high resolution calorimeter are:

- hermeticity over the entire solid angle (99.7% of the solid angle are covered)
- energy resolution for hadrons and jets of $\sigma(E)/E = 35\%/\sqrt{E} + 2\%$,
- energy resolution for electrons of $\sigma(E)/E = 18\%/\sqrt{E} + 2\%$,
- calibration of the absolute energy scale to 1%,
- precise angular resolution for particles ($\leq 10\,\text{mrad}$)
- longitudinal segmentation for hadron-electron separation.
- short signal processing time at the nano-second level

The ZEUS calorimeter completely surrounds the solenoid and the inner tracking detectors as shown in Fig. 3.6 and it is divided into three parts: The forward calorimeter (FCAL), the barrel calorimeter (BCAL) and the the rear calorimeter (RCAL) which covering polar angles from $\theta = 2.2°$ to $39.9°$, $\theta = 36.7°$ to $129.1°$ and $\theta = 128.1°$ to $176.5°$, respectively.

The three calorimeter components are structured similar and are subdivided longitudinally into an electromagnetic calorimeter (FEMC, BEMC, REMC) with a depth of $\sim 25 X_o$ equivalent to one interaction length λ, which is sufficient to fully contain the electromagnetic showers, and a hadronic calorimeter (HAC). In FCAL and BCAL the HAC section is divided into two subsections HAC1 and HAC2, while the RCAL has only one HAC section.

OVERALL DIMENSIONS: ≈ 6m in diameter (r,φ),
                     ≈ 7.6m in length (z)
                     (cylindrical shape)

FCAL (7.1λ)   BCAL (5.3λ)   RCAL (4λ)
HAC1,2 = 3.1, 3.1λ   HAC1,2 = 2.1, 2.1λ   HAC = 3.1λ
total active depth 1.53m 1.08m   0.88m

Layout of the ZEUS Uranium Scintillator Calorimeter; FCAL = Forward
Calorimeter, BCAL = Central Calorimeter, RCAL = Rear Calorimeter,
EMC and HAC = electromagnetic and hadronic sections.

Front view of FCAL assembled from   Front view of FCAL with transverse
24 modules of various depth in λ.   segmentation seen from the IP.
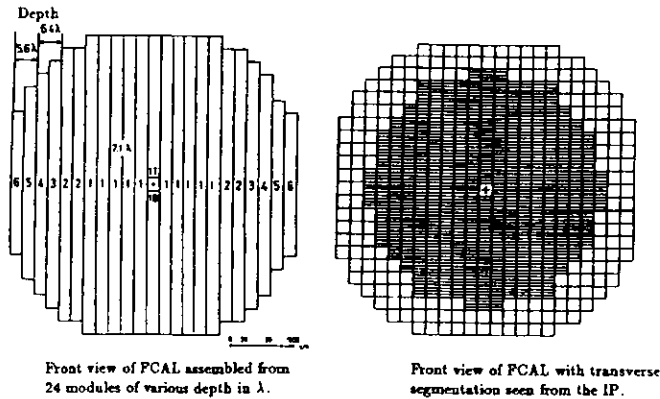
Figure 3.6:
Layout of the high resolution calorimeter and two front views of the FCAL.

The whole calorimeter has a modular structure. The FCAL and RCAL calorimeter consists of 24 modules, which follow the same construction principles, as shown in Fig. 3.7 where an isometric view of a FCAL module is presented. For a detailed description of the BCAL modules see [43]. The FCAL and RCAL modules have the same width of 20 cm and have a height varying from 2.2 m to 4.6 m so that roughly a cylindrical structure with a radius of ≈ 2.3 m can be built. The depth varies from $7.1\,\lambda$ in the central region to $5.6\,\lambda$ for the outer horizontal regions. The centre module of the FCAL and the RCAL calorimeter are splitted into a separate upper and lower module. The horizontal segmentation is determined by the width of the modules. The transverse segmentation depends on the height of the wavelength shifters which collect the scintillator light. Each longitudinal section (EMC, HAC1, HAC2) is read out on both sides by the wavelength shifter. For FCAL the segmentation of the EMC sections is 5×20 cm, and for RCAL 10×20 cm. These sections are called EMC towers. The hadronic towers of FCAL and RCAL have a segmentation of 20×20 cm.

Figure 3.7: Internal structure of an FCAL module.

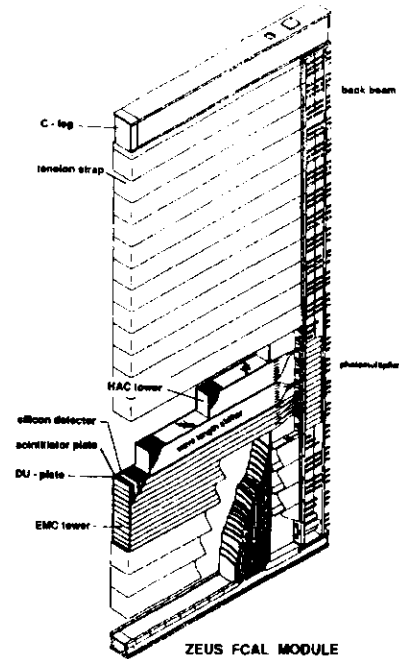Fig. 6.1 shows a front view of FCAL, as seen from the interaction point, assembled from the 24 modules and the same front view including the transverse segmentation of the FCAL. In addition Fig. 3.6 presents a cross section of the calorimeter along the beam pipe and the three calorimeter components FCAL, BCAL and RCAL with their longitudinal segmentation.

Due to the optical readout combined with photomultipliers a fast readout processing can be performed which allows the determination of the arrival times of incoming particles at the nano-second level. This feature can be successfully used to discriminate background events, as described in chapter 4.

The calibration of the calorimeter can be performed using several redundant tools, which are described in [49]. The main calibration source is the use of the natural uranium radio-activity, the so-called uranium noise (UNO), which produce a low background current in the photomultiplier. The integrated signal of the UNO provides a stable diagnostic tool for monitoring and calibration of the high resolution calorimeter.

Chapter 4

Monte Carlo Simulation

The Monte Carlo simulation of events can be divided into two processing steps. In the first step the event kinematics and the production of particles in an ep collision are simulated by MC programs such as PYTHIA [41] or HERWIG [50], so-called *event generators*. The output of an event generator consists of data with the information on particle species and four-momenta of the outgoing particles for each event. This information is used in the second step, the detector simulation, where the detailed simulation of the interaction of the outgoing particles with the detector components is performed in order to determine the detector response.

4.1   Monte Carlo Generation

Hadron production is a process involving QCD processes at large Q^2 ($Q^2 >> \Lambda^2$) which can be calculated in perturbative QCD, and nonperturbative QCD processes at $Q^2 << \Lambda^2$, where one has to rely on QCD inspired phenomenological models. Perturbative QCD processes can be computed in complete 1st, and for some observables like jet rates also in 2nd order α_s. Calculations in 3rd and higher order are still too complicated and not yet performed. For the implementation of matrix element calculations one has to introduce cut-offs to avoid the infrared and collinear divergencies, which cancel only in analytical cross section calculations where virtual corrections can be considered explicitely.

The data, however, show evidence for multijet events with three and more jets. For this reason and because of the difficulties with the divergencies the parton shower (PS) approach is used alternatively or in addition with 2nd order matrix elements to simulate higher order effects. In general, parton shower models are based on the leading-log QCD parton branchings $q \rightarrow qg$, $g \rightarrow qq$, and $g \rightarrow gg$, as shown in Fig. 2.2, which are used to construct the shower by successive branchings.

In high-energy scattering one has to distinguish between initial-state radiation, initiated by the two incoming partons, and final-state radiation of partons after the hard interaction. Initial- and final-state shower evolution are discussed separately,

because their implementations in Monte Carlo programs are formulated by rather different algorithms.

After the perturbative phase the outgoing colored partons must be transformed into colorless hadrons. This nonperturbative long distance effect, the so-called fragmentation, is described by different phenomenological models, where the most important ones are the cluster fragmentation implemented in HERWIG and the string fragmentation of the Lund-group in PYTHIA and JETSET.

In this work, data are compared with Monte Carlo samples of the HERWIG 5.7 and PYTHIA 5.6, (5.7) generators, where the PYTHIA version 5.7 is used to investigate multiple interaction effects. Both programs are general-purpose event generators for a large number of high energy processes, including the resolved and direct process of γp-scattering. The general structure of both generators can be divided into three phases. In the first phase, the hard interaction is calculated according to the leading-log matrix elements. In this phase the only ambiguity is given by the choice of the hard scale $\hat{Q}$. For massless partons, an often used scale in $2 \rightarrow 2$ scattering processes is $\hat{Q}^2 = p_t^2$, with the transverse momentum p_t of the two hard scattered partons. When masses are introduced $\hat{Q}^2$ can be modified to $\hat{Q}^2 = \frac{1}{2}(m_{t3}^2 + m_{t4}^2)$, where m_{t3} and m_{t4} denote the transverse mass $m_t^2 = m^2 + p_t^2$ of the two outgoing partons. But there exist several alternatives in each Monte Carlo generator. For instance, the default hard scattering scale of HERWIG is given by $\hat{Q}^2 = 2 \cdot \hat{s}\hat{t}\hat{u}/(\hat{s}^2 + \hat{t}^2 + \hat{u}^2)$ with the Mandelstam variables $\hat{s} = (p_1 + p_2)^2$, $\hat{t} = (p_1 - p_3)^2$ and $\hat{u} = (p_1 - p_4)^2$, where p_1, p_2 and p_3, p_4 are the four-momenta of the two incoming and the two outgoing partons, respectively.

In the second phase, the evolution of the parton showers is performed using algorithms which differ in some details for the HERWIG and PYTHIA generators. In contrast to the second phase, the formation of hadrons in the third phase is carried out by completely different models. While HERWIG uses the cluster fragmentation model [50], the main fragmentation option in PYTHIA is the Lund string fragmentation [51].

The first two phases of leading oder QCD compton scattering process with initial- and final-state radiation are shown in Fig. 4.1.

4.1.1 QCD-Shower Evolution

The shower evolution is described by the evolution variable t and the energy splitting variable z, both known from the Altarelli-Parisi approach. They control the kinematics of the parton branchings. The probability that a branching will take place during a small change dt is given by

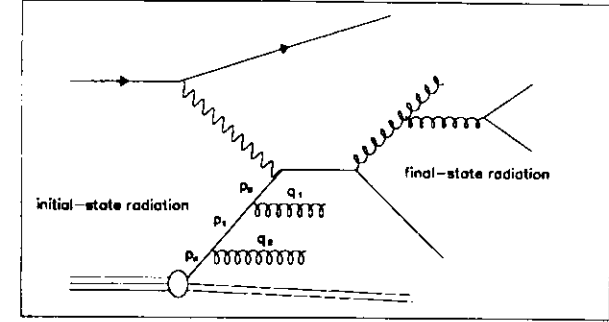$$\frac{dP_{a \to bc}}{dt} = \int dz \frac{\alpha_s}{2\pi} P_{a \to bc}(z) \qquad (4.1)$$

Figure 4.1: **Direct process with parton shower evolution**
Leading order QCD compton scattering with initial-state and final-state radiation.

with the corresponding splitting kernels of equation 2.40, 2.41, 2.42. The shower models differ mainly in the interpretation of t and z. The splitting variable z specifies the fraction of E, $E + p_z$ or $E + |p_z|$ of the mother parton which is given to the parton b. Furthermore z depends on the rest frame in which the parton energies are evaluated. In PYTHIA the preferred choice is the c.m. frame of the hard scattering. Also the choice of the evolution variable is not strictly prescribed by QCD. Conventionally it is defined by $t = \ln(Q^2/\Lambda^2)$, where Λ is the QCD scale in α_s. In PYTHIA the default choice of Q^2 is the off-shell mass of the partons with $Q^2 = m_a^2$, while the used scale in HERWIG is given by $Q^2 = m^2/(2z \cdot (1 - z))$.

Final-state showers

In a final state shower a parton cascade starts from a highly virtual parton whose virtualitiy is given by t_{max}. The produced partons generated in subsequent branching processes have a decreasing virtuality t. Since α_s depends on t, the cascade has to be stopped at a cut-off value t_{min}, where $\alpha_s(t_{min})$ becomes too large to justify the application of perturbative QCD.

$$Q^2_{max} = Q^2_{(1)} > Q^2_{(2)} > \ldots > Q^2_{(n)} = Q^2_{min}$$

The MC implementation of the parton shower evolution is based on the probabbility that a parton branching occurrs at a virtuality t. This probability can be calculated using the Sudakov form factor, which gives the probability that no branch occurs

between t and t_o, where $t > t_o$. The Sudakov form factor is given by

$$S_a(t) = \exp\left(-\int_{t_o}^{t} dt' \sum_{b,c} \int_{z_-(t')}^{z_+(t')} dz \frac{\alpha_s}{2\pi} P_{a \to bc}(z)\right) . \qquad (4.2)$$

The Sudakov form factor is nothing but the exponential decay law of radioactive decays with a Q^2-dependent decay probability. Since the integration of the Sudakov form factor is defined from a lower cut-off scale t_o to t, the required probability that no branch occurs between t_{max} and a smaller t is given by $S_a(t_{max})/S_a(t)$.

Initial-state showers

In contrast to the final-state shower with a forward evaluation in physical time, the partons of the initial-state showers are traced backwards from the hard interaction towards smaller virtualities. Since it is more convenient for the Monte Carlo implementation to define the hard scattering kinematics at first the technique of backward evolution of a parton shower is applied [52] using a modified Sudakov form factor. In the modified expression for the Sudakov form factors appear parton distributions, since the probability of a branching process $a \to bc$ with a parton a of the hadron is proportional to the parton density of parton a. The modified Sudakov form factor [53] gives the probability that a parton b remains at x during the backward evolution from t_{max} to $t < t_{max}$:

$$S_b(x, t_{max}, t) = \exp\left(-\int_{t}^{t_{max}} dt' \sum_{a,c} \int dz \frac{\alpha_s(t')}{2\pi} P_{a \to bc}(z) \frac{x' f_a(x', t')}{x f_b(x, t')}\right) . \qquad (4.3)$$

The range of the evolution variable

The range of t_{max} and t_{min} given by the corresponding Q^2_{max} and Q^2_{min} are free parameters in shower models. The cut-off parameter Q_{min}, which terminates the evolution is set to a low mass scale of $Q_{min} = 1.0\,\text{GeV}$. Partons with $Q^2 < Q^2_{min}$, below which partons are not allowed to radiate, are set on mass shell. The maximum value Q^2_{max} is usually associated with the hard scattering scale $\hat{Q}$. In general for most of the $2 \to 2$ processes the hard scale $\hat{Q}^2$ is given by p_t^2. In final-state showers the virtuality Q is associated with the mass of the branching parton and the transverse momenta generated in the branching processes are constrained by $p_t < Q/2$. In order to assign the highest p_t to the hard interaction in PYTHIA a decreasing ordering in p_t is constrained by the default choice of $Q^2_{max} = 4\hat{Q}^2$.

Coherence effects

Valuable inputs for parton shower methods are provided by theoretical studies of coherence effects, arising from the interference of soft-gluon amplitudes. These studies [52] have been shown that destructive interference [52] effects are large in the region of non-ordered emission angles. Coherence effects can be considered in parton shower programs by requiring a reduction of the phase space through a strict ordering of decreasing branching angles along the cascade from the hard vertex to the final partons. Decreasing parton masses do not constrain a decreasing order of emission angles, which is true only for the average of the angles, so that additional conditions have to be introduced to control the kinematics of parton branchings. Coherence effects lead to different ordering of emission angles for initial-state and final-state showers. These differences are described below in a discussion of the PYTHIA implementation of the final-state ordering and the HERWIG algorithm for the initial-state phase space reduction.

Angle ordering of final-state showers in PYTHIA

The implementation of angle-ordering in final-state showers is based on a comparison of each branching angle with that of the preceding branch. Consider the branching of the mother parton $a \to bc$ and the subsequent branchings of the daughter partons $b \to b_1 b_2$ and $c \to c_1 c_2$. The phase space reduction is obtained by requiring

$$\Phi_b < \Phi_a \qquad \text{and} \qquad \Phi_c < \Phi_a \qquad (4.4)$$

where Φ_a is the angle between the two outgoing daughters b and c of parton a, and Φ_b, Φ_c are the corresponding splitting angles of the subsequent branchings of the daughters b and c. The branching angle can be determined from the kinematic approximation:

$$\Phi_a \approx \frac{p_{t,b}}{E_b} + \frac{p_{t,c}}{E_c} \approx \sqrt{z_a(1-z_a)} m_a \left(\frac{1}{z_a E_b} + \frac{1}{(1-z_a)E_a}\right) = \frac{1}{\sqrt{z_a(1-z_a)}} \frac{m_a}{E_a} \qquad (4.5)$$

where m_a and E_a denote mass and energy of the mother parton a and z_a describes the energy fraction of the daughters, $E_b = z_a E_a$ and $E_c = (1-z_a)E_a$. Using this expression, the requirement $\Phi_a > \Phi_b$ is reduced to the kinematical condition:

$$\frac{z_b(1-z_b)}{m_b^2} > \frac{1-z_a}{z_a m_a^2} . \qquad (4.6)$$

Angle ordering of initial-state showers in HERWIG

Marchesini and Webber [55] developed a parton shower model, in which angle ordering is obtained by a modification of the evolution variable. Instead of the virtual mass, they introduced an angular type variable:

$$Q_i = E_i \sqrt{\xi_i} \quad , \quad \xi_i = \frac{p_n q_i}{E_n \omega_i} \tag{4.7}$$

where the notation of figure 4.1 is used and partons are denoted by their four-momenta. E_i and ω_i are the energy of the partons p_i and q_i, respectively. E_n, p_n denote energy and four-momentum of the incoming parton from the hadron side. In the small-angle region the ordering condition

$$Q_i < Q_{i-1} \tag{4.8}$$

leads to

$$E_i \Theta_{p_n q_i} < E_{i-1} \Theta_{p_n q_{i-1}} , \tag{4.9}$$

which is the correct phase-space reduction for initial-state showers. Compared with final-state showers, the relevant angles $\Theta_{p_n q_i}$ are the ones between the emitted partons q_i and the direction of the incoming p_n. The energy scaling of the angles only becomes important for very small x-values, otherwise all energies E_i are comparable. Thus, the main difference of initial- and final-state showers is found in the choice of the branching angles.

4.1.2 Fragmentation models

String fragmentation

The physical basis of the string fragmentation model is the concept of the linear confinement, best described for a back-to-back moving $q_o \bar{q}_o$-pair. The color field between the quarks is modelled by a uniform tube (string) with an energy proportional to their distance

$$E(r) = \kappa \cdot r \tag{4.10}$$

where κ is a string constant estimated to be $\kappa \approx 1.0\,\text{GeV}/\text{fm} \approx 0.2\,\text{GeV}^2$. As quark and antiquark move apart the field energy increases. At a typical distance of 2-5 fm the string breaks by forming of a new $q_1 \bar{q}_1$-pair, leaving two color singlets $q_o \bar{q}_1$, $\bar{q}_o q_1$. The successive processing of hadrons stops when only on-mass-shell hadrons remain.

Due to energy and momentum conservation, classical mechanics forbids point-like generation of particles with mass. Quantum mechanically the $q_1 \bar{q}_1$-pair is produced at one point and tunnels out to the allowed region, with a probability depending on mass and relative transverse momentum:

$$\exp\left(-\frac{\pi m_t^2}{\kappa}\right) = \exp\left(-\frac{\pi m^2}{\kappa}\right) \exp\left(-\frac{\pi p_t^2}{\kappa}\right) . \tag{4.11}$$

The transverse momentum of a meson is given by the vector sum of the transverse momenta of a quark and a antiquark which implies a width for mesons of approximately $\sigma_{\text{mes}} = 300\,\text{MeV}$. The mass term in the exponent suppresses heavy quarks with a rate of

$$u : d : s : c \quad = \quad 1 : 1 : \gamma_s : 10^{-11}$$

where the free parameter γ_s is introduced with a typical value of about $\gamma_s \approx 0.3$. The probability to produce a $q\bar{q}$-pair is described by the distribution $f(z)$, which is based on the energy E and longitudinal momentum p_z taken by a hadron out of the available energy $E + p_z$.

$$z = \frac{(E + p_z)_{\text{had}}}{(E + p_z)_{\text{quark}}} . \tag{4.12}$$

Different ansätze of $f(z)$ were studied and the default option of PYTHIA is given by the symmetric Lund fragmentation function:

$$f(z) = \frac{(1 - z)^a}{z} \exp\left(-\frac{b\,m_t^2}{z}\right) . \tag{4.13}$$

The string picture of multiparton systems including gluons and the production of baryons by diquark-antidiquark pairs, becomes more complicated, but does not lead to more free parameters. The main parameters, which have to be tuned to fit experimental data, are σ_{mes}, γ_s, a and b.

Cluster fragmentation in HERWIG

The cluster fragmentation model of Marchesini and Webber [55] is used together with their parton shower model. At a first step in the fragmentation model, any gluon of the shower evolution is forced to split into a light $q\bar{q}$-pair, where flavours are chosen randomly. Preclusters, described by their mass and color content are produced by combining of quark-antiquark or diquark-antidiquark pairs. The later are necessary

for the baryon production, like in the Lund model. Heavy preclusters with a mass above the threshold M_{clust}^{max} are split by creating of new $q\bar{q}$-pairs. Then the final clusters, fragment isotropically in the cluster rest-frames into two primary hadrons, which are mostly unstable. Light clusters are allowed to decay into single hadrons to take into account measured rates of single particles. At the end, unstable hadrons decay into stable particles.

4.1.3   Intrinsic k_t Smearing

In order to describe high-energy proton interactions such as ep or $p\bar{p}$ scattering, it was found to be necessary to assign an additional transverse momentum k_t to partons, which is attributed to non-perturbative effects, multi gluon exchange inside the proton and the fermi motion of the confined partons. The width of the k_t distribution, which is assumed to be Gaussian, is tuned to data and is different for the two Monte Carlo programs discussed here. Taking the default Gaussian distributions, HERWIG simulates the k_t smearing by a harder distribution with $\sigma = 0.7$ GeV, while PYTHIA uses a smaller value of $\sigma = 0.44$ GeV.

4.1.4   MC Event Generation

Monte Carlo events were generated using the leading order GRV photon parametrization and the next-to-leading order MRSD- parton distributions for the proton, which reasonably describes H1 and ZEUS data of F_2^p. In order to take into account different parametrizations for photon and proton, a reweighting technique has been applied.

Monte Carlo generators are basically controlled by variables stored in common blocks, which are set by the user to specify detailed subprocesses, options and parameter values. For comparison with other studies the main steering variables of HERWIG and PYTHIA are given in the following tables 4.1 and 4.2.

Parameter	Description	Choice
PTMIN	$p_{t,min}$ of hard interaction	2.5 GeV
Q2MAX	Q^2_{max} of ep-scattering	4.0 GeV^2
QCDLAM	hard interaction scale	$\hat{Q}^2 = 2\hat{s}\hat{t}\hat{u}/(\hat{s}^2\hat{t}^2\hat{u}^2)$
	choice of Λ_{QCD}-value	$\Lambda_{QCD} = 0.2$ GeV
IFLMAX	Number of flavours	$N_{max} = 5$
CLMAX	maximum mass of a cluster	$M_{max}^{clust} = 3.35$ GeV
PTRMS	σ of k_t^γ-distribution	0.70 GeV

Table 4.1: Common block variables of HERWIG

Parameter	Description	Choice
CKIN(3)	$p_{t,min}$ of hard interaction	2.5 GeV
PARP(13)	Q^2_{max} of ep-scattering	4.0 GeV^2
MSTP(32)	hard interaction scale	$\hat{Q}^2 = \frac{1}{2}(m_{t,3}^2 + m_{t,4})^2$
MSTP(2)	α_s	first-order α_s
MSTP(3)	choice of Λ_{QCD}-value	$\Lambda_{QCD} = 215$ GeV
MSTP(58)	Number of flavours	$N_{max} = 4$
MSTP(62)	strictly Q^2-ordering of showers	ON
PARJ(82)	cut-off m_{min} of parton showers	1.0 GeV
PARP(67)	Q^2_{max} of final-state shower	$Q^2_{max} = 4 \cdot \hat{Q}^2$
PARP(71)	Q^2_{max} of initial-state shower	$Q^2_{max} = 4 \cdot \hat{Q}^2$
MSTP(93)	primordial k_t^γ-distribution	Gaussian
PARP(99)	σ of k_t^γ-distribution	0.44 GeV
PARP(100)	$k_{t,max}$ of k_t^γ-distribution	2.0 GeV
PARJ(2)	s-quark suppression γ_s	$\gamma_s = 0.3$
PARJ(41)	a-value of the Lund function f(z)	$a = 0.5$
PARJ(42)	b-value of the Lund function f(z)	$b = 0.9$ GeV^2

Table 4.2: Common block variables of PYTHIA

4.2   Detector Simulation

A full description of the detector components is given in the Monte Carlo for Zeus Analysis, Reconstruction and Trigger (MOZART) program package, which makes use of the CERN GEANT3 [56] system. The GEANT3 program designed for the simulation of the detector response describes the passage of the generated particles through the various regions of the experimental setup taken into account geometrical volume boundaries and all physical interactions of the particles with the matter and the magnetic field of the detector. Detector components are represented by a structure of geometrical VOLUMEs, where each volume is defined by a set of material constants such as atomic weight, atomic number, density, radiation length and absorbtion length. These parameters are used to compute energy loss and cross sections. For hadronic particles the total cross section is computed from GHEISHA, a program for hadronic shower evolution contained in GEANT3.

After full simulation of the detector response the output from MOZART is fed into the ZGANA program for a simulation of the trigger logic, so that Monte Carlo events can be treated in the same way like data in the following analysis.

Chapter 5

Data Selection

This chapter gives a description of the data acquisition and the filter conditions, which are applied to select a hard photoproduction dijet sample. The three level trigger system, off-line data selection and the jet finder algorithm are discussed. Background studies will show that the strategy of data selection leads to a clean sample, with small contaminations from beam-gas interactions, cosmic muon events, deep inelastic scattering and a low contribution of diffractive hard photoproduction events.

5.1   Trigger

At HERA one of the challenges for the data acquisition is the bunch crossing time of 96 ns, clearly too short to perform a full data readout or to make a trigger decision. At design luminosity the ZEUS trigger system has to select interesting events with a rate of 3–5 Hz amongst background events of the order of about 100 KHz. Main types of background are proton beam-gas interactions, proton beam-halo interactions and cosmic muons. Background suppression is achieved by a three level trigger system, where each successive level has more time available to compute more complicated trigger decisions. Fig. 5.1 shows a schematic overview of the ZEUS trigger and data aquisition system. The *first level trigger* (FLT) operates only on a small subset of the detector data with reduced dynamic ranges to allow a first trigger decision after 4.6 μs, corresponding to 46 bunch crossings. At this level most of the beam-gas and beam-halo events can be eliminated and a trigger rate of 1 KHz is obtained. For the *second level trigger* (SLT) almost the whole fraction of the event data and the full dynamic range are used. The SLT-trigger decision is achieved at the latest 3 ms after the *ep*-interaction and reduces the rate to 100 Hz. The *third level trigger* (TLT) is based on the fully reconstructed event and performs background suppression down to a planned rate of 3–5 Hz.

For every bunch crossing the data of all detector components are stored in 10 MHz pipelines during the processing time of the FLT to achieve a deadtime-free data acquisition. Each component has its own pipelined readout electronics and a local first

level trigger. For the different components specific readout solutions were developed. While the readout electronics of all tracking components make use of digital pipelines, the UCAL readout is based on an analog CMOS pipeline realized in switched capacitor technology [57].

The FLT data from the detector components are sent to the global first level trigger (GFLT), where a final decision is generated from the logical-or of 64 subtriggers, which summarize the FLT information of all components. After a positive GFLT-decision the pipelined data are transferred to buffers for processing by the second level trigger. If the GFLT is not issued, the pipelined data are discarded.
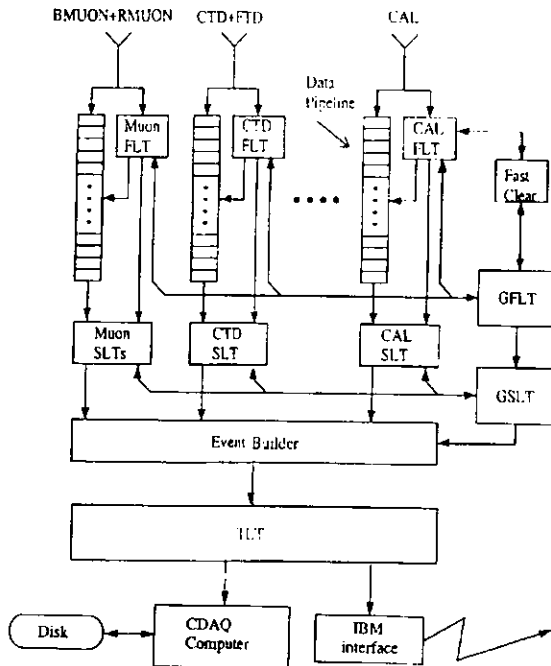

Figure 5.1: Schematics of the trigger and data acquisition system

Data from the local second level triggers are combined to carry out more accurate correlation checks concerning tracking, timing and vertex determination. Before the full event reconstruction is performed, the GSLT decides whether to accept or reject the event. In the case of a positive decision of GFLT and GSLT the data are sent to the event-builder (EVB).

The task of the event-builder is to collect and combine the data of all detector components in the final data format ADAMO and the transfer of the complete data structure to the third level trigger, where a full reconstruction of the event is performed. The typical size of one event is about 120 KBytes, depending on the event type.

The third level trigger must be able to achieve the reduction to the final rate of 3-5 Hz. The TLT can be used in offline and online mode. In the offline mode, the TLT runs the ZEUS Physics Reconstruction package ZEPHYR to reconstruct the event. Since, at this stage, the non-rejected background events passed the FLT and SLT, more sophisticated strategies have to be applied, which are based on event shape studies using energy flow properties of the reconstructed event. In online mode a reduced version of ZEPHYR takes time limitations of the third level trigger into account.

5.2 Hard Photoproduction Trigger

As mentioned, the decision of the GFLT depends on the logical-or of the used trigger configuration, which is set according to the trigger signature of the interesting event class. The 64 GFLT subtriggers combine the trigger information of the local detector components, expressed in terms of regional energy sums, tracking informations as well as the veto signal from the C5-counter. A definition of all subtriggers can be found in [58].

5.2.1 GFLT subtriggers for hard photoproduction

The signature of a typical hard photoproduction event are jets with large energy deposition in the uranium calorimeter. Therefore, this class of events are selected by using the calorimeter triggers. For FLT purposes, the calorimeter is segmented into 896 trigger towers, each tower consisting only of one EMC and one HAC section. Signals of trigger towers are used to compute the total calorimeter energy $Etot$, the transverse energy Et, the EMC energy of BCAL, RCAL and CAL denoted with $BEMC$, $REMC$ and EMC, respectively. In addition to the $REMC$ subtrigger, a second computation of the RCAL EMC energy with lower energy resolution including all trigger towers is given in the $REMCth$ subtrigger.

The computation of $Etot$ and EMC is carried out without use of the first three rings of FCAL towers and the first ring of RCAL towers around the beam pipe, where the exclusion of the very forward region reduces the sensitivity to energy deposition of the proton remnant and activity due to proton beam-gas interactions. Et is determined without the FCAL towers immediately adjacent to to the forward beam pipe, the so-called beam pipe ring, and the computation of $REMC$ excludes the beam pipe ring of the RCAL.

Subtrigger	Threshold Values	Res. Efficiency	Dir. Efficiency
Etot	10.0 GeV	54.9 %	54.4 %
Et	8.0 GeV	33.7 %	38.0 %
EMC	7.5 GeV	57.6 %	56.4 %
BEMC	2.0 GeV	56.0 %	63.8 %
REMC	2.0 GeV	37.0 %	32.2 %
REMCth	3.75 GeV	14.8 %	21.0 %
GFLT		87.6 %	89.9 %

Table 5.1: **Efficiencies of the GFLT subtriggers**
The table shows the threshold values of the used GFLT subtriggers and the trigger efficiencies for resolved and direct dijet events, generated with PYTHIA 5.6.

The threshold values of the subtriggers are shown in table 5.1. A given event is accepted, if the logical-or of the subtriggers is not vetoed by a signal from the C5-counter.

Efficiency of the GFLT

The trigger efficiency, defined by the ratio of accepted events to generated events is obtained from PYTHIA 5.6 Monte Carlo samples of dijet events for resolved and direct processes. Table 5.1 shows that the efficiency of single subtriggers does not exceed values of 60 %, whereas the high efficiency of 88 % for resolved and 90 % for direct events of the full GFLT trigger configuration demonstrates the requirement of a logical-or combination of several subtriggers.

The efficiencies depend on the definition of the generated dijet events, which in turn requires a definition of a *generated jet*. Since jets are defined by certain jet algorithms, the exact definition of a generated dijet event is presented after the discussion of the jet finder algorithm, where also the kinematic region as determined by the transverse jet energy, the maximum virtuality of the photon Q^2_{max}, and the y range is given.

5.2.2 The Second Level Trigger

During the '93 run period, the second level trigger was used to eliminate beam-gas and the so-called spark induced events, without any loss of physics events. Spark events are triggered by a high signal of a photomultiplier tube on the BCAL, while the energy deposition of the rest of the calorimeter is very small. The occurrence of sparking [59] is caused by leakage currents in the cathode region of the PMTs. Due to lower threshold, spark induced events are triggered mainly by the EMC region of the BCAL.

The SLT identifies sparks by requiring a single PMT signal of an EMC cell in

BCAL with an energy above 800 MeV, and energy sums of the remaining cells below 800 MeV in BCAL, 800 MeV in FCAL and 400 MeV in RCAL.

Rejection of proton beam-gas interactions uses the excellent time resolution of the uranium calorimeter of about 1 ns. It is possible to reconstruct arrival times of hadrons in RCAL and FCAL from the unweighted mean over all PMTs. Per definition, the mean FCAL time (t_{FCAL}) and the mean RCAL time (t_{RCAL}) are 0 ns for particles coming from the nominal interaction point. In the case of proton beam-gas interactions, with a vertex located upstream of the calorimeter, the produced particles arrive at the RCAL 11 ns before they hit the FCAL. This leads to a reconstructed time of $t_{FCAL} \approx 0$ ns and $t_{RCAL} \approx -11$ ns. The time reconstruction is carried out, if more than two photomultiplier tubes have an energy deposition in RCAL and FCAL. Events are accepted if no time could be determined or if the following timing cuts are satisfied:

$$|t_{FCAL}| < 8\,\text{ns} \quad \text{and} \quad |t_{RCAL}| < 8\,\text{ns}.$$

The influence of the SLT on the dijet photoproduction acceptance is negligible.

5.2.3 The Third Level Trigger

At the TLT level, the full event data are available and more complicated rejection algorithms can be applied to suppress background. Beam-gas rejection is improved by tighter timing cuts, while muon and spark suppression can be performed by algorithms, especially developed for muon and spark identification. The hard photoproduction group organized its data acquisition without direct muon and spark finding on the TLT level, since the applied energy cuts lead to a sufficient rejection.

TLT-Selection

Beside background reduction the TLT provides the possibility to apply filter sets adopted to the signature of the interesting event classes. For the hard photoproduction branch, the events are required to pass the following set of cuts:

- $E - P_z > 8$ GeV,
- $E_{t,cone} > 12$ GeV,
- $P_z/E < 0.94$,
- vertex with $|z| < 75$ cm,

where E is the energy measured by the calorimeter including all cells and P_z is the longitudinal energy given by the total sum over all calorimeter cells, $\sum(E_{cell} \cdot \cos\Theta_{cell})$. Angles, which depend on the interaction point, such as Θ_{cell}, are calculated with respect to the reconstructed vertex position. $E_{t,cone}$ is the total transverse energy where cells within a cone of $10°$ around the forward direction are removed.

Estimation of the total trigger efficiency

GFLT, SLT and TLT have a high acceptance for dijet events from photoproduction processes. The efficiency of the full trigger chain is 80.9 % (71.4 %) for resolved (direct) events. Fig. 5.2 shows distributions of $\log(x_p)$, x_γ and y separately for resolved and direct dijet events. Superimposed are histograms of events which pass the GFLT and TLT. As can be seen, both triggers affect mainly the low y-region, while the high y-region is only slightly reduced. In the high y-region, almost all events of the GFLT output are accepted by the TLT. In contrast to the high-y behaviour, in the
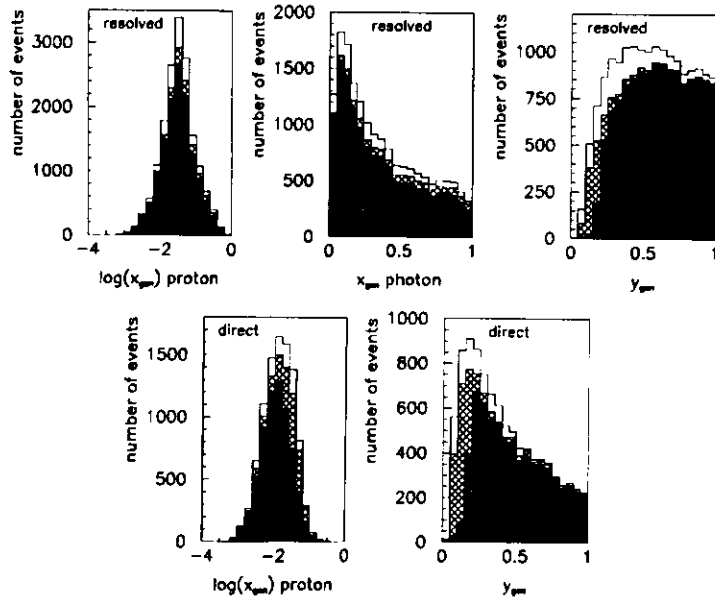

Figure 5.2: Trigger suppression of dijet events
The plots show $\log(x_p^{gen})$, x_γ^{gen} and y_{gen} histograms for hard photoproduction dijet events generated with PYTHIA 5.6. Superimposed are subsamples, which passed the GFLT (crossed) and the TLT (dark) decision. The first three plots depict histograms for resolved photoproduction events, while the fourth and fifth plot show the $\log(x_p^{gen})$ and y_{gen} histograms of direct photoproduction events.

low-y range the trigger efficiency of the GFLT is further reduced by the TLT. Both triggers favour more energetic γp-collisions and events with $y < 0.1$ do not pass the trigger chain.

The different y-shapes for resolved and direct events are explained by the lower momentum transfer to the hard interaction in resolved processes. Lower x_γ-values, $x_\gamma^{res} < x_\gamma^{dir} = 1$, of resolved events, are compensated by larger y-values to provide enough energy in the hard scattering center of mass system to form two jets. The different y-shapes are also the reason for the lower TLT trigger efficiency of direct events. Low-y events are very sensitive to the applied $E_{t,cone}$ cut of the TLT. Since the low-y region is strongly populated in direct processes, this cut leads to a lower TLT efficiency for direct processes than for resolved interactions.

5.3   Offline Data Selection

For the accepted events a full event reconstruction is performed with the reconstruction program ZEPHYR. First data from individual detector components like tracking chambers, the uranium calorimeter and the luminosity monitor are reconstructed, then the global track matching and matching of calorimeter cells and CTD tracks are performed and finally particle identification from combined data of CTD, CAL, HES and other components is performed. Results are stored in ADAMO tables, which allow an easy access by simple FORTRAN calls. A detailed introduction to the event reconstruction and analysis is given in [60].

DST Selection

Using the full information of the event after reconstruction, additional cuts can be applied to improve data selection. The results of the different offline filters are used to set so-called Data Selection Tape (DST) bits, which allow an assignment of the events to specific event classes. In this work, the data sample selected by the hard photoproduction working group high E_t filter (DST bit 28) is used. For this class, the events are required to fulfill the conditions:

- no signal from the Veto Wall counters,

- $|t_{FCAL}|$, $|t_{RCAL}|$, $|t_{FCAL} - t_{RCAL}| < 6$ ns,

- vertex with satisfying $|14 t_{FCAL} [ns] + z [cm]| < 60$ cm.

From the total integrated luminosity of 545 nb^{-1} taken by ZEUS in 1993 the complete trigger chain and DST offline selection accepted a sample of 146,141 events.

Final Off-Line Filter

Since the DST sample still contains background events, further cuts have to be applied to obtain a clean dijet sample with a background contribution below a few percent. Main sources of background are proton beam-gas events, cosmic ray events and ep-interactions of neutral DIS events. The aim is a suppression of each background source to a level below 1 %. A filter consisting of four steps is applied in the following order:

FIL1 Rejection of events with an identified electron with $y_e = 1 - \frac{E_e'}{2E_e}(1 - \cos\Theta_e) < 0.7$ found by the electron finder ELEC5, reduces the sample from $146,111$ to $121,976$ events.

FIL2 A cut on $y_{JB} > 0.15$ was used to select the kinematic range of the sample, while the restriction to $y_{JB} < 0.7$ was applied to reject the kinematic region where the outgoing electrons of DIS events cannot be separated sufficiently from secondary electrons and photons. These cuts lead to a sample of $108,891$ events.

FIL3 An enlarged threshold value of $E_{t,cone} = 15\,\text{GeV}$ reduces the sample to $73,306$ events.

FIL4 A track finding algorithm based on the VCTRK package [61] is used to reconstruct tracks not associated with the vertex. To reduce beam gas events, events with more than five such tracks are rejected, leaving $69,152$ events.

5.4   Jet finding

On the data sample remaining after trigger, DST and off-line selection a jet finding algorithm is performed to search for events with two or more jets to obtain the final data sample. In order to reduce uncertainties in the comparison of jet cross section measurements, a standard jet definition adopted for QCD measurements was proposed at the Snowmass conference [62] in 1990. The jet definition is based on clustering of calorimeter cells in a metric of pseudo rapidity η and azimuth ϕ. Clusters are defined by all calorimeter cells which fulfill

$$R_{cell} = \sqrt{(\phi_{cell} - \phi_{clu})^2 + (\eta_{cell} - \eta_{clu})^2} < R_{cone}$$

where ϕ_{clu} and η_{clu} represent the center of the cluster and ϕ_{cell} and η_{cell} are the coordinates of the calorimeter cells, which are determined by the jet finding procedure. In practice, an iterative approach in forming jet centroids is applied. Different cone algorithms differ mainly in the used procedure to define the cone axis. In this work, the cone algorithm PUCELL is used. Cluster quantities, such as the transverse energy

and the coordinates of the cluster axis, are derived from the energies of the assigned cells. The transverse energy of a cluster is defined by:

$$E_{t,clu} = \sum_{cell} E_{t,cell}$$

where the sum runs over all cells inside the cone radius. Using $E_{t,clu}$, the centroid of the cluster is identified with the E_t weighted sums:

$$\eta_{clu} = \frac{1}{E_{t,clu}} \sum_{cell} E_{t,cell} \cdot \eta_{cell} \tag{5.1}$$

$$\phi_{clu} = \frac{1}{E_{t,clu}} \sum_{cell} E_{t,cell} \cdot \phi_{cell} . \tag{5.2}$$

The PUCELL algorithm

The following five steps describe the implementation of the Snowmass convention by the cone algorithm PUCELL with used threshold energies and steering parameters.

1. Cells are ordered in decreasing transverse energy $E_{t,cell}$. Cells above a threshold energy of $E_{t,seed} > 300\,\text{MeV}$ serve as seed cells to initiate the clustering.

2. For each seed cell, cells within a cone radius of $R_{pre} = \sqrt{(\Delta\eta_s)^2 + (\Delta\phi_s)^2} = 1.0$ of each other are grouped into preclusters, where $\Delta\eta_s$ and $\Delta\phi_s$ are the distances in η and ϕ between seed cell and precluster cell.

3. The centroid of each precluster is determined using the E_t weighted η and ϕ centres of the assigned cells, according to Eqn (5.1), (5.2).

4. Using the centroids of the preclusters, clusters are reconstructed performing a loop over all cells with $E_{cell} > 80\,\text{MeV}$ and $E_{cell} > 30\,\text{MeV}$ for HAC and EMC cells, respectively, if they are within a distance of $R_{cone} = 1$, where the same cone radius is taken for clusters and preclusters. The centroids of the clusters are recalculated with the new cells assigned to the cluster. Using the new centroid of the cluster, this procedure is repeated until the cell-cluster assignment is stable. If stability is not reached, the procedure stops after 20 iterations.

5. A merging routine is applied to handle cells, which are assigned to more than one cluster. The energy sum of cells, which are assigned to two clusters, the so-called overlap energy, is calculated. If the overlap energy exceeds 75 % of the energy of the smaller cluster, the two clusters are merged, otherwise these cells are assigned to the closest cluster. The centroids of the final clusters are

recalculated, and if the transverse energy of a cluster is above a threshold of 5 GeV, it is considered as a jet.

From the sample, which passed trigger, DST and off-line selection a subsample of 11,654 dijet events is selected with at least two reconstructed detector jets in the range $-1 < \eta < 2$, and a transverse jet momentum of $E_{t,jet} > 5.0$ GeV.

Generated Dijet Events

The cone algorithm PUCELL is used to reconstruct jets, from the energy depositions in the CAL cells for both data and generated MC events. They are called detector jets and will be denoted by an index 'det'. In order to assess the quality of the reconstruction of jets, the detector jets have to be compared with the generated jets. In contrast to the partons, which are well defined within the MC programs, the generated jets consist of the outgoing hadrons and depend on the jet definition and the free parameters of the jet finding algorithm, such as the cone radius. The generated jets, the so-called hadron jets, can be defined by a hadron jet finder, similar to the PUCELL algorithm, where calorimeter cells are replaced by the outgoing hadrons. All final state particles in the angular range $5° \leq \Theta \leq 175°$ are considered for the hadronic jet search. Cone radius and merging routine are the same as in the PUCELL jet finder. Variables associated with hadron jets are denoted by 'had'.

Using hadron jets, it is possible to give a precise definition of generated hard photoproduction dijet events for the analysis presented. Generated dijet events are defined by the following conditions:

- $0.2 < y_{gen} < 0.8$,

- maximum virtuality $Q^2_{max} = 4$ GeV^2,

- transverse jet energy $E^{had}_{t,jet} > 6$ GeV,

- at least two reconstructed hadron jets

- in the rapidity range $-1 < \eta^{had}_{jet} < 2$.

For three and four hadron jet events, which contribute with 7.2 % and 0.3 % to the final MC sample, only the two jets with the highest transverse jet energy are considered in the following analysis. The jet multiplicities are estimated using the GRV-LO and MRSD- parton parametrizations for the resolved photon and the proton, respectively. Direct and resolved processes are mixed according to their cross sections given by the PYTHIA generator.

Measured Dijet Events

The goal of this work is the measurement of the differential rapidity jet cross section $(d\sigma/d\eta_{had})_{\eta_1,\eta_2}$, with two entries per event using the two jets with the highest transverse jet momentum. The definition of a generated dijet event and the considered kinematic region is given by the conditions of the previous paragraph.

In contrast to the generated dijet events the experimentally observed dijet events are defined by the complete trigger, DST and off-line data selection. In order to allow a convenient comparison between generated and measured detector events, the following summary presents the main condition which are passed by dijet events on the detector level:

- GFLT, SLT and TLT decision,

- DST off-line selection,

- $0.15 < y_{JB} < 0.7$,

- maximum virtuality $Q^2_{max} = 4$ GeV^2, i.e. no identified electron with $y_e < 0.7$ in the calorimeter,

- transverse jet energy $E^{det}_{t,jet} > 5$ GeV,

- at least two reconstructed detector jets, where the two jets with the highest transverse jet energy are accepted for the analysis,

- both jets are in the rapidity range $-1 < \eta^{det}_{jet} < 2$.

Comparing the generated with the detector events, it is seen, that both classes of events differ in the minimum transverse jet energy and in the y range. The lower transverse jet energy and the reduced y_{JB} range take into account smearing effects caused by the imperfection of the detector measurement. A discussion of detector effects concerning the choice of the y_{JB} range and the minimum transverse jet energy is given in the next chapter.

Typical signatures of two measured hard photoproduction dijet events are shown in Fig. 5.3. For each event a vertical cut of the calorimeter along the beam, a cross section of the calorimeter perpendicular to the beam and an η-ϕ lego plot of the transverse energy of the calorimeter cells are presented. The upper figure depicts a resolved dijet event with an additional photon remnant jet close to the beam pipe in the RCAL. The lower figure shows a direct dijet event with two jets in the BCAL and no activity in the backward region.
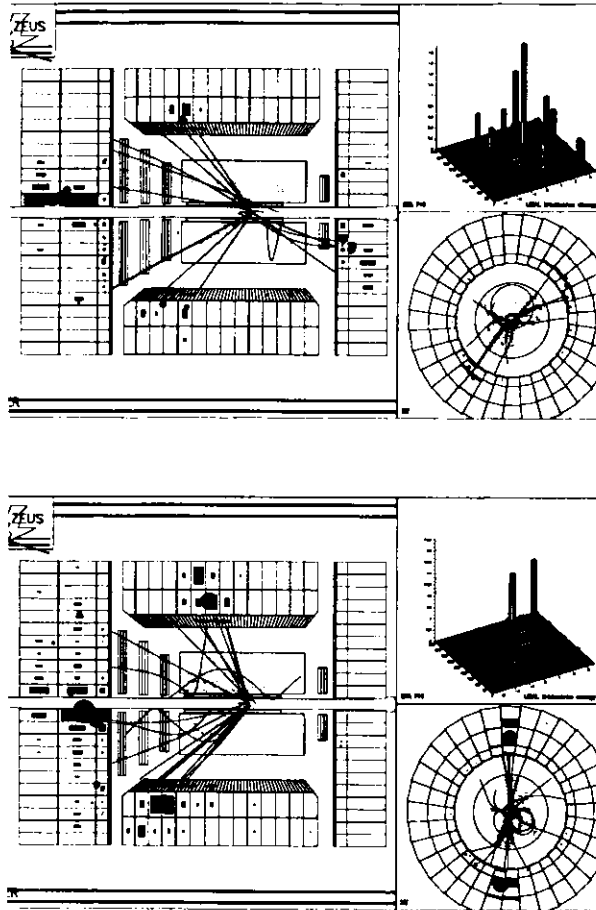
Figure 5.3: Resolved and direct photoproduction dijet events
Typical detector signatures of a resolved and a direct photoproduction event are shown for a vertical cut and a cross section of the calorimeter. The transverse energy of the calorimeter cells is presented in an η-ϕ lego plot. The upper figure depicts the resolved dijet event with a photon remnant jet close to the beam pipe in the RCAL. The lower figure shows the direct dijet event with two jets in the BCAL.

5.5 Background Estimates

Background studies of non ep events use data from the pilot bunches. The number of events, which are assigned to electron pilot bunches, proton pilot bunches and colliding bunches allow to estimate the contribution of electron and proton beam-gas and cosmic muon induced events. Since a fraction of the pilot bunch events is produced by cosmic muons, the pilot bunches can only be used to estimate the combined background of beam-gas and cosmic muon events. In addition to the pilot bunches, there exist also crossings with empty bunches, where the only contribution is given by cosmic muons. The empty bunches can be used to estimate approximately the efficiency of a cosmic muon filter.

The contamination by electron pilot or proton pilot bunches is obtained from the number of events assigned to the considered pilot bunches n_{pilot}, the total number of events n_{ep} excluding the pilot bunches, and the ratio of the integrated proton (electron) current $\mathcal{I}_{\text{pilot}}^{\text{P}}$ ($\mathcal{I}_{\text{pilot}}^{\text{e}}$) of the proton (electron) pilot bunches to the integrated proton (electron) current $\mathcal{I}_{ep}^{\text{e}}$ ($\mathcal{I}_{ep}^{\text{P}}$) assigned to the ep bunch crossings. For instance, the percentage of the background B_{pilot} due to the proton pilot bunches is then given by

$$B_{\text{pilot}} = \frac{n_{\text{pilot}}}{n_{ep}} \cdot \frac{\mathcal{I}_{ep}^{\text{P}}}{\mathcal{I}_{\text{pilot}}^{\text{P}}} \ .$$
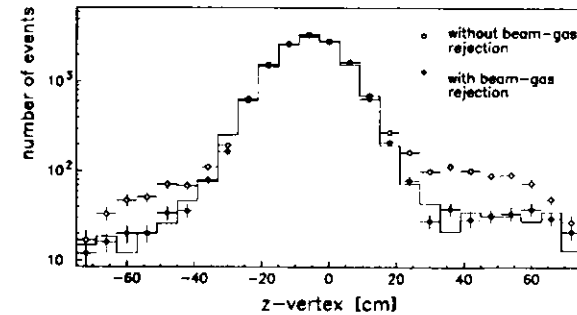

Figure 5.4: Vertex distributions of data and Monte Carlo
The figure shows the vertex distributions of data (dots) and PYTHIA (full line) events with two or more jets on detector level. All events have passed trigger, DST and final off-line filter chain, apart from the beam-gas filter FIL4. Open circles show data without the off-line filter FIL4 and full dots represent the improved data sample with filter FIL4.

Beam-gas background

Most of the beam-gas background is rejected by the timing cuts in the TLT or DST
filter. A further improvement of proton beam-gas rejection is achieved by the proton
beam-gas filter FIL4. Fig. 5.4 shows the vertex distributions of the final dijet sample
without filter step FIL4, open dots, and with FIL4 selection, black dots, while the
full line shows the beam-gas free Monte Carlo distribution.

The proton beam-gas filter is based on the typical event signature with a large
number of tracks in the CTD, as shown in the upper plot of Fig. 5.5. Using this specific
behaviour, the VCTRK track finding algorithm is used to identify so-called long tracks
where the closest approach z_{tr} of the trajectories to the beam line ($x = y = 0$) has
at least a distance of 20 cm from the reconstructed vertex z, z $z_{tr} > 20$ cm. More
precisely, long tracks are defined as tracks which traverse the innermost superlayer
and one of the superlayers three to eight and points to an energy deposition in the
calorimeter. Events with more than five long tracks are rejected.

Without use of the off-line filter FIL4, the background estimated from the proton
pilot bunches amounts to 5.1 %, which is reduced to 1.1 % when using the proton
beam-gas filter. The contamination due to electron pilot bunches, which is not af-
fected by the off-line filter FIL4, is 0.5 %.

Cosmic muon background

Since no muon finder has been applied in the data selection chain, it is expected that
an essential contribution of the remaining background are cosmic muon events. The
signature of a typical event given by the second plot of Fig. 5.5, suggests that these
events can be identified by the most forward condensate, measured in the uranium
calorimeter, where a condensate is defined as an isolated set of adjacent cells with
an energy sum above 400 MeV. The rapidity of a condensate is calculated from the
angle of the energy weighted centre with respect to the vertex.

In the case of a cosmic ray event, the energy deposition of the muon in the
calorimeter gives rise to the reconstruction of two jets, back-to-back in the (η, ϕ)-
plane, i.e. $\eta_{jet1} \approx -\eta_{jet2}$ and a difference of the azimuth angles of $\Delta\phi \approx 180°$.
From Fig. 5.5, one can expect that for cosmic muons with roughly vertical tracks
the maximum rapidity of the condensates will be greater than $\eta = 0.0$ and smaller
than approximately $\eta \approx 1.5$. Fig. 5.6 (a) presents the η_{max}^{con}-distribution of data and
PYTHIA dijet events. The data distribution shows a clear shoulder in the low η_{max}^{con}-
range, which is typical for distributions of *large rapidity gap* events and cosmic muon
induced events. The scatter plot of the two jet rapidities, as shown in Fig. 5.6 (b)
demonstrates that more than 50 % of the events are concentrated around the line
defined by $\eta_{jet1} = -\eta_{jet2}$, where the cosmic muon induced events are expected. In
order to reduce the background of cosmic muons, an off-line filter FIL5, which leads
also to rejection of the *large rapidity gap* events, is applied after jet-finding.

FIL5 Events with $\eta_{max}^{con} < 1.5$ are rejected.
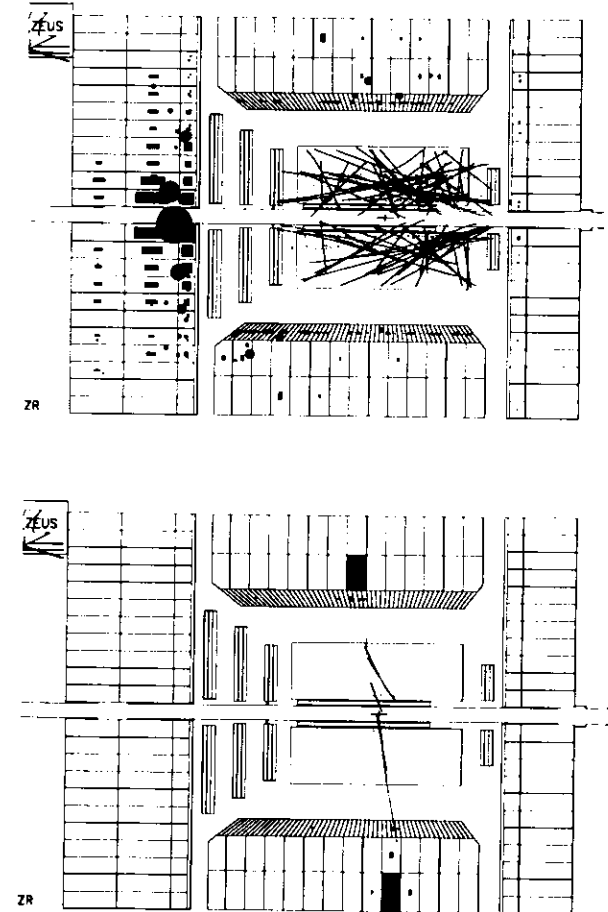
Figure 5.5: Beam-gas and cosmic ray muon event
Typical detector signatures of the calorimeter and inner tracking chambers are shown for
two classes of background events. The upper figure depicts a proton beam-gas event with
a large number of reconstructed tracks in the CTD, while the lower figure shows a cosmic
ray muon, with almost no activity in the CTD and no energy deposition in the forward
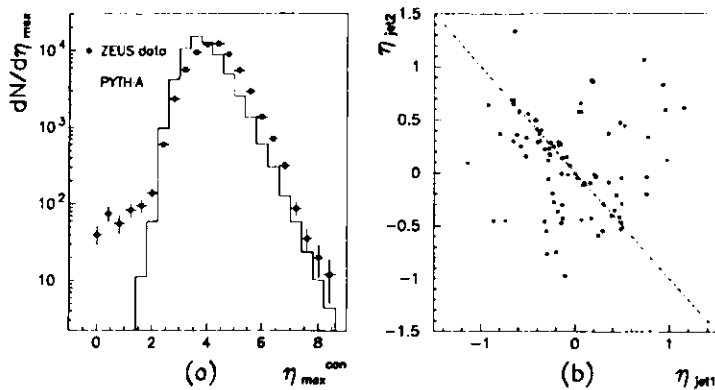and backward calorimeters.

Figure 5.6: η_{max}^{con}-distributions of condensates

In Fig. (a), distributions of the maximum rapidity of calorimeter condensates are shown for data (dots) and PYTHIA (full line) dijet events after trigger, DST and off-line selection without use of the FIL5 filter step. Fig. (b) is a scatter plot of the two jet rapidities for dijet events with a maximum rapidity of condensates $\eta_{max}^{con} < 1.5$.

This rather simple method for cosmic muon rejection is justified by the reduction of the cosmic muon contribution included in the electron and proton pilot bunches. Using the off-line filter FIL5 the background contributions assigned to electron and proton pilot bunches are reduced from 0.5 % and 1.1 % to 0.2 % and 0.6 %, respectively.

The efficiency of FIL5 is illustrated by the suppression of events from empty bunches, which are produced by cosmic muons. From 19 events triggered by empty bunches, the off-line filter FIL5 leads to a rejection of 17 events.

The main reason for the low contamination due to cosmic muon events is the dijet condition, which requires at least two jets with a transverse jet energy of 5 GeV for each jet. Cosmic muon events, which pass this condition can then be rejected by the simple cut FIL5.

Contribution of diffractive hard photoproduction events

In recent publications, evidence has been presented for events with a *large rapidity gap* in deep inelastic scattering [63] and in hard photoproduction [64]. These events are characterized by the presence of a large rapidity gap towards the proton direction

in the η_{max}^{con} distribution. The event characteristics are consistent with a diffractive process, in which a colorless object, the so-called pomeron, is exchanged between photon and proton. Ingelman and Schlein [65] assumed a model, in which the pomeron behaves like a hadron with a partonic substructure.

To determine the contribution of diffractive hard events present in the dijet sample, diffractive events were generated with POMPYT, which is a Monte Carlo model within the framework provided by PYTHIA. For the partonic substructure, the *gluonic* pomeron with a hard parton distribution $xg(x) = 6x(1 - x)$ was chosen. The assumption of a pure gluonic structure can be used to estimate approximately the upper limit of the contribution of large rapidity gap events. Parton distribution of soft gluons, $xg(x) = 6(1 - x)^5$, or a pomeron structure with a pure quark distribution, $xq(x) = \frac{6}{4}x(1 - x)$, result in clear smaller jet cross sections, as shown in recent results [66] concerning the measurement of the pomeron structure in hard photoproduction.

For the photon direct and resolved contributions are considered. The resolved photon is parameterized using the DG (Drees and Grassie [20]) parton distributions. After application of the full trigger, DST and off-line filter including the filter FIL5, a contamination of hard diffractive events below 3.7 % is expected using the diffractive sample generated by POMPYT.

Contamination from deep inelastic scattering

The last source of background are deep inelastic scattering events. Almost all events of this class pass the GFLT, where calorimeter triggers are used to signal jet activity, and the third level trigger is also not adopted to reduce DIS events. A sufficient DIS suppression is based on an electron finder algorithm. In FIL1 ELEC5 is used to identify electrons in the range $y_e < 0.7$, where y is calculated from the energy and scattering angle of the electron. For higher y-values, the separation of the scattered electron from secondary electrons and photons becomes insufficient. This region is rejected by a cut $y_{JB} < 0.7$ in the off-line filter FIL2. For background studies, DIS events are produced with HERACLES using the structure function MRSD-' for the proton.

After the DST selection, DIS events contribute with 5.2 % to the hard photoproduction sample. The electron finder applied in FIL1 reduces this contribution to 1.0 % and after the y_{JB}-cut in FIL2 and jet finding a contamination of 0.3 % is achieved.

In summary, a clean hard photoproduction dijet sample is selected with a total background contamination of about 1.1 %, produced by beam-gas interactions, cosmic ray muon induced events and deep inelastic scattering. The contribution of hard diffractive events is below 3.7 %.

Chapter 6

Data Sample

This chapter begins with a discussion of the general characteristics of the measured dijet events and their simulation by the Monte Carlo program PYTHIA 5.6. It has been checked, how the variables in the analysis are modelled on generator level and in the following detector simulation. Several distributions for data and MC are compared. The analysis depends strongly on the correct simulation of the calorimeter response and the material in front of it.

Differences between data and MC distributions can be caused by an inadequate detector simulation or by physical processes not properly included in the event generation. Therefore, in case of discrepancies further checks are required to analyse their origin. Energy loss and shower processes due to inactive material, as well as the shower evolution in the calorimeter lead to resolution and acceptance effects. They are studied by correlation plots, where the differences between generated values and their reconstructed values are measured to asses the quality of the reconstructed variables based on the uranium calorimeter.

6.1   General Event Characteristics

The distribution of several quantities describing general characteristics of the event are shown for data and for a sample of PYTHIA in Fig. 6.1. The MC sample includes direct and resolved processes using the GRV-LO (full line) and LAC1 (dashed line) photon parametrization, where resolved and direct contributions are mixed according to their cross sections as given by PYTHIA 5.6. The figure presents histograms of the total energy E_{tot}, the transverse energy E_t, energy deposits of the calorimeter sections FCAL, BCAL and RCAL denoted with E_{FCAL}, E_{BCAL} and E_{RCAL}, respectively, and of y_{JB}. All histograms are normalized to one.

The shape of the y_{JB}-distribution is well described by the GRV parametrization, while the expectation from LAC1 is systematically below the data at low values. This is in agreement with the assumption, that due to the higher cross section of the LAC1 parametrization, the direct component which dominates at low y-values, becomes less
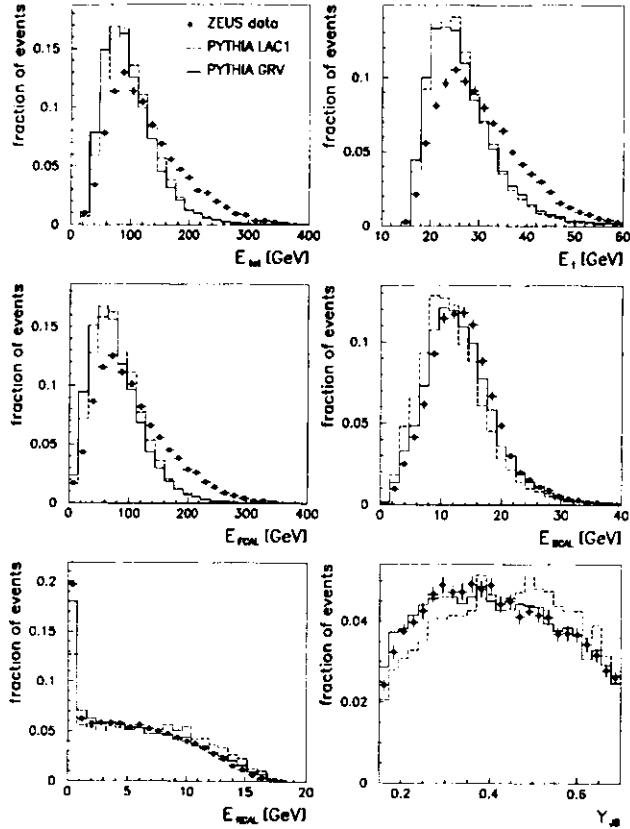
Figure 6.1: General event characteristics
The figures show histograms (normalized to one) of the total energy E_{tot}, the transverse energy E_t, the energy of FCAL, BCAL and RCAL denoted as E_{FCAL}, E_{BCAL} and E_{RCAL}, respectively, and the distribution of y_{JB} for data (dots) and PYTHIA 5.6. The MC sample includes direct and resolved processes, for the GRV-LO (full line) and LAC1 (dashed line) photon parametrization, where resolved and direct contributions are mixed according to their cross sections given by PYTHIA.
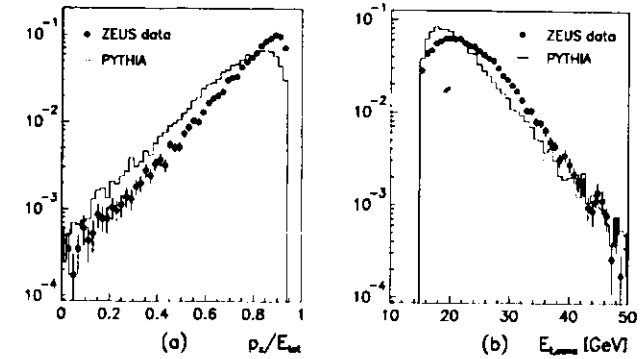

Figure 6.2: Distributions of trigger variables
Distributions of p_z/E_{tot} and $E_{t,cone}$ are shown for data (dots) and PYTHIA using the GRV (full line) photon parametrization. Histograms are normalized to one.

relevant.

While E_{BCAL} and E_{RCAL} distributions are reproduced by PYTHIA, a strong excess of energy is observed in FCAL, affecting also the distributions of the total energy and transverse energy. Due to the remarkable discrepancy in the description of the forward energy, detailed investigations are necessary to study the origin and the influence of the energy excess on the calculation of the dijet cross section.

The observation of a forward energy excess should affect also the variables p_z/E_{tot} and $E_{t,cone}$, used in the TLT and off-line data selection. Their distributions are depicted in Fig. 6.2. Both variables show a systematic shift to higher values for the data, which is expected due to extra energy in the FCAL.

6.1.1   Jet characteristics

Quantities related to the reconstructed detector jets are given in Fig. 6.3. It is seen, that energy and transverse energy of the jets are in excellent agreement for data and MC sample. The difference $\Delta\phi$ of the azimuth angles between both jets is shown in a linear scale for $\Delta\phi > 120°$ and in a logarithmic scale for the full range. In leading-order QCD, without parton showering, the two jets balance in transverse energy, due to momentum conservation, with $\Delta\phi \approx 180°$. Due to parton showers and fragments from both the proton remnant and the photon remnant, pairs of jets with low $\Delta\phi$-values are reconstructed. For $\Delta\phi > 120°$ data are described well by PYTHIA, while
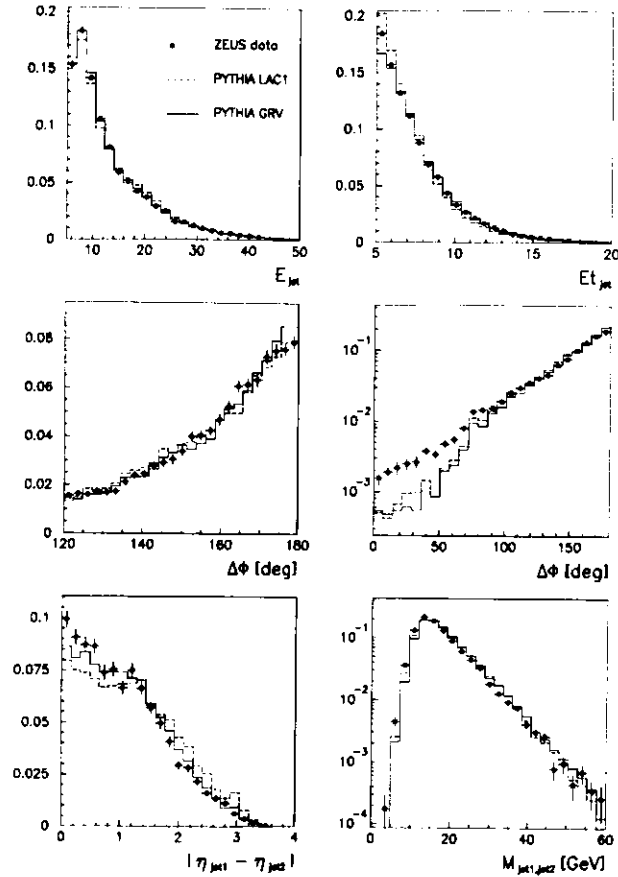
Figure 6.3: Characteristics of the dijet system
Data and PYTHIA distributions for the energy of the jets E_{jet}, transverse jet energy Et_{jet}, the difference of the azimuth angles $\Delta\phi$, the rapidity difference $|\eta_{jet1} - \eta_{jet2}|$ and the invariant mass $M_{jet1,jet2}$ of the dijet system. Histograms are normalized to one.

for $\Delta\phi < 120°$, as shown in the logarithmic plot, data are above the MC prediction, illustrating a small excess of events with unbalanced pairs of jets.

The last two plots of Fig. 6.3 show distributions of the difference of jet rapidities and the invariant mass $M_{jet1,jet2}$ of the dijet system. The histogram of $M_{jet1,jet2}$ is in good agreement within the systematic uncertainties due to the choice of the structure function. Note, that the invariant dijet mass is used in Equ. 2.85 to define x_γ, which demonstrates the intrinsic dependence on the parton parametrization of the photon.

The $|\eta_1 - \eta_2|$-shape shows a small deviation in the range of $|\eta_1 - \eta_2| < 0.5$, where the expectations of PYTHIA are slightly below the data.

Track multiplicity

The agreement of the E_{jet} and $E_{t,jet}$ distributions between data and MC sample suggests that the string fragmentation model of PYTHIA gives a good approximation of jet evolution in the present kinematic range. This is confirmed by measurements of jet profiles [67], showing that the energy flow inside the jet cone as a function of rapidity and azimuth angle is reproduced by PYTHIA. For the dijet sample, the track multiplicity of jets is measured, using long tracks as defined in the previous chapter, in the range $-1 < \eta_{jet} < 1$, where the CTD has high acceptance. Tracks inside the jet cone coming from the vertex are assigned to the jet and are used to reconstruct
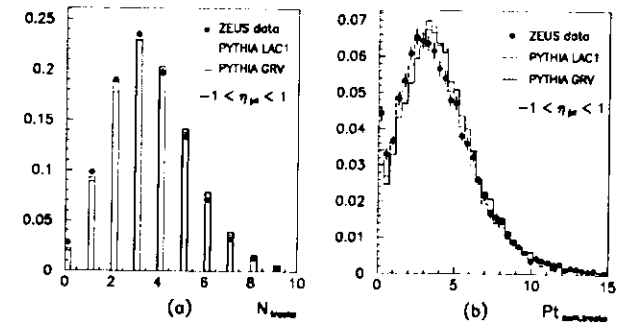

Figure 6.4: Multiplicity and transverse momentum sum of jet tracks
Fig. (a) shows the multiplicity of charged particles of all jets taken from the final dijet sample in the rapidity region $-1 < \eta_{jet} < 1$. Fig. (b) displays the sum of the transverse momenta $\sum |\vec{p}_{t,track}|$ carried by charged particles inside jets. Data (dots) are compared with PYTHIA samples including direct and resolved contributions; GRV-LO (full line) and LAC1 (dashed line). Histograms are normalized to one.

the transverse jet momentum $Pt_{sum,tracks}$ as measured by the CTD. Fig. 6.4 displays track multiplicity and transverse momentum $Pt_{sum,tracks} = \sum |\vec{p}_{t,track}|$ from the charged tracks. The track multiplicity is in good agreement with the PYTHIA prediction, while the maximum of the $Pt_{sum,tracks}$ distribution is slightly shifted peaking at 2.5 GeV as compared with 3.5 GeV for the Monte Carlo. Still, the string fragmentation used in PYTHIA is a remarkable description.

jet multiplicity	resolved	direct	resolved + direct	data
1-jet	$71.6 \pm 0.4\%$	$42.3 \pm 0.8\%$	$67.9 \pm 0.5\%$	$68.1 \pm 0.4\%$
2-jet	$26.1 \pm 0.3\%$	$52.3 \pm 0.9\%$	$29.4 \pm 0.4\%$	$28.7 \pm 0.3\%$
3-jet	$2.3 \pm 0.1\%$	$5.3 \pm 0.3\%$	$2.7 \pm 0.1\%$	$3.0 \pm 0.1\%$
4-jet	$0.11 \pm 0.02\%$	$0.15 \pm 0.05\%$	$0.12 \pm 0.02\%$	$0.24 \pm 0.03\%$

Table 6.1: Distribution of jet multiplicities for MC resolved, direct and for data samples. The combined sample of direct and resolved contributions is mixed according to the generated cross section of PYTHIA.

Jet multiplicity

In the previous comparison of jet quantities it has been demonstrated that jet characteristics sensitive to the fragmentation like jet energy E_{jet} and track multiplicity are in good agreement with expectations of PYTHIA. Variables related to the hard scattering process, such as $M_{jet1jet2}$ or the $\Delta\Phi$-distribution in the range $\Delta\Phi > 120°$ are also well reproduced by the MC simulation. A further quantity of the latter class is the distribution of jet multiplicities. Jet rates are presented in table 6.1. The rate of 1-jet, 2-jet, 3-jet and 4-jet events are given for data, resolved, direct and the mixed sample of resolved and direct events. The values are normalized to the number of events with at least one reconstructed jet. Resolved and direct samples differ significantly in the 1-jet and 2-jet rate. The origin of this difference is due to the higher energy parton momentum in the hard interaction for direct than for resolved events, expressed by $x_\gamma^{res} < x_\gamma^{dir} = 1$, which leads to more jets in the acceptance range of the detector. The complete sample of the mixed PYTHIA gives a good prediction of the rates for 1-jet and 2-jet events. The 3-jet rate is slightly higher for the data, while the 4-jet rate of data is larger by a factor of 2, than the prediction of PYTHIA. This could be a hint for higher order QCD effects not included in PYTHIA. But also multiple interactions should be able to account for higher rates of 3-jet and 4-jet events.

6.1.2 Event signatures of resolved and direct photoproduction

In this section, the comparison of data and Monte Carlo samples of PYTHIA is extended to variables, which provide more information about the underlying resolved

and direct processes. Variables describing the hard interaction are y_{JB}, η_{jet}, x_γ, x_p and energy deposition in the backward direction. Due to the occurrence of the photon remnant in the resolved process, large differences of the event topology are expected for resolved and direct events in the backward region.

Uncorrected differential cross sections $d\sigma/dx_\gamma^{det}$ **and** $d\sigma/d\log(x_p^{det})$

It has been shown, that the data and Monte Carlo distributions are in good agreement for quantities which do not depend strongly on the energy deposits in the forward region, where the data show a large excess of energy compared to the PYTHIA MC. In this section, one of the main distinction of resolved and direct process, the distribution of x_γ is shown.

The measurement of x_γ^{det} requires the reconstruction of two jets and the determination of y, which can be estimated by a measurement of y_{JB}. Since the y_{JB}-distribution and the jet energies are well reproduced by PYTHIA, a measurement of x_γ^{det} provides a first check of the jet rapidity distributions, see Equ. 2.78. A description of the differential cross section measurement is given in the next chapter.

Before cross sections of x_γ^{det} and x_p^{det} are presented, two different reconstruction methods are compared to check the conventional reconstruction method, where x_γ^{det} and x_p^{det} are calculated using Equ. 2.76 and Equ. 2.77 with y_{JB} as an estimate for the photon energy.

Fig. 6.5 shows scatter plots of x_γ^{det} versus $x_{\gamma,D}^{det}$ of the D'Agostini-Monaldi approach, as described in section 2.3 for data, resolved and direct MC events. The complete dijet sample and the subsample with $\Delta\phi > 150°$ are compared. While in the conventional method x_γ^{det} and x_p^{det} depend on the transverse momenta and rapidities of the two jets, in the D'Agostini-Monaldi method $x_{\gamma,D}^{det}$ is evaluated from the invariant masses of the dijet system and the system of the two jets plus the photon remnant. Both invariant masses depend on the difference of the azimuth angle of the dijet system. Deviations from $\Delta\phi = 180°$ lead to a decrease of the dijet mass and of the reconstructed value of $x_{\gamma,D}^{det}$. The tail of low values in the $\Delta\phi$-distribution causes the differences, which are observed in the plots of Fig. 6.5. For events with approximately back-to-back scattered jets ($\Delta\phi > 150°$), both reconstruction methods are in good agreement, so that in the following studies only the conventional reconstruction method is taken.

Fig. 6.6 depicts the uncorrected cross sections of detector jets $d\sigma/d\log(x_p)$ and $d\sigma/dx_\gamma$. Differential cross sections of data and a mixed sample of direct and resolved PYTHIA events are shown using the GRV-LO photon parametrization. The direct contribution, included in the PYTHIA sample, is drawn separately. While the shape of $d\sigma/d\log(x_p)$ is approximated by the Monte Carlo sample, there is a disagreement for the x_γ^{det} distribution. The direct peak at high values as well as the low-x_γ^{det} behaviour of the data is not reproduced by PYTHIA. A discussion concerned with the deviation of data and MC expectations in the cross section measurement will follow in the last chapter.

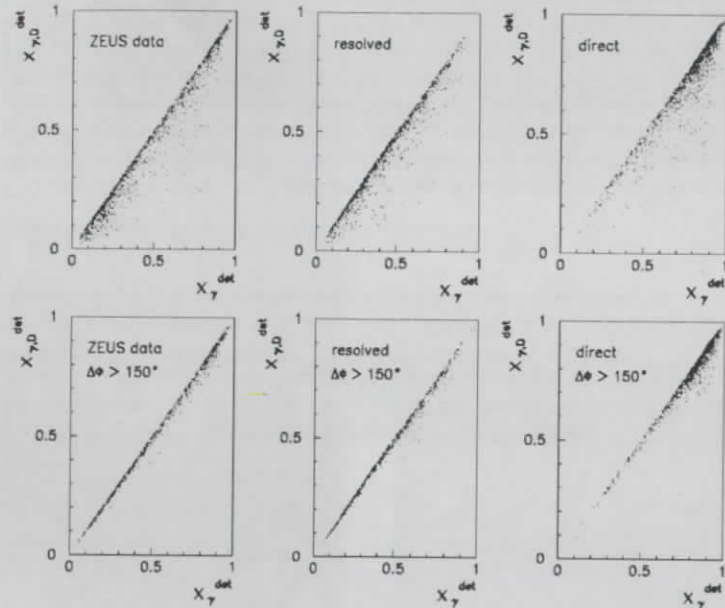Still, qualitatively, the peak at $x_\gamma^{det} \approx 0.85$ is a clear signature of the direct process

Figure 6.5: Scatter plots of $x^{\text{det}}_{\gamma,D}$ versus x^{det}_γ
The figure shows scatter plots of $x^{\text{det}}_{\gamma,D}$ and x^{det}_γ, calculated using the D'Agostini-Monaldi approach and the conventional reconstruction method, respectively, for the complete dijet sample and the subsample with $\Delta\phi > 150°$ of data, resolved and direct events.

and shows that only a combined sample of resolved and direct events is in principle able to describe hard photoproduction in ep-collisions.

Energy deposition of the photon remnant

In the resolved case, a fraction x_γ of the photon momentum enters into the hard interaction while the photon remnant carries the energy $E_{\text{rem}} = (1 - x_\gamma)yE_e$. The energy flow of the photon remnant is approximately in the direction of the incoming electron and causes energy deposition in the backward region close to the beam pipe, where the contribution of the direct process is small. In order to check the simulation of the photon remnant in PYTHIA 5.6 using the GRV-LO photon parametrization,
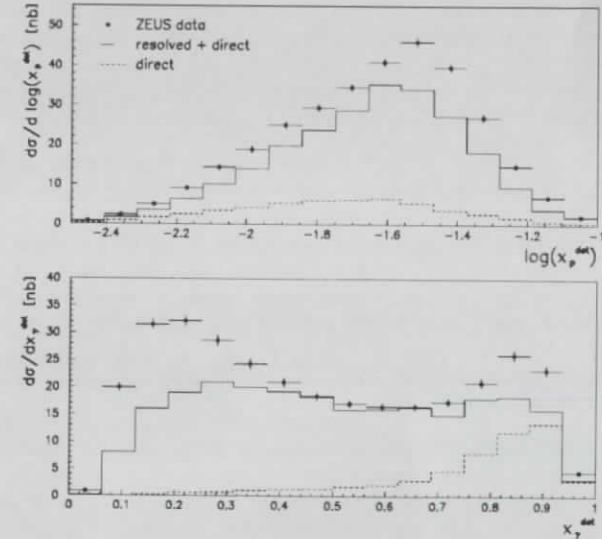

Figure 6.6: Uncorrected cross section of $d\sigma/d\log(x^{\text{det}}_p)$ and $d\sigma/dx^{\text{det}}_\gamma$
The plots show uncorrected differential cross sections of x^{det}_p and x^{det}_γ for data (dots) and PYTHIA 5.6 (full line) using the GRV-LO and the MRSD- parton distributions for the photon and the proton, respectively. The direct contribution, which is included in the PYTHIA prediction, is drawn separately (dashed line).

the energy E_{back}, which is collected in cone of $45°$ around the electron direction, is compared with the data. This definition of E_{back} differs slightly from the back energy as used in the D'Agostini approach, where the cone is defined by the most backward scattered jet. An estimate of the photon remnant energy in using a fixed cone is more adopted to the resolved/direct separation as proposed by Owens. Fig. 6.7 depicts E_{back} and relative quantities such as $E_{\text{back}}/E_{\text{tot}}$, $E_{\text{back}}/(E_{\text{BCAL}} + E_{\text{RCAL}})$ and $E_{\text{back}}/M_{\text{jet1jet2}}$. While E_{back} is in good agreement for data and PYTHIA 5.6 (full line) including direct and resolved contributions, the distributions of the normalized back energy $E_{\text{back}}/E_{\text{FCAL}}$ differ in the whole range. Of course, this reflects the energy excess in the forward region. For instance, $E_{\text{back}}/(E_{\text{BCAL}} + E_{\text{RCAL}})$, where the back energy is normalized to the energy sum of BCAL and RCAL or the distribution of $E_{\text{back}}/M_{\text{jet1jet2}}$ with a normalization to the invariant dijet mass lead to good agreement with the Monte Carlo prediction.
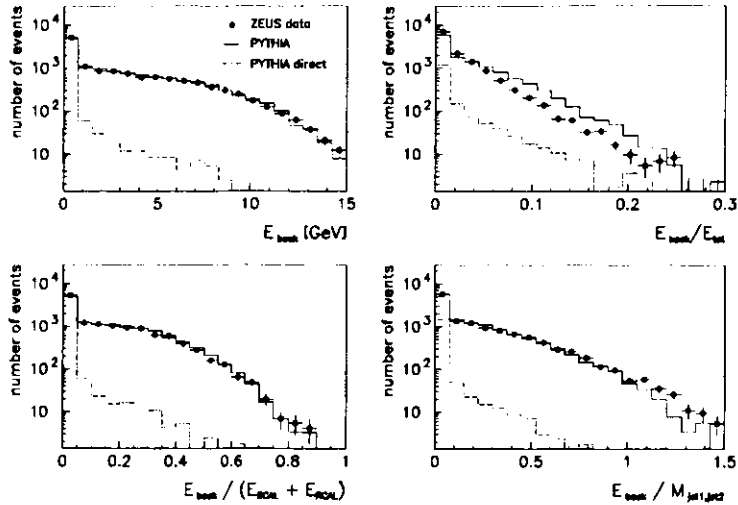
Figure 6.7: Backward energy deposition

Distributions of the energy E_{back} in a cone of $45°$ around the electron direction, and E_{back}/E_{tot}, $E_{back}/(E_{BCAL} + E_{RCAL})$, $E_{back}/M_{jet1,jet2}$, where the back energy E_{back} is normalized to the total energy E_{tot}, the energy sum of BCAL and RCAL $E_{BCAL} + E_{RCAL}$, and the invariant dijet mass $M_{jet1,jet2}$. Data, and PYTHIA distributions are marked by dots and full line. The direct contribution (broken line) is shown separately.

Separation of resolved and direct component

This section discusses which separation between resolved and direct events can be achieved by different cuts. In particular for the analysis of the forward energy excess, different separation methods will demonstrate, that the energy excess is related to a physical process, not considered in the Monte Carlo generation, and is not caused by detector effects or the detector simulation. In chapter 3, it is pointed out that a cut on x_γ or on a quantity related to the energy deposition of the photon remnant can be applied to separate resolved and direct contributions. This is confirmed by the distribution of x_γ^{det} and E_{back} as shown in Fig. 6.6 and Fig. 6.7, where the different contributions of resolved and direct events are displayed.

Applying a cut of $x_\gamma^{det} < 0.75$ on the PYTHIA sample, a subsample of resolved events is obtained, with a contamination of 9.2% of direct events. Similar results are
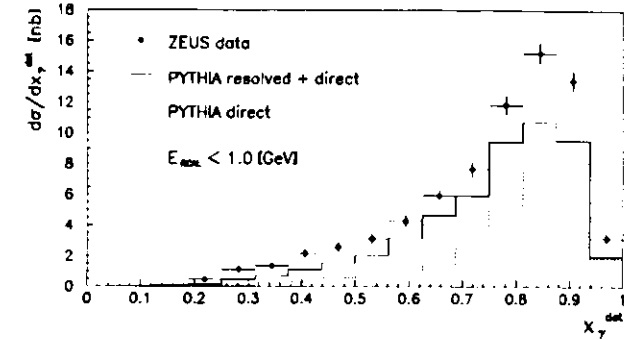

Figure 6.8: Uncorrected cross section $d\sigma/dx_\gamma^{det}$ for $E_{RCAL} < 1\,GeV$

achieved by use of the conditions $E_{RCAL} > 1\,GeV$ or the tighter cut $E_{back} > 2.0\,GeV$, which lead to direct backgrounds of 14.2% and 5.5%, respectively. It should be noticed, that these energy cuts reject also the high-x_γ resolved component, which is characterized by low energy photon remnants.

The separation of a clean resolved sample is favoured by the higher cross section of the resolved process. The ratio of direct to resolved contributions, generated with $p_{t,min} = 2.5\,GeV$, is approximately given by $\sigma_{dir}/\sigma_{res} \approx 1 : 7$, with a dependence on the used photon structure function. In photon proton scattering, as $p_{t,min}$ is increased the direct contribution becomes more important. For instance, in a Monte Carlo sample generated with $p_{t,min} = 6.0$, one obtains a ratio of about $\sigma_{dir}/\sigma_{res} \approx 1 : 3.5$. The choice of the $p_{t,min}$ value depends mainly on the threshold for the transverse jet momenta. In the chapter *Dijet Cross Sections* it will be shown, that for the present analysis a low value of $p_{t,min} = 2.5\,GeV$ is required.

A problem in the separation of a direct sample by use of cuts, which are based on backward energy, is the component of the resolved process with low energy deposition in RCAL. Conditions like $E_{back} < 2.0\,GeV$ or $E_{RCAL} < 1\,GeV$, result in samples with resolved contributions of 60% and 42%, respectively. However for some applications it is sufficient to select a high-x_γ sample. Beside a cut on x_γ^{det}, this can be achieved by requiring low values of E_{back} or E_{RCAL}. Fig. 6.8 displays the reconstructed x_γ^{det}-distribution, selected by the condition $E_{RCAL} < 1\,GeV$. The resolved/direct separation by use of energy measurements without any use of the reconstructed jets is an interesting alternative and provides an independent method for the separation.

6.1.3 The energy excess in the forward direction

For the distribution of the FCAL energy, the Monte Carlo simulation is not able to predict the energy flow as observed in data. This disagreement has led to questions concerning the reliability of the event generation by PYTHIA and the detector simulation. The measured energy excess could be caused by different mechanisms. The discrepancy could be a consequence of a wrong detector simulation. In this case, the whole analysis is affected. Other mechanisms could be energy depositions of the proton remnant or a missing process not considered on the generator level. An energy excess, due to background, can be excluded, because of the low contamination with beam-gas events.

In the following analysis, it will be shown that the energy excess in the forward calorimeter is related to the resolved process and is not observed in the direct case. The absence of additional energy in the direct process will demonstrate, that a wrong detector description is not responsible for the observed effect. Furthermore, a different behaviour of the proton remnant becomes also very unlikely, because both processes are characterized by two outgoing coloured partons with a large overlap in the kinematic range of x_p. Therefore, it is expected, that the extra energy in the forward region must be explained by a modification of the resolved process. The multiple interactions model, provided by PYTHIA 5.7, is such an approach. It will be discussed in the last chapter.

Forward energy for resolved and direct samples

The separation cuts of the previous section are used to investigate the forward energy flow. For the application of the x_γ^{det} cut, it must be considered, that the x_γ^{det} calculation could be influenced by the extra forward energy, because the extra energy affects the y_{JB} measurement. However, only a small effect is expected, due to the small polar angles of the forward direction. The production of additional forward jets used for the kinematic calculations could be more critical. Both cases lead to a shift to lower reconstructed x_γ^{det} values. The possibility, that direct events, accompanied by additional forward energy are moved into the resolved sample, so that the remaining direct sample includes only events without energy excess, is checked by using three different separation cuts. First, the dijet sample is separated by a cut on x_γ^{det}, which is sensitive to the mentioned effects.

Fig. 6.9 (a) shows the FCAL energy distribution of the total dijet sample for data (dots) and a mixed MC sample of resolved and direct events (full line). Resolved and direct subsamples are given in Fig. 6.9 (b) and Fig. 6.9 (c), respectively. While the E_{FCAL} distribution of the resolved sample is characterized by a tail to high values, the direct sample is in reasonable agreement with the PYTHIA expectations.

The influence of y_{JB} on the x_γ^{det}-measurement is checked by use of the LUMI tagged subsamples. A subsample of 25 % of events, having a scattered electron with $\Theta < 6\,\text{mrad}$, is collected by the LUMI detector which provides a very precise deter-
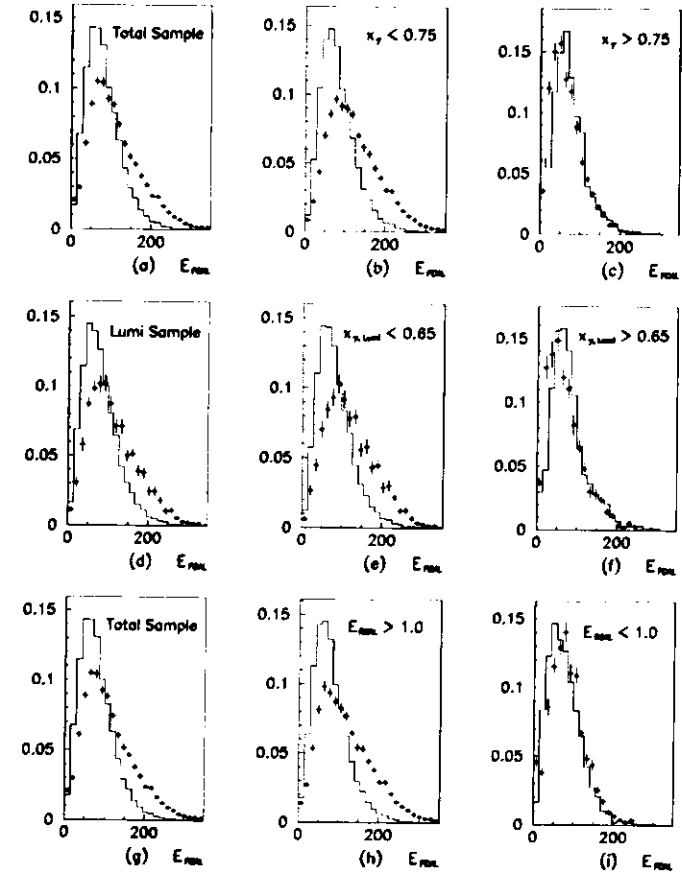
Figure 6.9: FCAL energy distributions

Fig. (a)-(c) show the FCAL energy of the total, resolved and direct dijet sample, using a separation cut at $x_\gamma^{det} = 0.75$, for data (dots) and a sample of PYTHIA 5.6 (full line) generated with the GRV-LO photon parametrization. In Fig. (d)-(f), the same plots are presented for Lumi tagged events, using a cut on $x_\gamma^{lumi} = 0.65$, where y is calculated from the scattered electron. Fig. (g)-(i) display the total sample and resolved and direct subsamples, obtained by a cut on $E_{RCAL} = 1\,\text{GeV}$.

mination of the true y, independently from any activity in the main detector. For the Lumi tagged data and MC samples, x_γ^{lumi} is computed replacing y_{JB} by y_{lumi} in Equ. 2.76, where y_{lumi} is calculated from the energy of the scattered electron E_e'; $y_{\text{lumi}} = 1 - E_e'/E_e$. A cut at $x_\gamma^{\text{lumi}} = 0.65$ takes into account the shift of the x_γ distribution to lower values, du to the fact, that the reconstructed y_{lumi} is approximately 20 % higher than the measured y_{JB}. Fig. 6.9 (d)-(f) depict the total Lumi sample and its resolved and direct subsamples. The direct distributions are again in agreement for data and Monte Carlo.

The possibility of additional jet production in the forward region is checked by use of the RCAL energy cut. Separating the dijet sample by a cut on $E_{\text{RCAL}} = 1\,\text{GeV}$, gives a high-$x_\gamma^{\text{det}}$ sample, which is completely independent from the reconstructed jets and y_{JB}. Fig. 6.9 (g)-(i) show distributions of the result of the E_{RCAL} separation, which confirms, that the energy excess of the forward direction is related to the resolved process, while the direct process shows no deviation from Monte Carlo predictions. With this result, it is indicated, that the observed differences between data and Monte Carlo expectations are not caused by a wrong detector description.

6.2 Detector Effects

Interactions of final state particles with the material in the detector cause acceptance and smearing effects. Due to the imperfection of the detector, two effects are observed. The first effect is a reduced probability (acceptance) to measure a given event in a given kinematical region. The second is related to detector resolution and misidentification of a measured quantity, which leads to deviation of a reconstructed value from the true value. In order to statistically determine the true value from the reconstructed variable, detector simulations are used to obtain the corrections, which have to be applied on the measured quantity. The method, which is used to compute a true distribution from the corresponding measured one, is the so-called *unfolding* procedure. While the correction for acceptance is straight forward, the situation becomes completely different, if migration effects play an important role. Therefore, a main criterion for the chosen unfolding method is given by the detector resolution.

6.2.1 Reconstruction of y_{JB}

The aim of this work is the measurement of dijet cross sections in a photon-proton center-of-mass energy range $s_{\gamma p} = E_{\text{cm}}^2$, which is determined by y, with $s_{\gamma p} = y s_{ep} = y \cdot 4 E_e E_p$. For the calculation of $d\sigma/dx_\gamma$, events are selected according to their reconstructed y_{JB}-value. In the description of the off-line filter, it is outlined that a reliable data selection is limited to the range $0.15 < y_{\text{JB}} < 0.7$. Now, the question is, which range of the generated y_{gen} variable corresponds to the chosen region of y_{JB}? Fig. 6.10 depicts two scatter plots of y_{gen} versus y_{JB} for resolved and direct events, which are accepted by the data selection cuts; y_{JB} is systematically smaller in both
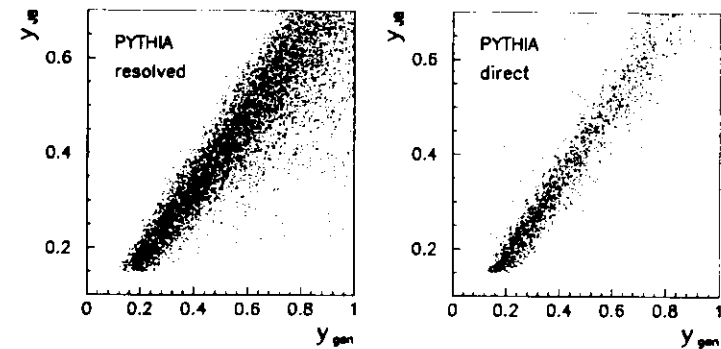
Figure 6.10: Scatter plots of y_{JB} versus y_{gen}

cases. The observed migration effect of the resolved sample in the high-y_{gen} region is probably caused by energy loss of the photon remnant through the beam pipe. Due to the large migration in the high-y_{gen} region, it is reasonable to restrict the range of the generated distribution in the following corrections to values below $y_{\text{gen}} = 0.8$, so that the accessible region of the reconstructed y_{JB} corresponds to the kinematic window

$$0.2\,s_{ep} < s_{\gamma p} < 0.8\,s_{ep} . \tag{6.1}$$

Using the electron and proton beam energies of $E_e = 26.7\,\text{GeV}$ and $E_p = 820\,\text{GeV}$, respectively, $\sqrt{s_{\gamma p}}$ covers the range between $132\,\text{GeV}$ and $265\,\text{GeV}$.

In cases of a y_{JB} measurement, the true value of y is precisely obtained by a measurement of y_{lumi}, using the scattered electron. Fig. 6.11 shows the relative difference $(y_{\text{JB}} - y_{\text{lumi}})/y_{\text{lumi}}$ for data and the PYTHIA prediction. The distributions have been fitted to Gaussian functions. The results for data and Monte Carlo compare very well. The mean value of the PYTHIA distribution demonstrates, that a measurement of y_{JB} is too small by 19.9 %, while a fit to the data distribution gives a value of 20.1 %.

6.2.2 Measurement of transverse jet momenta

It has been mentioned in the description of the jet algorithm, that the definition of jets is a matter of convention. One of the parameters is the minimum value of transverse jet momenta that can be accepted, to justify a perturbative QCD description. For
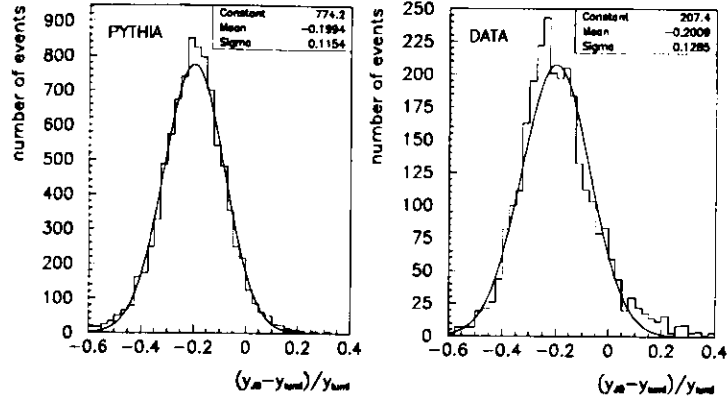
Figure 6.11: Relative deviation of y_{JB} from the y_{lumi} value for data and PYTHIA
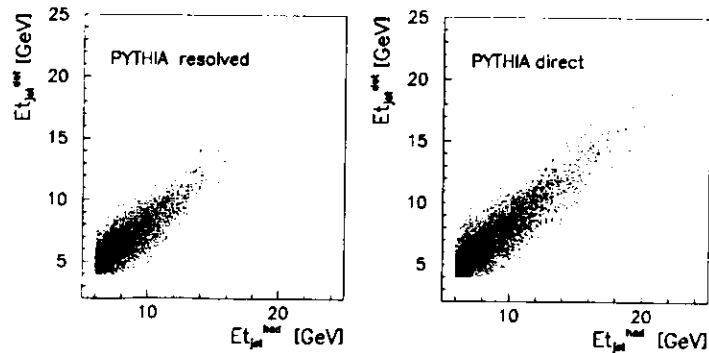

Figure 6.12: $E^{det}_{t,jet}$ versus $E^{had}_{t,jet}$

this analysis, detector jets of at least 5 GeV are selected and are compared with hadron jets with $E^{had}_{t,min} > 6$ GeV, where the lower threshold value for detector jets takes into account energy loss due to inactive material.

Fig. 6.12 depicts scatter plots of transverse jet momenta for detector and hadron jets in resolved and direct processes. The threshold value of the detector jets is lowered to $E^{det}_{t,min} = 4$ GeV to indicate the rejected region below $E^{det}_{t,min} = 5$ GeV. It is shown, that the correlation of the transverse momenta of detector and hadron jets is poor in the low E_t region. The influence, due to inactive material and smearing effects of the calorimeter on energy measurements can be estimated by distributions of $\Delta E_{t,jet} = (E^{det}_{t,jet} - E^{had}_{t,jet})/(E^{had}_{t,jet})$ and $\Delta y = (y_{JB} - y_{gen})/y_{gen}$, as shown in Fig. 6.13. The mean values of fitted Gaussian functions indicate a similar shift to lower values. Transverse jet momenta of detector jets and y_{JB} differ by 16.3 % and 19.9 %, respectively, from their generated values. Note, that the Δy distribution reproduces exactly the deviation between y_{JB} and y_{lumi}, which confirms that the MC is a good approximation of reality.

The underestimation of transverse jet energies on the detector level is considered by lowering of the threshold values from $E^{had}_{t,jet} \geq 6$ GeV for hadron jets to $E^{det}_{t,jet} \geq 5$ GeV on the detector level.

The correlation between hadron jets and detector jets, as shown in Fig. 6.12, means, that reconstructed variables using jet energies, such as x_γ, have to be corrected for cross section calculations. A two dimensional correction of transverse jet momenta, as a function of $E_{t,jet}$ and η_{jet} is carried out in [67]. One advantage in cross section measurement of jet rapidities is the possibility to avoid such complicated correction
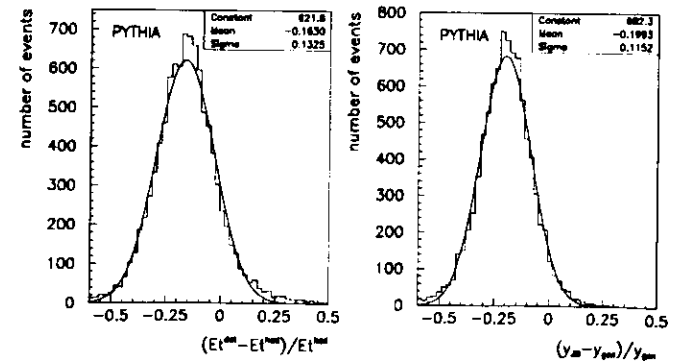

Figure 6.13: Comparison of reconstructed and generated variables

procedures, because the correlation of the jet rapidities between detector jets and hadron jets is very well, as shown in the next section.

6.2.3 Resolution of the jet reconstruction

The accuracy of the cross section measurement $(d\sigma/d\eta)_{\eta_1,\eta_2}$ is based mainly on the quality of the reconstruction of jets in the calorimeter. The calorimeter resolution can be estimated by comparison of hadron jets with their associated detector jets. Since in a given event several jets are found on hadron and on detector level, the meaning of an *associated detector jet* has to be defined. A pair of a hadron and a detector jet is regarded as a corresponding jet pair, if the distance in η-ϕ space of hadron and detector jet is less than 0.5, which is half of the chosen cone radius of the jet-finding algorithms.
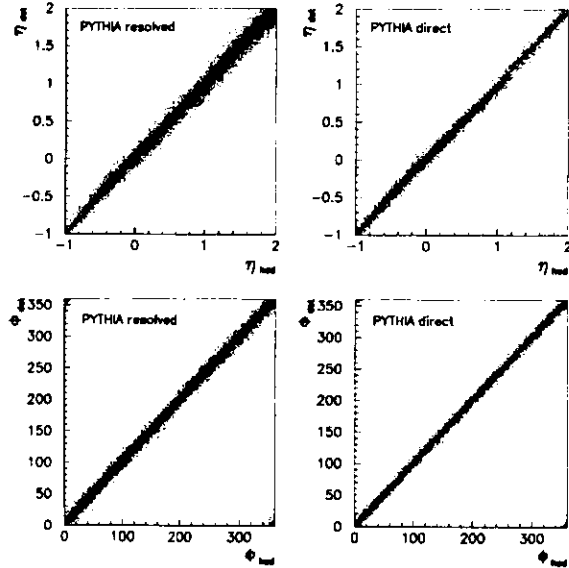

Figure 6.14: Scatter plot of jet variables

Scatter plots of the angle variables η_{jet} and ϕ_{jet} of hadron jets and their associated detector jets are shown for resolved and direct PYTHIA samples.
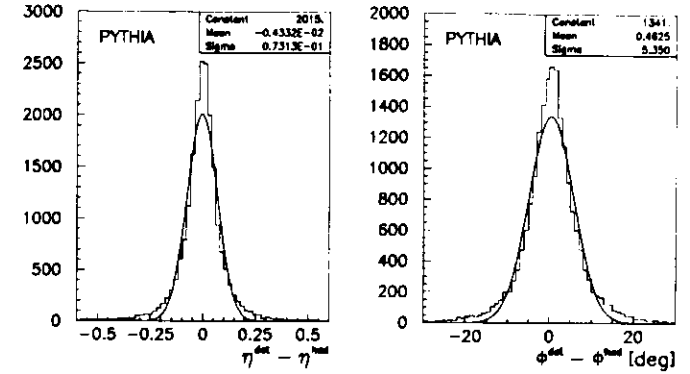
Figure 6.15:

Comparison of rapidity η and azimuth angle ϕ for detector and hadron jets.

The sample of hadron jets is selected by $0.2 < y_{gen} < 0.8$ and $E_{t,jet}^{had} > 6\,\text{GeV}$. For the corresponding detector jets a transverse energy of $E_{t,jet}^{det} > 5\,\text{GeV}$ is required. Fig. 6.14 shows scatter plots of the jet variables η_{had} versus η_{det} and ϕ_{had} versus ϕ_{det} for resolved and direct events separately. Hadron jets, without a corresponding detector jet are rejected. The scatter plots demonstrate that the cone axes of hadron jets are well correlated with the ones of the detector jets.

	PYTHIA		HERWIG	
	mean	σ	mean	σ
$\Delta\eta_{jet}$	-0.004	0.073	-0.004	0.059
$\Delta\phi_{jet}$	$0.5°$	$5.4°$	$0.3°$	$4.4°$
$\Delta E_{t,jet}$	-16.3%	13.3%	-15.3%	12.7%
Δy	-19.9%	11.5%	16.6%	12.1%

Table 6.2: Mean and rms spread σ for the distributions
$\Delta\eta_{jet} = (\eta_{jet}^{det} - \eta_{jet}^{had})$, $\Delta\phi_{jet} = (\phi_{jet}^{det} - \phi_{jet}^{had})$, $\Delta E_{t,jet} = \frac{E_{t,jet}^{det} - E_{t,jet}^{had}}{E_{t,jet}^{had}}$ and $\Delta y = \frac{y_{JB} - y_{gen}}{y_{gen}}$.

Distributions of $\Delta\eta = \eta_{det} - \eta_{had}$, $\Delta\phi = \phi_{det} - \phi_{had}$ and fitted Gaussian functions are displayed in Fig. 6.15. In contrast to the transverse jet momenta, the angle

variables η_{jet} and ϕ_{jet} are reconstructed without systematic bias and the jet resolution
of the detector is better than 6° for ϕ_{jet} and 0.08 units for η_{jet}. Shift and resolution
of the jet variables η_{jet}, ϕ_{jet}, $E_{t,jet}$ and the measurement of y_{JB} are summarized in
table 6.2. The values as predicted by the HERWIG generator are also shown. Both
generators agree in $\Delta\eta_{jet}$, $\Delta\phi_{jet}$ and $\Delta E_{t,jet}$, while the mean of Δy is approximately
3 % smaller for the HERWIG simulation.

6.3   Summary

In summary, it has been shown that the general event characteristics of the data
are approximately described by the PYTHIA generator and the detector simulation,
except for quantities which are affected by forward energy. Jet characteristics, such as
track multiplicity, jet energy and transverse jet energy as well as the jet multiplicity
itself, compare well with PYTHIA predictions. The shape of the uncorrected cross
section of x_γ^{det} shows, however, a large difference between data and PYTHIA. For
the direct process, the distribution of the FCAL energy is remarkably described by
PYTHIA MC, while in the resolved case a large energy excess in the data is observed,
not predicted by the standard PYTHIA simulation. Comparison of detector and
hadron jets have shown an excellent resolution of the calorimeter for the measurement
of ϕ_{jet} and η_{jet}. Both quantities are reconstructed without systematic bias and a
resolution better than 6° for ϕ_{jet} and 0.08 units for η_{jet}. In contrast the measurement
of transverse jet energies shows an underestimation of about 16 % compared to the
generated values.

Chapter 7

Dijet Cross Sections

In perturbative leading order QCD, hard photoproduction of resolved and direct pro-
cesses is described by a hard scattering process with two outgoing partons. The
rapidity distribution of these partons $(d\sigma/d\eta_{par})_{n_1,n_2}$ (with two entries per event) is
determined by the LO–QCD matrix elements and the parton distributions of the pho-
ton and the proton. The outgoing partons produce jets of hadrons, so-called hadron
jets. Since the partons cannot be observed directly, quantities related to the partons,
such as η_{par}, x_γ and x_p are reconstructed from the measured hadron jets. In a pure
LO–QCD scenario, there is a strong correlation between the hard scattered partons
and the observed hadron jets. Distributions of parton variables like $(d\sigma/d\eta_{par})_{n_1,n_2}$,
can be studied by measuring of the corresponding jet distribution. The LO–QCD
description, however, is an approximation and higher-order QCD radiation leads to
additional parton activity and makes the interpretation of jet distributions more com-
plicated. Due to the parton shower radiation, the jet rapidity is not only determined
by the hard scattering process as in an idealized LO–QCD scenario. Therefore, an
estimation of the contribution of parton shower induced jets is needed for the under-
standing of the cross section measurement.

There are two different types of cross sections. The first one is the hadron jet
cross section $(d\sigma/d\eta_{had})_{n_1,n_2}$, where only detector effects have to be corrected. Due
the good correlation of hadron jets and their associated detector jets, as shown in the
previous chapter, detector effects can be corrected very precisely, and $(d\sigma/d\eta_{had})_{n_1,n_2}$
is obtained independently from Monte Carlo assumptions. The second is the parton
cross section $(d\sigma/d\eta_{par})_{n_1,n_2}$ as given by the hard scattering process. In this case,
Monte Carlo simulations of higher order QCD radiation are required to correct the
contribution of parton shower induced jets. It will be shown that QCD initial state
radiation from the photon side gives rise to a large amount of dijet events. (See
also the critical discussion [68] of the initial state shower model as used in PYTHIA
and HERWIG.) Due to this contribution in the dijet sample, complicated unfolding
procedures have to be applied to data, which lead to a dependence of the cross section
measurement on the parton shower model used.

A further aspect of higher order QCD radiation is related to the choice of the low

value of $p_{t,min} = 2.5$ GeV in the MC generation. The aim of this work is the measuring of hadron jets with a transverse energy of $E_t > 6$ GeV. Obviously these hadron jets cannot be produced by partons with a transverse momentum of $p_t = 2.5$ GeV. In the discussion of parton shower effects, it is shown, that the observed jets of low-p_t dijet events are mainly produced by parton shower radiation.
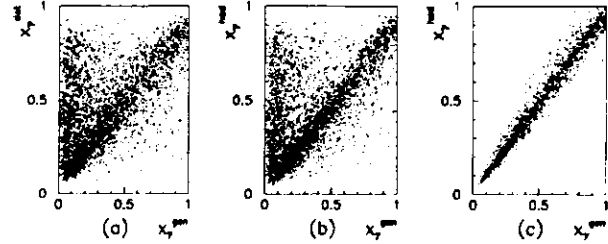

Figure 7.1: Reconstructed versus generated x_γ
Scatter plots of x_γ^{det} versus x_γ^{gen}, Fig. (a), x_γ^{had} versus x_γ^{gen}, Fig. (b). Fig. (c) shows x_γ^{had} versus x_γ^{gen} for a sample generated without use of the parton shower model.

7.1   Initial State QCD Radiation

The following discussion of parton shower radiation concentrates on initial state radiation from the resolved photon, which is the main source of parton shower induced dijet events. As an illustration, consider a typical *initial state* event with low x_γ^{gen}, with two outgoing jets in the forward direction and an initial state jet from the resolved photon in the backward direction. If one of the two forward jets is not detected, due to its high rapidity, the remaining jet pair consists of one forward jet and an initial state jet in the backward direction, which causes large reconstructed values of x_γ^{had} and x_γ^{det}.

This example indicates a convenient method for the study of parton shower effects. Due to the exponential dependence of x_γ on the jet rapidities, as shown in Equ. 7.1, parton shower induced dijet events can be identified by comparing the generated x_γ value with the reconstructed one.

$$x_\gamma = \frac{1}{2y E_e}\left(E_{t,jet1}\exp(-\eta_{jet1}) + (E_{t,jet2}\exp(-\eta_{jet2}))\right) \qquad (7.1)$$

The main aspects of parton shower effects become clear in the discussion of Fig. 7.1. Fig. 7.1.(a) and (b) display scatter plots of x_γ^{det} and x_γ^{had} versus generated x_γ^{gen}, in which x_γ^{had} is calculated using the hadron jets and the generated y-value. One part of the events fall on the diagonal, while a considerable fraction of low-x_γ^{gen} events shows no correlation between generated and reconstructed values. These so-called misidentified events are not caused by detector effects, which is demonstrated by the similarity of Fig. 7.1 (a) and Fig. 7.1 (b). The expression *misidentified* is used in the sense, that the observed jets are not produced by the outgoing partons of the hard interaction, but by at least one other parton resulting from the parton shower evolution.

In order to demonstrate the influence of the parton shower model, a sample without parton shower evolution (which also turns off automatically the evolution of the photon remnant) has been generated. Fig. 7.1 (c) presents the corresponding scatter
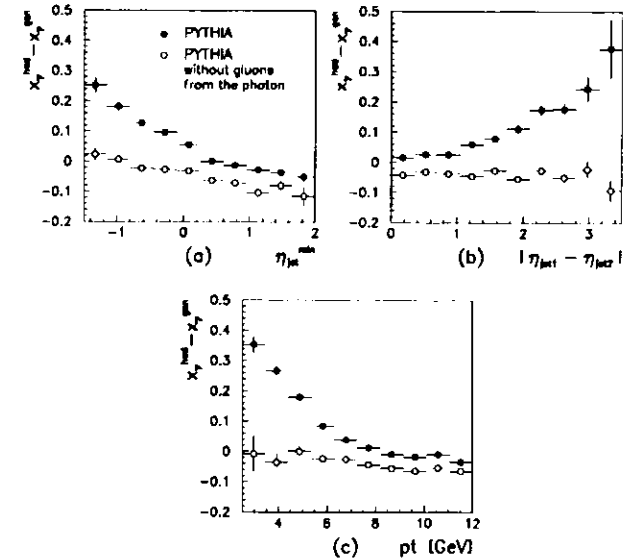

Figure 7.2:
Plots of $(x_\gamma^{had} - x_\gamma^{gen})$ vs. η_{jet}^{min} (a), $(x_\gamma^{had} - x_\gamma^{gen})$ vs. $|\eta_{jet1} - \eta_{jet2}|$ (b) and $(x_\gamma^{had} - x_\gamma^{gen})$ vs. p_t (c) for the total PYTHIA sample (full circles) and a sample excluding the gluon contribution of the photon (open circles).

plot x_γ^{had} versus x_γ^{gen}. Misidentification is not observed and the events are concentrated on the diagonal. The remaining smearing is produced by lost particles not detected in the cone radius of one.

The interpretation of misidentified events by a jet topology with one parton jet in the forward direction and one initial state jet in the backward direction will be demonstrated by measuring $(x_\gamma^{had} - x_\gamma^{gen})$ versus the rapidity of the most backward scattered jet and as a function of the rapidity gap between the two jets $|\eta_{jet1} - \eta_{jet2}|$. This is shown in Fig. 7.2 (a), and Fig. 7.2 (b). Results of the complete MC sample and of a sample excluding the gluon contribution of the photon are presented. While the total sample exhibits the expected behaviour, namely increase of $(x_\gamma^{had} - x_\gamma^{gen})$ at low η_{jet}^{min} values and for large rapidity gaps $|\eta_{jet1} - \eta_{jet2}|$, this is not observed for the quark contribution of the photon. This shows that the gluon content of the photon is responsible for most of the wrongly reconstructed x_γ values.

The small deviation to negative values of the quark sample in Fig. 7.2 (a) probably indicates effects due to initial state radiation from the proton or from final state shower evolution in the forward direction.

The correlation of initial state parton shower radiation with the transverse momentum p_t of the hard scattered partons is checked by $(x_\gamma^{had} - x_\gamma^{gen})$ versus p_t as shown in Fig. 7.2 (c). One can see, that large values of $(x_\gamma^{had} - x_\gamma^{gen})$ correspond to the low-p_t range, which demonstrates that low-p_t dijet events are measured, due to the occurrence of initial state induced jets. This is the reason for the choice of a low
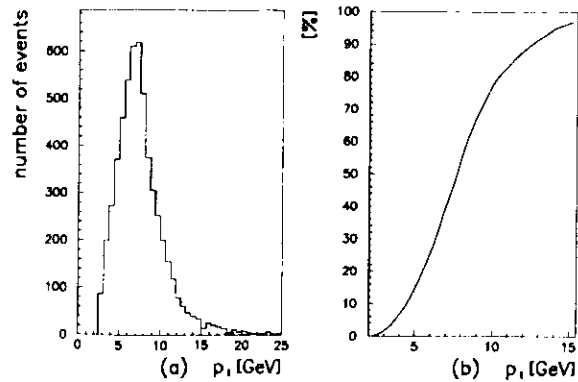

Figure 7.3:
Spectrum of pt_{min} (a) and its integral (b) for the PYTHIA dijet sample.

$p_{t,min}$ value in the Monte Carlo generation. The p_t-spectrum of the MC dijet sample and the fraction of events with a value below p_t are shown in Fig. 7.3 (a) and (b), respectively. A choice of $p_{t,min} = 2.5$ GeV includes almost the whole contribution of parton shower induced jets, while a MC generation with $p_{t,min} = 6.0$ GeV would neglect approximately 25 % of the dijet sample.

In summary, the dijet sample is strongly affected by initial state radiation. Therefore, unfolding back to the parton level requires a precise estimation of the parton shower induced jet contribution, which introduces a dependence on Monte Carlo assumptions in the measurement of the parton cross section $(d\sigma/d\eta_{par})_{\eta_1,\eta_2}$. Further, it is shown that the fraction of parton shower induced events depends on the chosen value of $p_{t,min}$. Thus, different values of $p_{t,min}$ will lead to a change of the unfolding procedure. These problems are avoided in a cross section measurement $(d\sigma/d\eta_{had})_{\eta_1,\eta_2}$ of hadron jets, where only detector effects have to be corrected. The next section gives a description of the corrected jet cross section measurement $(d\sigma/d\eta_{had})_{\eta_1,\eta_2}$, in the following $(d\sigma/d\eta)_{\eta_1,\eta_2}$ for short, for dijet events in the kinematic region given in section 5.4.

7.2   Dijet Cross Section

The aim is the measurement of the photoproduction dijet cross section in a kinematic region defined by $Q^2 < 4$ GeV^2, $E_{t,jet} > 6$ GeV and $0.2 < y < 0.8$. The analysis of the previous chapter has shown, that detector effects lead only to small differences in the reconstructed η_{jet} and ϕ_{jet} variables, comparing detector and hadron level. The good calorimeter resolution of $\Delta\eta_{jet} = 0.07$ in units of rapidity and the good correlation between hadron and detector jets, shown in Fig. 6.15, permits the use of a bin-by-bin correction of migration and detection efficiency. The bin-by-bin unfolding method is not independent of the used structure functions. However, for structure functions, which are similar in shape, differences of correction factors, developed for different parametrizations, are negligible compared with detector effects and can be considered as a small systematic uncertainty.

7.2.1   Bin-by-bin data correction

Jet rapidities are measured in the range $-1 < \eta_{jet} < 2$ using 14 bins. In order to estimate detector acceptance, purity and correction factors for each bin i, three distributions of jet rapidities are selected for the simulated event sample.

- N_i^{had} denotes the number of hadron jets with $Q^2 < 4$ GeV^2, $E_{t,jet} > 6$ GeV in the region $0.2 < y < 0.8$ in bin i.

- N_i^{det} denotes the number of detector jets requiring trigger and offline data selection, including cuts on $0.15 < y_{JB} < 0.7$ and $E_{t,jet} > 5$ GeV.

- N_i^{good} denotes the number of hadron jets of so-called good dijet events with two detector jets and two hadron jets passing the conditions of N_i^{had} and N_i^{det}, respectively.

The hadron jet distribution N_i^{had} represents the generated distribution. Due to detector effects and different selection cuts for the hadron jet and the detector jet sample, a transformed detector jet distribution N_i^{det} is measured. The hadron jet distribution can be restored by a bin-by-bin correction, where each bin of the detector distribution is multiplied with a correction factor, defined by the ratio of hadron jets to detector jets. In order to study also separately acceptance and purity of the measurement, the above distributions are used to define:

$$A_i = \frac{N_i^{good}}{N_i^{had}}, \qquad P_i = \frac{N_i^{good}}{N_i^{det}}, \qquad C_i = \frac{N_i^{had}}{N_i^{det}}$$

where A_i, P_i, C_i denote acceptance, purity and correction factors for each bin. The reliability of this simple correction method is checked by comparing the expectations of purity acceptance and correction factors for PYTHIA with the outcome of the HERWIG generator. Fig. 7.4 shows estimates for both generators. It is seen, that the predictions of PYTHIA and HERWIG agree very well.

The distribution of the purity is flat in the whole rapidity range, with an average value of about 60 %, except for the first and last bin. The low values of the last bins in purity and acceptance plots are caused by shifts due to the calorimeter resolution and the missing neighboring bins. For instance, detector events in the last bin with a corresponding hadron jet $\eta_{jet}^{had} > 2$ are counted in N_i^{det} but not in N_i^{good}, which leads to a lower purity. These kind of migration exist for all bins, but due to the smooth rapidity distribution, the loss of entries per bin is compensated by migration from neighboring bins of both sides, which is not the case for the first and last bins. Due to the same migration shifts in the acceptance plot, the decrease of the last bin in the purity plot is canceled, so that the correction factor is not affected.

The acceptance is slowly changing with a plateau of 55 % between $0 < \eta_{jet} < 0.7$ and dip at $\eta_{jet} = 1.3$, caused by the gap between FCAL and BCAL and different efficiencies of calorimeter triggers.

The correction function has a maximum at low rapidity values and is close to one in the forward direction. The large correction values of about 1.5 in the first three bins are caused by the low acceptance in this region, probably a result of the different $E_{t,jet}$ thresholds for detector and hadron jets.

The corrected experimental dijet cross section is computed by multiplying the number of entries N_i^{data} with the corresponding correction factor C_i and division of the bin width $\Delta\eta$.

$$\left(\frac{d\sigma}{d\eta}\right)_{m,n,i} = \frac{C_i \, N_i^{data}}{\mathcal{L} \, \Delta\eta} \qquad (7.2)$$
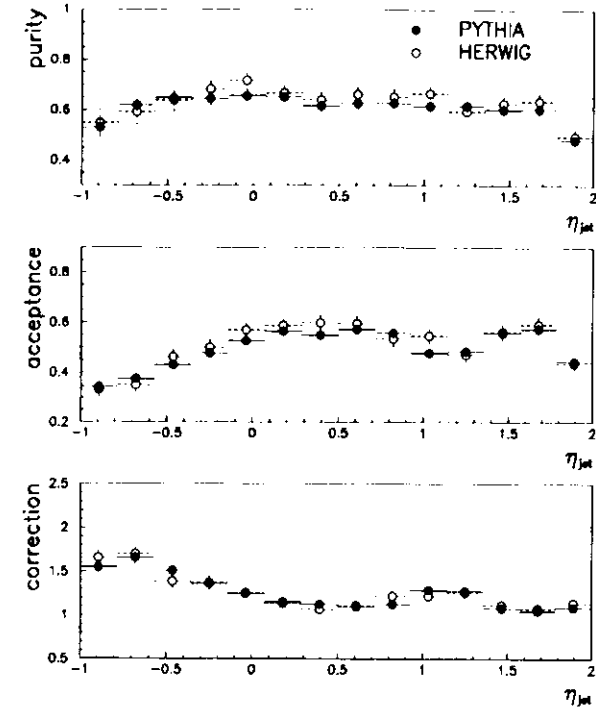
Figure 7.4: Purity (P_i), acceptance (A_i) and correction (C_i) factors

After normalization with the integrated luminosity of $\mathcal{L} = 545$ nb^{-1}, the differential dijet cross section $(d\sigma/d\eta)_{m,n}$ is obtained as shown in Fig. 7.5 and Fig. 7.6.

7.3 Systematic Errors

The systematic uncertainties have been studied by varying variables, which are used in the data selection and the computation of the dijet cross section. For each change of a variable, the cross section was recalculated and compared with the reference value in each bin. The reference values are obtained using the

- Monte Carlo generator: PYTHIA 5.6,

- proton structure function: MRSD-,

- photon structure function: GRV-LO,

- ratio of resolved and direct processes: given by the MC-Generator,

- jet algorithm: PUCELL with cone radius of one.

The first four items are considered in the estimate of the systematic error, while the last point does not contribute to a systematic uncertainty, because the cone algorithm and the cone radius are fixed conditions, which have to be applied in comparisons with theoretical computations. The changed items are divided into one part describing uncertainties of the above choices, and a second part, where variables used in data selection are varied. All changes are summarized in the following list and are described below:

- Monte Carlo Generator: HERWIG 5.7

- Proton Structure Function: MRSD0

- Photon Structure Function: LAC1

- Ratio of resolved and direct processes: $2 \cdot \sigma_{dir}/\sigma_{res}$

- Ratio of resolved and direct processes: $\frac{1}{2} \cdot \sigma_{dir}/\sigma_{res}$

Systematics checks of the data selection variables are carried out by the following variations in the Monte Carlo sample:

- $E_{t,cone} \geq 15\,\mathrm{GeV} \longrightarrow E_{t,cone} \geq 12\,\mathrm{GeV}$

- $p_z/E_{tot} < 0.94 \longrightarrow p_z/E_{tot} < 0.90$

- $y_{JB} \longrightarrow 0.95 \cdot y_{JB}$

- $E_{t,jet} \longrightarrow 1.05 \cdot E_{t,jet}$

- $E_{t,jet} \longrightarrow 0.95 \cdot E_{t,jet}$

The influence of the Monte Carlo generator is checked by comparing PYTHIA 5.6 with HERWIG 5.7 where a small change due to the fragmentation models is expected. Because of the lower statistic, the comparison is limited by the statistical error of the HERWIG sample, which leads to fluctuation in the error with values between 0.7 % and 8.6 %. The sign of the relative changes indicates the direction of the change.

The choice of the proton structure function leads only to a small decrease of about 1.0 %. This is due to the probed range of parton momentum fractions $x_p > 0.003$, where uncertainties of the gluon parametrization are still small. The change

of the photon structure function from GRV-LO to LAC1 reduces the cross section approximately by 5 % in the whole rapidity region.

Uncertainties due to the leading order resolved/direct mixing are estimated by a drastic change of the direct contribution. Increasing the direct cross section by a factor of two affects mainly the backward region, where the cross section becomes 7 % higher in the first bin, while the last bin is only increased by 2 %. Decreasing the direct component by a factor of two leads to a similar effect in the opposite direction; with values of -5 % and -1 % in the first and last bin, respectively.

The described uncertainties are added in quadrature and are drawn as thick error bars in the cross section plots of Fig. 7.5 and Fig. 7.6. Thin error bars of the statistical errors are negligible and within the full circles of the data points.

Uncertainties due to data selection

In the following, two systematic energy effects are taken into account. First, due to the forward energy excess, the variables p_z/E_{tot} and $E_{t,cone}$, which are used in the data selection show a systematic shift to higher values in data. This shift is taken into account by changing the cut values in the MC sample. The cut $E_{t,cone} = 15\,\mathrm{GeV}$ was reduced to $E_{t,cone} = 12\,\mathrm{GeV}$, affecting mainly the backward direction where the cross section of the first five bins decreases by about 12 %. The forward direction seems to be less sensitive to this cut with a reduction of about 5 % in the last six bins. The cut $p_z/E_{tot} = 0.94$ was varied to $p_z/E_{tot} = 0.90$ leading to the opposite dependence with small changes in the backward region and large differences in the forward direction. The cross section change increases progressively from 0.2 % in the first bin to 13 % in the last bin.

In [69] the influence of the detector description was checked by comparing y_{JB} y_{lumi} as a function of y_{lumi} for data and Monte Carlo samples. It is shown, that the y_{JB} reconstruction in MC is possibly overestimated by 5 % at high values. In order to consider this possibility, y_{JB} was varied to $0.95 \cdot y_{JB}$ with a resulting change of approximately -1 % in the range $\eta_{jet} > 0.2$ which increases up to 6.7 % towards the first bin.

In the same note [69], it is demonstrated that a possible uncertainty in the simulation of the calorimeter response can lead to differences in the transverse energy of jets of at most ± 5 %. Including a change of $E_{t,jet} \to 1.05 \cdot E_{t,jet}$ and $E_{t,jet} \to 0.95 \cdot E_{t,jet}$ lead to the main contribution of approximately ∓ 15 % in the whole rapidity range. Systematic errors which are connected with changes of the energy scale or the influence of the forward energy excess are calculated separately and are indicated by a grey band in Fig. 7.5 and Fig. 7.6.

7.4 The Dijet Cross Section $(d\sigma/d\eta)_{\eta_1,\eta_2}$

So far, two processes have been discussed, which possibly influence the dijet cross section as a function of the rapidity. The observation of an energy excess in the forward direction and higher order QCD radiation, as simulated by the parton shower model in Monte Carlo generators. The goal for this work is the investigation of the photon parametrization, where GRV-LO and LAC1 structure functions are used in a comparison of $(d\sigma/d\eta)_{\eta_1,\eta_2}$ to check an important property of the resolved photon, the gluon contribution at low-x_γ values.

In order to estimate the influence of the parton shower model, data are compared with a pure leading order QCD prediction without fragmentation. Then the same MC expectation is shown including string fragmentation and using the PUCELL cone algorithm with a cone radius $R_{cone} = 1.0$. Further, cross sections are evaluated with PYTHIA including the parton shower model with $p_{t,min} = 5.0$ GeV and $p_{t,min} = 2.5$ GeV to demonstrate the effects of low-p_t dijet events.

In Fig. 7.5 (a) the measured cross section is compared with the leading order QCD predictions. The direct contribution is drawn separately and it is seen that the forward direction is not affected by the direct process. The leading order QCD prediction is obtained by taking the two outgoing partons of the hard interaction with a cut of $p_{t,min} = 6$ GeV, without intrinsic k_t smearing of the partons in the proton and the resolved photon, without parton shower evolution and without fragmentation. Comparing these LO-PYTHIA predictions with analytical leading order dijet calculation has shown a good agreement. It is interesting, that the absolute normalization of the data is approximately described by the LO MC curves, which means, that the squared transverse momentum p_t^2 is indeed a good choice for the hard scale in conjunction with a first loop α_s coupling constant. The second result is, that the difference between the GRV-LO and LAC1 photon structure functions is too small, to be detectable with the data.

In Fig. 7.5 (b) the measured jet cross section is compared with the MC hadron jet cross section including fragmentation, but without parton shower evolution. In this case the LO QCD cross section decreases, due to the energy lost by partons which are outside of the cone radius. This plot demonstrates the strong influence of the cone radius and the necessity to include fragmentation in the comparison of data with analytical QCD computations. While the backward direction is roughly approximated within the systematic errors, there is a significant deviation in the forward region outside the systematic uncertainties.

In Fig. 7.6 (a) the predictive power of Monte Carlo simulations is tested by including k_t smearing and parton shower evolution with a cut of $p_{t,min} = 5.0$ GeV. It is shown, that the predicted shape is in better agreement with data. In addition, a difference between the GRV-LO and LAC1 expectation becomes visible in the whole rapidity range. This effect is caused by the higher gluon contribution of LAC1. As shown in the discussion of the parton shower effects, the gluon contribution of the photon leads to initial state jets, so that the higher cross section is a direct conse-
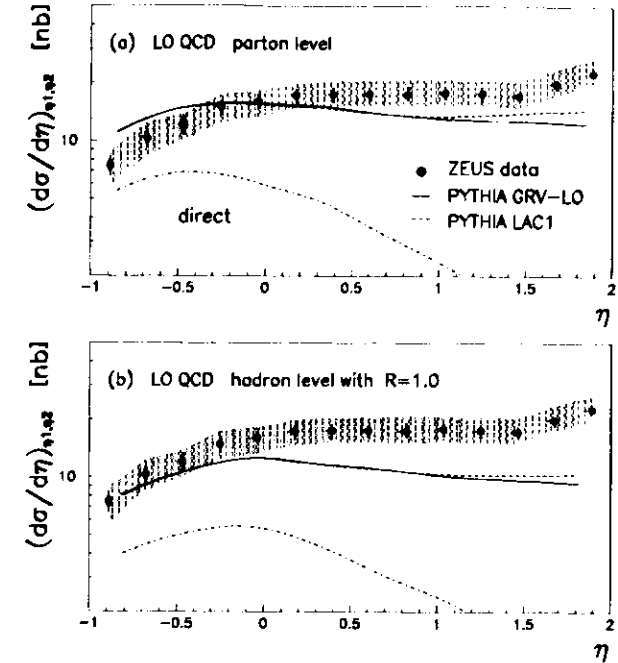
Figure 7.5:

Dijet cross section $(d\sigma/d\eta)_{\eta_1,\eta_2}$ with two entries per event as a function of the rapidity η for $E_{t,jet} > 6$ GeV in the kinematic region defined by $Q^2 < 4$ GeV and $0.2 < y < 0.8$. Error bars indicate statistical errors of data and systematic errors not associated with energy scale and forward energy excess, added in quadrature. The shaded band shows systematic uncertainties due to the energy scale and forward energy excess. In Fig. (a) the data are compared with the LO-QCD prediction given by the two outgoing partons of PYTHIA with a cut on $p_{t,min} = 6$ GeV and without use of parton shower evolution, fragmentation and intrinsic k_t smearing of the partons in the resolved photon and in the proton. Shown are the GRV-LO (full line) and LAC1 (dashed line) photon parameterizations, including the direct component, which is also shown separately (dot-dashed line). Fig. (b) displays the LO-QCD prediction using the two outgoing hadron jets obtained by inclusion of the string fragmentation.
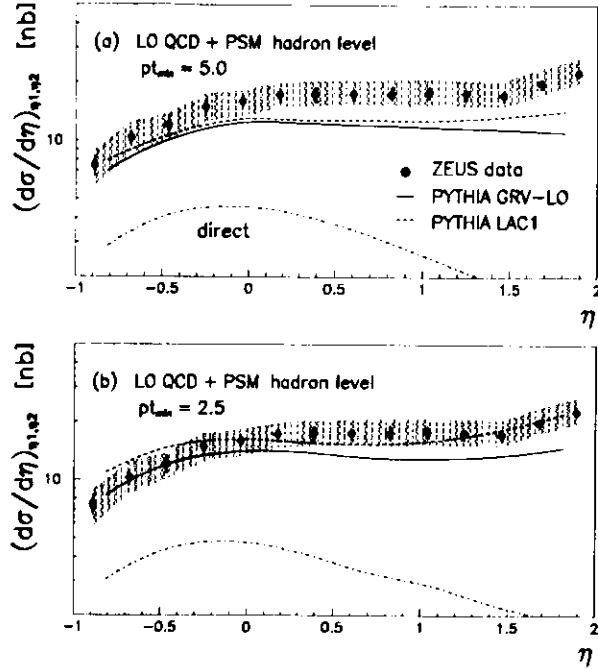
Figure 7.6:

Dijet cross section $(d\sigma/d\eta)_{\eta_1,\eta_2}$ with two entries per event as a function of the rapidity η for $E_{t,jet} > 6$ GeV in the kinematic region defined by $Q^2 \leq 4$ GeV and $0.2 < y < 0.8$. Error bars indicate statistical errors of data and systematic errors not associated with energy scale and forward energy excess, added in quadrature. The shaded band shows systematic uncertainties due to the energy scale and forward energy excess. In Fig. (a) the data are compared with the hadron jet cross section using parton shower evolution, fragmentation and intrinsic k_t smearing of the partons in the resolved photon and in the proton. Shown are the GRV-LO (full line) and LAC1 (dashed line) photon parameterizations, including the direct component, which is also shown separately (dot-dashed line). The Monte Carlo sample is generated with the cut-off parameter $p_{t,min} = 5.0$ GeV. Fig. (b) displays the same predictions using a cut $p_{t,min} = 2.5$ GeV.

quence of parton shower radiation from the gluons of the photon. Thus parton shower evolution lead to an enhancement of the differences between both structure functions.

This is shown clearly in the next Fig. 7.6 (b), where a $p_{t,min} = 2.5$ GeV is used and the ratio on the initial state induced jets is increased compared with the sample of $p_{t,min} = 5.0$ GeV. As a consequence, the difference between GRV-LO and LAC1 is more obvious, and a change of the shape can be observed. While the GRV-LO is more obvious, and a change of the shape can be observed. While the GRV-LO prediction with $p_{t,min} = 5.0$ is approximately flat in the forward region and starts to decrease slightly for $\eta_{jet} > 1.5$, one can observe an increase for GRV-LO in the sample using $p_{t,min} = 2.5$ GeV.

7.5　Summary

The hadron jet cross sections $(d\sigma/d\eta)_{\eta_1,\eta_2}$ integrated over $E_{t,jet} > 6$ GeV is measured as a function of the rapidity η in bins of $\Delta\eta = 0.21$ and is compared with the LO-QCD parton cross section as given by PYTHIA without use of fragmentation, a LO-QCD hadron jet cross section including jet fragmentation, and hadron jet cross sections using fragmentation, intrinsic k_t smearing and parton shower evolution for values of $p_{t,min} = 5.0$ GeV and $p_{t,min} = 2.5$ GeV. While the parton cross section is too large in the backward region, the LO-QCD hadron cross section without use of the parton shower model shows a large deviation in the whole forward region. A better agreement is obtained by inclusion of the parton shower model, where the lower value of $p_{t,min} = 2.5$ GeV leads to an improved description of the data compared with the $p_{t,min} = 5.0$ GeV sample.

In the next chapter, it will be shown that a measurement of the energy flow and the forward energy as a function of x_γ, x_p and y indicates the existence of multiple interactions in γp collision at HERA. Thus, it cannot be expected that predictions of standard PYTHIA cross sections lead to a satisfactory description of the data. Due to the small differences between the GRV-LO and LAC1 photon parametrizations, they cannot be distinguished by these measurements because of these mentioned uncertainties. Therefore the understanding of multiple interactions is essential for the determination of the gluon contents of the photon using dijet measurements.

Chapter 8

Multiple Interactions

The analysis of the energy excess in the forward direction has shown that the discrepancy between data and PYTHIA MC calculation is related to the resolved photoproduction process. One process, which has to be considered only in the resolved process, is the mechanism of multiple interactions (MI), also named multiple scattering (MS), which is the notation used in this chapter. At the end of the '93 Monte Carlo generation using PYTHIA 5.6 a new version PYTHIA 5.7, including multiple interactions, became available and investigations concerning the energy flow problem in the forward direction could be carried out, see [70].

In this chapter, expectations from the so-called *simple model*, see chapter 3, as implemented in PYTHIA 5.7 using the GRV photon structure function are compared with standard PYTHIA 5.6 and data distributions. Distributions of the FCAL energy and a measurement of the energy flow as a function of the polar angle of the entire calorimeter are used to check the final event shape of multiple interactions events.

It is expected that the probability of multiple interactions depends on the x_γ of the hardest scatter, because low values of the hardest scatter leave a high fraction of the photon energy for subsequent interactions. Supposing that most of the reconstructed dijet pairs are produced by the same scatter, which is indicated by the general agreement of data and standard PYTHIA in the $\Delta\phi$ distributions, see Fig. 6.3, the Bjorken-x_γ of the hardest scatter can be estimated from the reconstructed x_γ^{det}. This assumption means that only a negligible contribution of two-jet events is generated by two different scatters with uncorrelated jets in $\Delta\phi$. The back-to-back behaviour of the jets will be analysed because of its sensitivity to additional jet production mechanisms as well as to the extra energy in the forward direction.

8.1   Measurement of the Energy Flow

The starting point for the discussion of multiple scattering effects in hard photoproduction was the discrepancy of the FCAL energy distribution between the dijet sample defined in chapter 5 and the Monte Carlo simulation. Fig. 8.1 shows histograms of

123

FCAL energy for the dijet sample (full circles), standard PYTHIA (broken line) and the expectation of the MS sample. It is seen, that the inclusion of the MS simulation leads to an improvement in describing the data.

In order to localize the energy excess more precisely, the energy flow as a function of the polar angle Θ has been measured in the range $5° < \Theta < 175°$. Fig. 8.2 depicts the mean energy per event for the resolved dijet sample, separated by a cut on $x_\gamma^{det} < 0.75$ to suppress direct contribution. The cut is used to emphasize the resolved MS contribution and to reduce the sensitivity to the resolved/direct mixing. Data (full circles) are compared with standard PYTHIA with the GRV (doted line) and LAC1 (dashed doted line) photon parametrization, respectively, and the PYTHIA MS prediction (full line). Fig. 8.2.(a) presents the full range of Θ in a logarithmic scale. The standard PYTHIA samples with GRV parametrization gives a good description of data in the whole region, except in the first two bins. Fig. 8.2.(b) shows the forward direction in a linear scale. The prediction based on LAC1 is not able to describe the excess of energy in the forward direction, in spite of its high gluon contribution at low x_γ, which is able to cause larger energy depositions in FCAL region. The backward region, Fig. 8.2.(c) is approximately described by the GRV-LO, LAC1 and MS sample, except in the last bin, where the MS energy flow agrees very well with data, while the LAC1 prediction is too high and the GRV value is slightly above the data.

In contrast to a reasonable description of the energy flow in the forward and backward direction, the MS model disagrees with the data and standard PYTHIA in the range $80° < \Theta < 130°$, where the energy flow is overestimated. Take note, that the
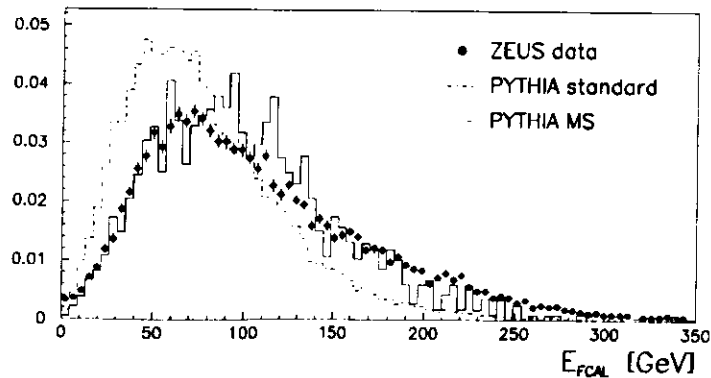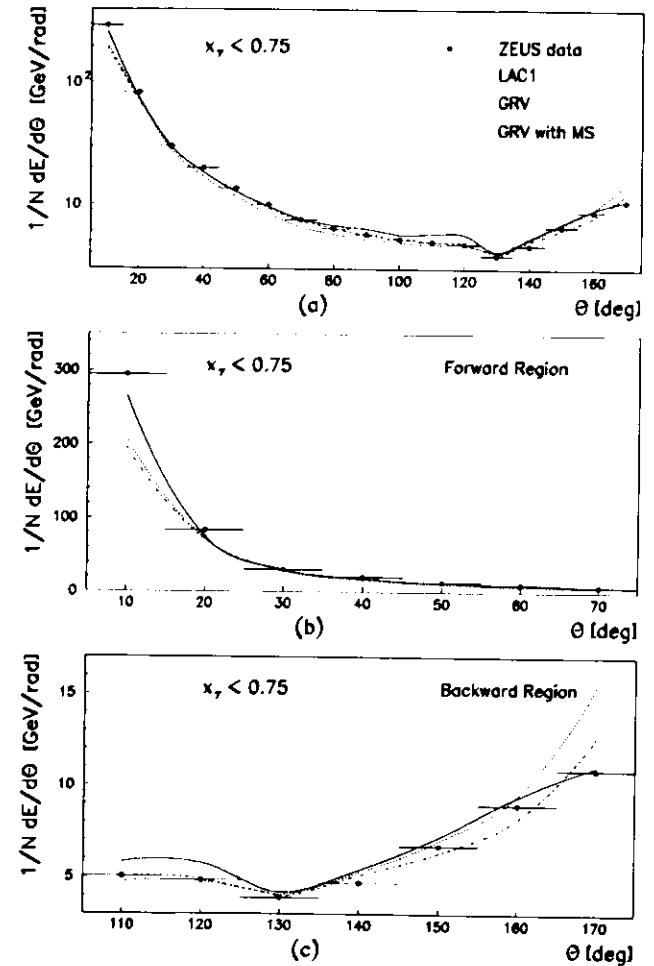

Figure 8.1: The FCAL energy distribution

Figure 8.2: Energy flow as a function of Θ for resolved photoproduction Fig. (a) shows the energy per event as a function of the polar angle Θ. Fig. (b) and (c) show the forward and backward regions on a linear scale. A cut on $x_\gamma^{det} < 0.75$ is applied to reduce the direct component.

mutiple scattering events are generated using the GRV-LO photon parametrization. One can expect, that MS with the LAC1 structure function will lead to a decrease of the energy flow in the BCAL region, as observed for the standard PYTHIA predictions with GRV-LO and LAC1.
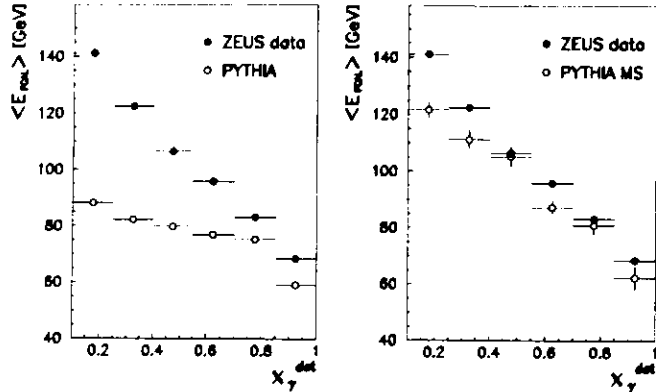

Figure 8.3: Mean of FCAL energy versus x_γ^{det}
a) The left plot shows a comparison of the mean FCAL energy as a function of x_γ^{det} for data (full circles) and standard PYTHIA (open circles). b) The right plot shows a comparison between data and the multiple scattering model.

8.1.1 Forward energy dependence on x_γ, x_p and y_{JB}

In order to study the energy flow dependence on the kinematics, the mean of the FCAL energy is measured as a function of x_γ^{det}, $\log(x_p^{det})$ and y_{JB}. Fig. 8.3 shows two plots of the FCAL energy versus x_γ^{det}, where the error bars denote the standard variation of the FCAL distribution in the given bin. Fig. 8.3(a) compares data with PYTHIA, where a clear disagreement is present. Fig. 8.3(b) demonstrates the improvement by use of the MS model.

Fig. 8.4 presents $<E_{FCAL}>$ as a function of x_p^{det}. The increase of $<E_{FCAL}>$ towards higher x_p^{det} values in the data is predicted by standard PYTHIA and the MS sample. However, standard PYTHIA and data differ in shape and in absolute magnitude, whereas the MS PYTHIA prediction leads to a much better description of the data.

Fig. 8.5 shows the mean FCAL energy as a function of y_{JB}, for the resolved subsamples, selected by a cut on $x_\gamma^{det} < 0.75$. In contrast to standard PYTHIA, where approximately no dependence on y_{JB} can be observed, there is an increase

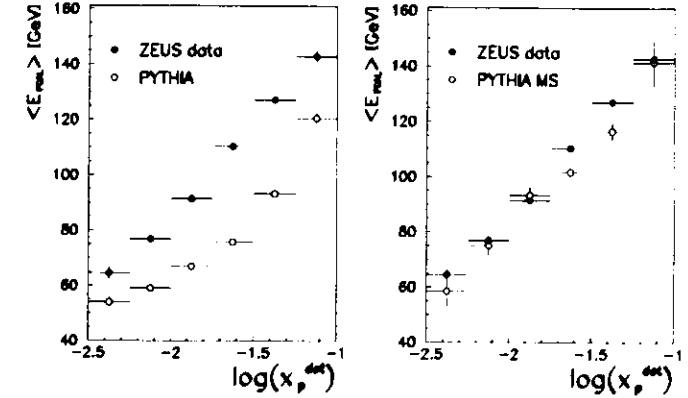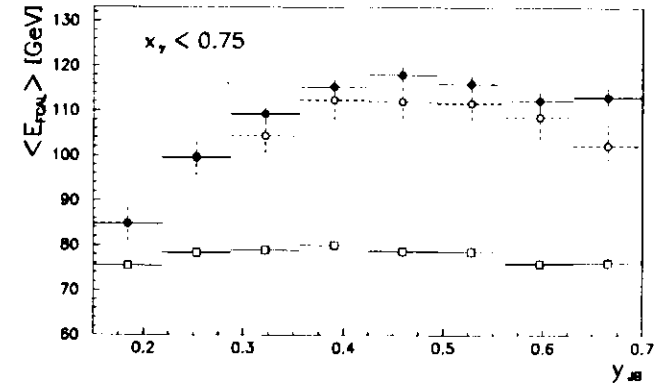**Figure 8.4: Mean of FCAL energy versus $\log(x_p^{det})$**

Figure 8.5: Mean of FCAL energy versus y_{JB}
Shown are data (full circles), standard PYTHIA MC (open squares) and the multiple scattering model (open circles).

from low-y_{JB} to higher values in the data with a maximum at $y_{JB} = 0.45$. The MS events show a similar behaviour, but are still below the data. This plot indicates, that the forward energy flow of the MS model is a function of the photon energy, which is given by $E_\gamma = y \cdot E_e$, while the FCAL energy of standard PYTHIA is basically independent on the photon energy.

These comparisons have shown, that typical characteristics of the multiple scattering model can be observed in the data. The simple model of PYTHIA 5.7 is able to describe shape and approximately the absolute values of the mean FCAL energy as a function of the kinematic variables x_γ^{det}, x_p^{det} and y_{JB}.

8.2   Measurement of the back-to-back behaviour

In this section, the correlation of the two jets, expressed by their difference in azimuth angles $\Delta\phi$, is compared. In Fig. 8.6 the $\Delta\phi$ distribution is given in a linear scale and in a logarithmic scale. The first plot shows, that the general shape of data (full circles) is described by standard PYTHIA, denoted as 'GRV', and multiple scattering, which is denoted as 'GRV with MS'. The logarithmic plot, however, displays differences in the low $\Delta\phi$ tail, also shown in Fig. 6.3. The tail of the data distribution is well approximated by the MS sample. The increase of events with small values of $\Delta\phi$ indicates the presence of uncorrelated jets from different scatters in one γp-collision.
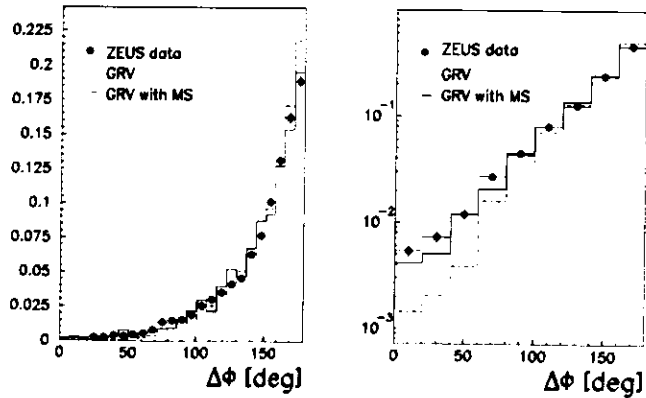

Figure 8.6: Difference of azimuth angles $\Delta\phi$ between the two jets
The figure shows the $\Delta\phi$ distributions for data (full circles), standard PYTHIA (broken line) and PYTHIA MS events in a linear and logarithmic scale.

8.2.1   Mean of $\Delta\phi$ as a function of x_γ^{det}

In order to check the influence of x_γ on the jet correlation, the mean of $\Delta\phi$ is measured as a function of x_γ^{det}. Fig. 8.7 presents two plots, where data are compared with normal PYTHIA and MS PYTHIA samples. Again, the comparison shows that the multiple scattering model is in reasonable agreement with the data distribution, while the standard PYTHIA expectation is not able to describe the decrease of the mean to small values. As in the measurement of the mean FCAL energy, a disagreement between data and PYTHIA without multiple interactions becomes more obvious for low values of x_γ^{det}, which means that at low values, an increasing fraction of two-jet pairs is affected by the additional activity of the multiple interactions. It seems reasonable, that the reconstructed x_γ^{det} is not a good estimation of the hardest scatter for low-$\Delta\phi$ events. However, since no dijet pair with higher x_γ^{det} is found it can be expected, that x_γ^{det} indicates approximately an upper limit of the hardest scatter.

It is interesting, that the $<\Delta\phi>$ distribution of standard PYTHIA decrease also towards low x_γ^{det}-values, which means that the basic mechanism of this behaviour is not related to multiple interactions. This mechanism is most probably the influence of the photon remnant, which carries higher energies in low-x_γ events, so that the two jets are not balanced by each other. In the case of multiple scattering, a further deterioration of the back-to-back behaviour is caused by the production of additional jets from subsequent scatters resulting in uncorrelated pairs of jets.
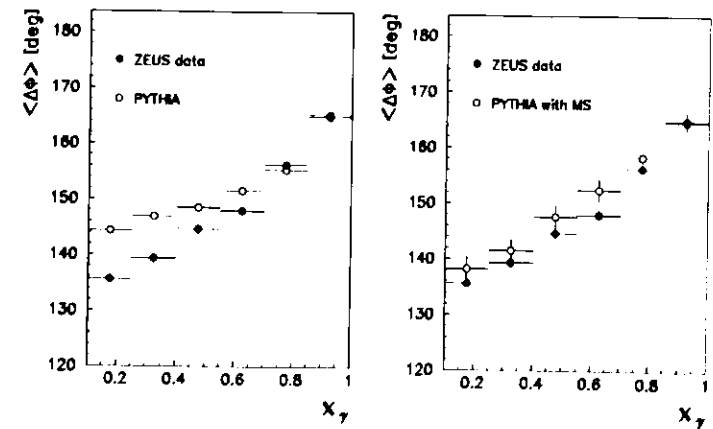

Figure 8.7: Mean value of $\Delta\phi$ as a function of x_γ^{det}

8.3 Summary

The differences between data and standard PYTHIA MC in the forward energy flow and the back-to-back correlation of the two jets can be generally explained by a model of multiple scattering as implemented in PYTHIA 5.7. Detailed comparisons of the mean FCAL energy as a function of x_γ^{det}, $\log(x_p)$ and y_{JB} show that a large improvement is achieved by application of the mutiple scattering model in resolved photoproduction. There are still discrepancies, but in general the MS model yields a reasonable description of all distributions.

Chapter 9

Summary and Conclusions

Summary

The main goal of the present work was the analysis of the partonic structure of almost real photons in dijet photoproduction. At the ep collider HERA, photoproduction of high transverse momentum jets ($p_t \approx 5$–20 GeV), so-called hard photoproduction, offers the opportunity to study the quasi-real photon in a kinematic range, where its structure can be evaluated within perturbative QCD. In leading-order QCD, two classes of processes contribute to jet photoproduction, the *direct* and the *resolved* processes. The signature of the direct and the resolved processes is the production of two hard jets, which balance each other with almost identical transverse momenta. In addition to the outgoing jet-pair, there is a low-p_t photon remnant close to the direction of the incoming electron (backward direction) in resolved processes.

Since the distribution of the pseudorapidity η of the jets is strongly related to the parton densities, one can use the η dependence of jet cross sections to get information about the partonic structure of the resolved photon. In particular, jet photoproduction allows the analysis of the gluon contents of the photon, which is not constrained by existing data from deep inelastic electron-photon scattering experiments at $e^- e^+$ colliders. In this thesis the differential dijet cross section $(d\sigma/d\eta)_{\eta_1,\eta_2}$ with two jet entries per event is measured and compared with predictions of the PYTHIA 5.6 Monte Carlo program.

From the data collected during 1993 by the ZEUS detector with an integrated luminosity of 545 nb^{-1}, a clean dijet sample of hard photoproduction events has been selected with γp center of mass energies between 130 and 265 GeV, and at least two reconstructed jets in the pseudorapidity region $-1 < \eta < 2$, where the two jets with the highest transverse energy are taken for the analysis and the measurement of the differential dijet cross section $(d\sigma/d\eta)_{\eta_1,\eta_2}$.

It is shown, that general event characteristics and the energy flow of the data are described by PYTHIA, except in the forward region close to the beam pipe, where a large excess of energy is observed, not described by the standard PYTHIA program.

Clear evidence for resolved and direct photoproduction is seen in distributions of the fractional momentum x_γ of partons with respect to the photon and the backward energy, defined by the measured energy in a cone of $45°$ around the beam pipe. A peak at $x_\gamma = 0.85$ is a clear signature of the direct process, while the backward energy flow can be described only by the occurrence of a photon remnant close to the beam pipe, where the direct contribution is small. Jet variables such as track multiplicity inside the jets, the jet energy, the transverse jet energy and the jet multiplicity itself compare well with the PYTHIA predictions.

Measurement of the differential dijet cross section $(d\sigma/d\eta)_{\eta_1,\eta_2}$

The differential dijet cross section $(d\sigma/d\eta)_{\eta_1,\eta_2}$ has been measured in the kinematic region defined by $Q^2 < 4\,\mathrm{GeV}^2$ with a median of approximately $10^{-3}\,\mathrm{GeV}^2$ and $0.2 < y < 0.8$ for dijet events with transverse jet momenta $E_t > 6\,\mathrm{GeV}$ in the range $-1 < \eta < 2$ and refers to jets at the hadron level defined by a cone algorithm in (η, ϕ) space with a cone radius of one. Detector effects have been corrected by comparison with a Monte Carlo sample generated by PYTHIA with a full simulation of the detector response. The measurement probes the proton and the resolved photon in a kinematic region down to fractional momenta of $x_p = 0.003$ and $x_\gamma = 0.1$ respectively at scales of the hard γp interaction up to $\hat{Q}^2 = p_t^2 \approx 300\,\mathrm{GeV}^2$, where p_t is the transverse momentum of the two partons generated in the hard scattering process.

The measured differential cross section is compared with the LO-QCD parton cross section as given by PYTHIA without use of fragmentation, a LO-QCD hadron jet cross section including jet fragmentation, and hadron jet cross sections using fragmentation, intrinsic k_t smearing and parton shower evolution for values of $p_{t,\mathrm{min}} = 5.0\,\mathrm{GeV}$ and $p_{t,\mathrm{min}} = 2.5\,\mathrm{GeV}$. The comparison includes predictions from the GRV-LO and LAC1 photon parameterizations, which differ mainly in the gluon contents at low-x_γ values, while the proton parton distributions is given by the MRSD- parameterization. The main results from the dijet cross section measurement are as follows:

- The pure LO QCD parton cross section ($p_{t,\mathrm{min}} = 6.0\,\mathrm{GeV}$) is too large in the low η region, while the forward region is underestimated for both, the GRV-LO and the LAC1 photon parameterizations.

- Including fragmentation, the LO QCD hadron jet cross section is described well in the backward region within the systematic errors. In the forward region ($\eta > 0$) there is however a discrepancy, the MC predictions being too low.

- The hadron jet cross sections using fragmentation, intrinsic k_t smearing and initial and final state parton shower evolution with values of $p_{t,\mathrm{min}} = 5.0\,\mathrm{GeV}$ and $p_{t,\mathrm{min}} = 2.5\,\mathrm{GeV}$ show that the lower value of $p_{t,\mathrm{min}}$ leads to the best agreement with the data. In the backward direction $\eta < 0$ the GRV-LO predictions agree with the data, while LAC1 leads to values above the data. In the forward region $\eta > 0$ LAC1 describes the data and the GRV-LO expectation is below

the data. However, the observation of an excess of the forward energy flow compared to the Monte Carlo simulation indicates that a better understanding of the forward region is required. An improvement of the MC description including a correct energy flow description in the forward direction may then lead to a better understanding and a decrease of the systematic errors, so that the difference between the GRV-LO and LAC1 predicted dijet cross section may then become more significant.

Multiple Interactions

Using different methods for the separation of the resolved and the direct contributions, it is shown that the excess of the forward energy flow is related to the resolved process and is not observed in the direct case. The absence of additional energy in the direct process demonstrates, that the detector simulation is not responsible for the observed effect. Therefore, the forward energy excess must be explained by a modification of the resolved process, not included in the standard PYTHIA 5.6 program. One approach for an explanation of the observed energy excess is the *multiple interactions* mechanism in resolved photoproduction, which allows several hard interactions in a given photon-proton collision. Expectations from the so-called *simple model* as implemented in PYTHIA 5.7 are compared with standard PYTHIA 5.6 and data distributions.

A measurement of the energy flow and the forward energy distribution as well as correlation plots of the mean FCAL energy as a function of x_γ, $\log(x_p)$ and y show that the multiple interactions model gives a much improved description of the data. The same is true for the distributions of $\Delta\phi$, the difference in azimuth angles of the two jets. There are, however still discrepancies, especially in the low-x_γ region below $x_\gamma = 0.4$, but in general the simple model of multiple interactions leads to a reasonable description of all distributions.

Conclusions and Outlook

The present work has shown that dijet photoproduction can be used to study the partonic structure of the photon. General event characteristics and jet variables are in agreement with Monte Carlo predictions using the PYTHIA 5.6 program, except in the forward region. Multiple interactions, as implemented by the simple model in PYTHIA 5.7, give a far better description of the hadronic energy flow. A precise comparison of different photon parameterizations requires further studies of the forward energy excess, where an interesting model for future studies is given by the multiple interactions approach. It should also be noted, that so far the available models are calculated in leading order only.

Bibliography

[1] St. Bentvelsen, J. Engelen, P. Kooijman
Reconstruction of (x, Q^2) and Extraction of Structure Functions in Neutral Current Scattering at HERA
Proceedings of the Workshop Physics at HERA, Vol. 1, 23–41
Hamburg, (1991), edited by W. Buchmüller, G. Ingelman

[2] F. Halzen, A. Martin
Quarks and Leptons: An Introductory Course in Modern Particle Physics
John Wiley & Sons, (1984) 195.

[3] H. Baer, J. Ohnemus, J. F. Owens
Expectations for Two- and Three-Jet Events at HERA
Z. Phys. C42 (1989) 657.

[4] A. Ali et al.
Heavy Quark Physics at HERA: Introduction and Overview
Proceedings of the HERA Workshop, Vol. 1, 395
Hamburg, (1987), edited by R. D. Peccei

[5] CTEQ Collaboration
Handbook of Perturbative QCD
edited by G. Steerman, (1993) 70.

[6] G. Altarelli, G. Parisi
Asymptotic Freedom in Parton Language
Nucl. Phys. B126 (1977) 289.

[7] P. D. B. Collins, A. D. Martin
Hadron Interactions
Graduate Student Series in Physics, Adam Hilger LTD, Bristol (1984) 63.

[8] G. A. Schuler, T. Sjöstrand
Towards a Complete Description of High-Energy Photoproduction
CERN-TH.6796/93 (1993)

[9] T. F. Walsh, P. Zerwas
Two-Photon Processes in the Parton Model
Phys. Lett. 44B (1973) 195.

[10] E. Witten
Anomalous Cross Section for Photon-Photon Scattering in Gauge Theories
Nucl. Phys. B120 (1977) 189.

[11] W. A. Bardeen, A. J. Buras
Higher-Order Asymptotic-Freedom Corrections to Photon–Photon Scattering
Phys. Rev. D20 (1979) 166.

[12] H. Abramowicz, et al.
Some Topics in ep Scattering: II. Parton Distributions in the Photon
DESY-Report 91–057, (1991), 8.

[13] J. J. Sakurai
Theory of Strong Interactions
Ann. Phys. (N.Y.) 11 (1960) 1.

[14] H. Kolanoski
Two-Photon Physics at $e^+ e^-$ Storage Rings
Springer-Verlag Berlin, Heidelberg, New York, Tokyo (1984), 150.

[15] G. Rossi
Singularities in the Perturbative QCD Treatment of the Photon Structure Functions
Phys. Lett. 130B (1983) 105.

[16] D. W. Duke, J. F. Owens
Quantum-Chromodynamic Corrections to Deep-Inelastic Compton Scattering
Phys. Rev. D26 (1982) 1600.

[17] W. R. Frazer
Proceedings of the Vth International Conference on Two-Photon Physics, Aachen, (1983), edited by Ch. Berger (Springer, New York, 1984), 377.

[18] M. Glück, K. Grassie, E. Reya
Detailed QCD Analysis of the Photon Structure Function
Phys. Rev. D30 (1984) 1447.

[19] P. Castorina, A. Donnachie
The Structure Function of the Pion
Z. Phys. C45 (1990) 497.

[20] M. Drees, K. Grassie
Parametrizations of the Photon Structure and Applications to Supersymetric Particle Production at HERA
Z.Phys. C28 (1985) 451.

[21] H. Abramowicz, K. Charchula, A. Levy
Parametrization of Parton Distributions in the Photon
Phys. Lett. B269 (1991) 458.

[22] M. Glück, E. Reya, A. Vogt
Photonic Parton Distributions
Phys. Rev. D46 (1992) 1973.

[23] M. Glück, E. Reya, A. Vogt
Parton Distributions for High Energy Collisions
Z.Phys. C53 (1992) 127.

[24] M. Glück, E. Reya, A. Vogt
Pionic Parton Distributions
Z.Phys. C53 (1992) 651.

[25] TOPAZ Collaboration, H. Hayashii et al.,
Measurement of the Inclusive Jet Cross Section in $\gamma\gamma$ Interactions at TRISTAN
Phys. Lett. B314 (1993) 149.

[26] AMY Collaboration, B.J. Kim et al.,
Measurement of the Inclusive Jet Cross Section in $\gamma\gamma$ Interactions at TRISTAN
Phys. Lett. B325 (1994) 248.

[27] L.E. Gordon, J.K. Storrow
The Parton Distribution Functions of the Photon and the Structure Function $F_2^\gamma(x,Q^2)$
Z.Phys. C56 (1992) 307.

[28] G.D'Agostini, D. Monaldi
Identification of High p_t Jet Events Produced by a Resolved Photon at HERA and Reconstruction of the Initial State Parton Kinematics
Proceedings of the Workshop Physics at HERA, Vol. 1, 527
Hamburg, (1991), edited by W. Buchmüller, G. Ingelman

[29] A. Valkarova
Separation of Resolved Photon Process and the determination of x_1, x_2 Parton Momentum Fractions
Proceedings of the Workshop Physics at HERA, Vol. 1, 535 Hamburg, (1991), edited by W. Buchmüller, G. Ingelman

[30] B.L. Combridge, C.J. Maxwell
Untangling Large-p_t Hadronic Reactions
Nucl. Phys. B239 (1984) 429.

[31] R.S. Fletcher, F. Halzen, S. Keller, W.H. Smith
Deciphering the Quark-Gluon Structure of High Energy Photons Using a Tagged Photon Beam at HERA
Phys. Lett. B266 (1991) 183.

[32] M. Drees, R.M. Godbole
Measuring the Parton Content of the Photon at DESY ep collider HERA
Phys. Rev. D39 (1989) 169.

[33] G. Bodwin, J. Repond
Direct versus Resolved Photoproduction of Jets
ZEUS-Note 94-006, Feb. 1994

[34] M. Klasen, G. Kramer, S.G. Salesch
Photoproduction of Jets at HERA: Comparison of Next-to-Leading Order Calculation with ZEUS Data
DESY-Report 94-232, Dec. 1994

[35] J. Owens
Talk given at the Tagung der Deutschen Physikalischen Gesellschaft
Dortmund, 1993.

[36] J. Owens
Lectures given at the CTEQ Summer School
August 1994, Lake Ozark, Missouri

[37] T. Sjöstrand, M. van Zijl
A Multiple-Interaction Model for the Event Structure in Hadron Collisions
Phys. Rev. D36 (1987) 2019-2041.

[38] M. Drees, F. Halzen
Hadron Structure of High-Energy Photons
Phys. Rev. Lett. 61 (1988) 275.

[39] ZEUS Collab., M. Derrick et al.
A Measurement of $\sigma_{tot}(\gamma p)$ at $\sqrt{s} = 210$ GeV
Phys. Lett. B293 (1992) 465-477.

[40] J.R. Forshaw, J.K. Storrow
Minijets and the Total Inelastic Photoproduction Cross Section
Phys. Lett. B268 (1991) 116.

[41] T. Sjöstrand
PYTHIA 5.6 and JETSET 7.3
Physics and Manual
CERN-TH.6488/92, (1992)

[42] J. Straver
Design, Construction and Beam Tests of the High Resolution Uranium Scintillator Calorimeter for ZEUS
Doctoral Thesis (1991).

[43] U. Holm et al.
The ZEUS Detector
Status Report 1993

[44] H. Bethe, W. Heitler
Proc. Roy. Soc. A146 (1934) 83.

[45] U. Amaldi
Fluctuations in Calorimetry Measurements
Physica Scripta 23, (1981) 409-424

[46] E. Lohrmann
Private communication

[47] E. Lohrmann
Einführung in die Elementarteichenphysik
Teubner, Stuttgart (1983)

[48] C. W. Fabjan
Calorimetry in High-Energy Physics
CERN-EP/85-54

[49] J. Krüger
The Uranium Scintillator Calorimeter for the ZEUS Detector at the Electron-Proton Collider HERA
DESY-Report, DESY F35-92-02, (1992)

[50] G. Marchesini,   B.R. Webber,   G. Abbiendi,   I.G. Knowles,   M.H. Seymour,
L. Stanco
HERWIG a Monte Carlo Event Generator for Simulating Hadron Emission Reactions with Interfering Gluons
Computer Phys. Commun. 67 (1992) 465.

[51] B. Anderson, G. Gustafson, G. Ingelmann, T. Sjöstrand
Parton Fragmentation and String Dynamics
Phys. Rep. 97 (1983) 31.

[52] T. Sjöstrand
A Model for Initial State Parton Showers
Phys. Lett. B157 (1985) 321.

[53] T. Sjöstrand
PYTHIA 5.6 and JETSET 7.3
Physics and Manual
CERN-TH.7122/93, (1993) 192.

[54] M. Bengtsson, T. Sjöstrand
Coherent Parton Showers versus Matrix Elements -
Implications of PETRA/PEP Data
Phys. Lett. B185 (1987) 435.

[55] G. Marchesini, B.R. Webber
Monte Carlo Simulation of General Hard Processes with Coherent QCD Radiation
Nucl. Phys. B310 (1988) 461.

[56] F. Bruyant et al.
GEANT User's Guide
CERN Program Library Office, Jan (1993)

[57] L. Hervás
The Pipelined Readout for the ZEUS Calorimeter
DESY F35D-91-01
FTUAM-EP-91-01, Jan. (1991).

[58] K. Tokushuku
Description of Standard Trigger
Vaxnews 200, Folder ZEUS.GENERAL
*GFLT Trigger Slot Assignment for Standard2 *May93* Runs*
Vaxnews 208, Folder ZEUS.GENERAL
GFLT Subtrigger Dictionary
Vaxnews 358, Folder ZEUS.GENERAL

[59] L.W. Mo, T.A. Nunamaker
The Subject Matter Related to PMT, Magnetic Shield, Installation and High Voltage Base on BCAL
ZEUS-NOTE 91-131, (1991).

[60] E. Tscheslog
ZEUS Reconstruction Program Organisation and Control
ZEUS-Note 91-037 (1991)

P. de Jong
Status of the Uranium Calorimeter Reconstruction Software
ZEUS-NOTE 92-019, (1992)

[61] D. Bandyopadhyay et al.
VCTRAK: Offline Output Information
ZEUS-Note 93-122 (1993)

[62] J. E Huth et al.
FERMILAB-Conf-90/249-E (1990)

[63] ZEUS Collab., M. Derrick et al.
Observation of Jet Production in Deep Inelastic Scattering with a Large Rapidity Gap at HERA
Phys. Lett. B332 (1994) 228-243.

[64] ZEUS Collab., M. Derrick et al.
Observation of Hard Scattering in Photoproduction Events with a Large Rapidity Gap at HERA
Phys. Lett. B346 (1995) 399-414.

[65] G. Ingelman, P. E. Schlein
Jet Structure in High Mass Diffractive Scattering
Phys. Lett. B152 (1985) 256.

[66] ZEUS Collab., M. Derrick et al.
Diffractive Hard Photoproduction at HERA and Evidence for the Gluon Content of the Pomeron
DESY-Report 95-115 (1995)

[67] C. Glasman, J. Terron
Jet Profiles in Photoproduction and Deep Inelastic Scattering at HERA
ZEUS-Note 94-125, Oct. (1994)

[68] M. Drees
Initial State Showering in Resolved Photon Interactions
Talk held at the 23rd International Symposium on Multiparticle Dynamics, Aspen, Colo., Sep. 1993
MAD/PH/797, Oct. (1993)

[69] K. Desch, C. Glasman, J. Terron
Inclusive Jet Differential Cross Sections in Very Low Q^2 Electroproduction at HERA
ZEUS-Note 94-086, (1994)

[70] C. Coldewey, M. Iori
Evidence for Multiple Interactions in Dijet Events at low Q^2 in the ZEUS 93 Data
ZEUS-Note 95-034, (1995)